Coherent Dynamics of Quantum Dots in Photonic-Crystal Cavities

Madsen, Kristian Høeg

Publication date:
2013

Document Version
Publisher's PDF, also known as Version of record

Coherent Dynamics of Quantum Dots in Photonic-Crystal Cavities

A dissertation
submitted to the Department of Photonics Engineering
at the Technical University of Denmark
in partial fulfillment of the requirements
for the degree of
philosophiae doctor

Kristian Høeg Madsen
June 14, 2013

Coherent Dynamics of Quantum Dots in Photonic-Crystal Cavities

Preface

The research presented in this thesis was carried out from March 2010 to June 2013 in the Quantum Photonics Group at DTU Fotonik at the Technical University of Denmark and later at the Niels Bohr Institute at the University of Copenhagen under the supervision of professor Peter Lodahl and professor Jesper Mørk.

First of all I would like to thank my main supervisor Peter Lodahl, with whom it has been a pleasure to work. Peter has been involved in every aspect of the work presented here, and his valuable supervision and encouraging input has helped form this thesis. When I started my studies in the Quantum Photonics Group at DTU Fotonik I was first introduced to the optical laboratories under the competent supervision of Serkan Ates, whom I would like to thank for teaching me the ins and outs of quantum optics experiments and also for a very pleasant working environment. I would also like to express my gratitude towards Luca Sapienza and Henri Thyrrestrup Nielsen for taking the time to teach me about the experimental setup.

Solid-state quantum optics is a multi-disciplinary field that incorporates elements of many different areas of physics, and the research presented here would not have been possible without collaboration. I am indebted to Serkan Ates, Asger Kreiner-Møller, Anders Nysteen, Toke Lund-Hansen, Jin Liu, and Alisa Javadi for their valuable contributions to the work presented here. In particular I would like to thank Per Kaer for an excellent collaboration and for discussing all the aspects of phonon dephasing with me. None of the work presented here would have been possible without samples, and I would like to thank Søren Stobbe for the photonic-crystal samples as well as Stephan Reitzenstein now at Technische Universität Berlin for supplying the micropillar sample.

During my Ph.D. studies I have had the rewarding experience of co-supervising three master-project students; Asger Kreiner-Møller, Tau Lehmann, and Sven Albrecht. I would like to thank them all for their enthusiasm and hard work.

In September 2011, the Quantum Photonics Group moved from DTU Fotonik to the Niels Bohr Institute. I moved with the group, but I stayed enrolled at DTU Fotonik, and I want to thank Jesper Mørk for allowing me to work at the Niels Bohr Institute, while being part of his research group. Upon arrival at the Niels Bohr Institute an empty room awaited, and it has been a tremendous challenge but also a very giving experience to build up a complete optical setup. I want to thank the whole Quantum Photonics Group for sharing this task and in particular Immo Söllner, Henri Thyrrestrup Nielsen, David Garcia, Alisa Javadi, and Marta Arcari for sharing the many practical tasks in setting up the laboratories.

I want to thank my former colleagues at DTU Fotonik for making it a very pleasant and productive place to work, as well as the Quantop group at the Niels Bohr Institute for the warm welcome, their help, and for the enjoyable working environment. In the Quantum Photonics Group there is a tradition for taking a large interest in others work, which has resulted in many fruitful and heated discussions. Therefore I would like to thank the whole Quantum Photonics Group and in particular Peter Lodahl, Immo Söllner, Jin Liu, Marta Arcari, David Garcia, Alisa Javadi, Søren Stobbe, Tau Lehmann, and Petru Tighineanu. Many of the group members have become good friends and have made the last three years very enjoyable.

In that respect I want to especially thank Immo Söllner, who has become one of my closest friends. He has engaged in numerous discussions with me on almost every aspect of my work, always been very helpful in the laboratory, and most of all made the time off-campus very enjoyable.

Finally, I want to thank my family and my girlfriend for supporting me throughout this project, for having paid such an interest in my research, and for listening to sometimes detailed explanations of quantum optics.

Abstract

In this thesis we have performed quantum-electrodynamics experiments on quantum dots embedded in photonic-crystal cavities. We perform a quantitative comparison of the decay dynamics and emission spectra of quantum dots embedded in a micropillar cavity and a photonic-crystal cavity. The light-matter interaction in the micropillar cavity is so strong that we measure non-Markovian dynamics of the quantum dot, and we compare to the Jaynes-Cummings model with all parameters independently determined. We find an excellent agreement when comparing the dynamics, but the emission spectra show significant deviations. Similar measurements on a quantum dot in a photonic-crystal cavity show a Rabi splitting on resonance, while time-resolved measurements prove that the system is in the weak coupling regime.

While tuning the quantum dot through resonance of the high-Q mode we observe a strong and surprisingly broadband Purcell enhancement of the decay rate, which cannot be described by the Jaynes-Cummings model. The broadband Purcell enhancement occurs because the quantum dot emits or absorbs a longitudinal acoustic phonon with the energy corresponding to the detuning between the quantum dot and cavity. We successfully model the decay rates with a microscopic model that allows us to for the first time extract the effective phonon density of states, which we can model with bulk phonons.

Studies on a quantum dot detuned from a low-Q mode of a photonic-crystal cavity show a high collection efficiency at the first lens of $(44.3\pm2.1)\%$, while the emission exhibits a very strong anti-bunching. We demonstrate how the quantum dot can be efficiently and selectively excited through longitudinal optical and acoustic phonon-mediated excitation. Indistinguishability measurements of the emitted photons under these two excitation schemes reveal low dephasing rates of 0.82 ± 0.41 μeV and 0.42 ± 0.18 μeV respectively.

Resumé

Denne afhandling beskriver kvante-elektrodynamiske eksperimenter på kvantepunkter i fotoniske nanostrukturer. Vi udfører en kvantitativ sammenligning af henfaldsraterne og emissions spektrerne fra kvantepunkter i mikrosøjle og i fotonisk krystal-kaviteter. Lys-stof vekselvirkningen er tilstrækkelig stærk i mikrosøjle kaviteten til, at vi måler et ikke-Markovisk henfald af kvantepunktet, og vi sammenligner vores data med Jaynes-Cummings modellen (JCM), hvor alle parametrene er målt uafhængigt. Sammenligningen af dynamikken viser en glimrende overensstemmelse, mens emissions-spektrene viser store afvigelser. Lignende målinger på et kvantepunkt i en fotonisk krystal-kavitet viser en Rabi opdeling, mens tidsopløste målinger viser, at systemet er svagt koblet.

Vi måler en stærk og forbavsende bredbåndet Purcell-forstærkning af kvantepunktets henfaldsrate, når det bringes gennem kavitetens resonans, hvilket ikke kan forklares med JCM. Den bredbåndede Purcell forstærkning foranlediges af, at kvantepunktet enten udsender eller absorberer en longitudinal akustisk fonon med en energi svarende til energiforskellen mellem kvantepunktet og kaviteten. Ved brug af en mikroskopisk model kan vi modellere henfaldsraterne glimrende, hvilket gør det muligt at udtrække den effektive fonon tilstandstæthed for første gang, og vi kan modellere denne med plane bølger.

Vi undersøger også et kvantepunkt i en fotonisk krystal-kavitet med en lav kvalitets-faktor. De emitterede fotoner opsamles med $(44.3 \pm 2.1)\%$ effektivitet ved den første linse, og vi viser at fotonerne i meget høj grad ikke klumper sig sammen. Vi demonstrerer, at kvantepunktet kan eksiteres effektivt og selektivt ved den ledsagende udsendelse af longitudinale optiske og akustiske fononer. Ved at måle hvor uadskillelige de udsendte fotoner er under disse forskellige typer eksitation, kan vi afsløre, at omgivelserne ødelægger kohærensen med en rate på hhv. 0.82 ± 0.41 μeV og 0.42 ± 0.18 μeV.

List of Publications

The work performed in the course of this Ph.D.-project has resulted in the publications listed below:

Journal Publications

1. K. H. Madsen, S. Ates, T. Lund-Hansen, A. Löffler, S. Reitzenstein, A. Forchel, and P. Lodahl, *Observation of Non-Markovian Dynamics of a Single Quantum Dot in a Micropillar Cavity*, Physical Review Letters, **106**, 233601 (2011).

2. K. H. Madsen and P. Lodahl, *Quantitative analysis of quantum dot dynamics and emission spectra in cavity quantum electrodynamics*, New Journal of Physics, **15**, 025013 (2013).

3. K. H. Madsen, P. Kaer, A. Kreiner-Møller, S. Stobbe, A. Nysteen, J. Mørk, and P. Lodahl, *Measuring the effective phonon density of states of a quantum dot in cavity quantum electrodynamics*, Physical Review B, **88**, 045316 (2013).

Journal Publications in Preparation

1. K. H. Madsen, S. Ates, J. Liu, A. Javadi, and P. Lodahl, *Efficient generation of indistinguishable photons using phonon-mediated excitation of a quantum dot in a photonic-crystal cavity*. In preparation for submission.

Conference Contributions

1. K. H. Madsen, S. Ates, S. Reitzenstein, A. Forchel, and P. Lodahl, *Cavity quantum electrodynamics of a quantum dot in a micropillar cavity: com-*

parison between experiment and theory, NOEKS10, Paderborn, Germany, (2010).

2. K. H. Madsen, S. Ates, T. Lund-Hansen, A. Löffler, S. Reitzenstein, A. Forchel, and P. Lodahl, *Non-Markovian spontaneous emission from a single quantum dot*, Frontiers in Optics, San Jose, California, USA, (2011).

3. K. H. Madsen, S. Ates, T. Lund-Hansen, A. Löffler, S. Reitzenstein, A. Forchel, and P. Lodahl, *Observation of non-Markovian dynamics of a single quantum dot in a micropillar cavity*, CLEO/EQEC, Munich, Germany, (2011).

4. K. H. Madsen, P. Kaer, A. Kreiner-Møller, S. Stobbe, A. Nysteen, J. Mørk, and P. Lodahl, *Non-Markovian phonon dephasing of a quantum dot in a photonic-crystal nanocavity*, NOEKS11, Stuttgart, Germany, (2012).

Contents

Chapter 1

Introduction

In the last 100 years quantum theory has evolved from the initial description of the Hydrogen atom, signified by the Bohr model in 1913, to the state where individual quantum systems can be manipulated, for which Serge Haroche and David Wineland was awarded the 2012 Nobel Prize in Physics. Dirac laid the cornerstone of quantum optics by quantizing the electromagnetic field, which led to the realization that the vacuum electromagnetic field exhibits fluctuations around its mean zero amplitude. These fluctuations give rise to the Lamb shift and stimulate spontaneous emission. Since the foundation was laid, the field of quantum optics has progressed to the point, where the vacuum fluctuations can be modified and the light-matter interaction controlled as a number of ground breaking experiments on atoms demonstrated [1]. In addition, quantum optics has also been a testing ground for more fundamental aspects of quantum theory, which most notably includes the investigation of the Einstein-Podolsky-Rosen paradox [2] culminating with the violation of Bell's inequality [3] by Aspect et al. [4].

During this development, the field of solid-state physics evolved greatly and eventually saw one of the most influential inventions of the twentieth century, namely the transistor, which forms the fundamental building block of all modern electronics. Ever since, semiconductors have been the subject of an immense body of research, which eventually made the fabrication of devices that combine optics and electronics possible.

More recently quantum optics in solid-state materials has become a field in

its own right. This is largely due to the invention of self-assembled semiconductor quantum dots (QDs), where discrete electronic transitions give rise to the emission of single photons, which is a property normally attributed to single atoms. A crucial difference, however, stems from the semiconductor material the quantum dots are embedded in, which makes it possible to tailor the optical properties by utilizing the mature technology for fabrication in semiconductor materials. One of the main reasons for the intense research within this field is the prospect of using this as a platform for quantum-information processing.

The initial proposal for quantum cryptography [5] was based on having single photons available on-demand, and this spurred the interest in solid-state quantum optics. Later proposals for quantum computing [6] that rely on indistinguishable single photons on-demand fueled the interest in the research field further. While the solid-state environment does give rise to undesired effects such as decoherence, it also offers the prospect of scaling the individual systems and can thus form a platform for quantum-information processing. In addition to generating single photons, the engineering of the light-matter interaction, made possible by the solid-state platform, has been proposed to create a single-photon non-linearity [7, 8].

Although many proposals in solid-state quantum optics revolve around the application for quantum-information processing, it has also become clear that the interplay between otherwise disjunct fields of physics can be studied in this platform. Examples of this includes the emerging field of quantum optomechanics, where the ultimate quantum mechanical motion of, e.g., nanomembranes is studied [9].

In this thesis the coherent dynamics of quantum dots in photonic-crystal cavities is investigated. The coherence is determined by the environment experienced by the quantum dot, and this can be divided into two parts; a nanophotonic and a solid-state environment. The former modifies the vacuum fluctuations of the electromagnetic field and we probe it by measuring the spontaneous emission from quantum dots. The latter gives rise to decoherence of quantum dots, and we obtain information on the responsible mechanisms by measuring the coherence of the emitted photons.

The outline of the thesis is as follows:

In chapter 2 the basic concepts used throughout this thesis are introduced. First quantum dots are described with a focus on their electronic and optical

properties, and thereafter the concept of photonic crystals and in particular cavities are explained. Finally, the light-matter interaction of a quantum dot coupling to a cavity is described and the measurable quantities are derived.

In chapter 3 we study quantum dots embedded in two different types of cavities; a micropillar cavity and a photonic-crystal cavity. Both cavities alter the vacuum fluctuations experienced by the quantum dot significantly, and as a consequence the spontaneous emission from the quantum dots strongly depends on the cavity. We perform a quantitative analysis of the resulting dynamics and emission spectra by comparing them to the model for light-matter interaction derived in chapter 2.

Mechanical motion due to thermal vibrations, i.e. phonons, is omnipresent in solids, and in chapter 4 we investigate how phonons can alter the dynamics of a quantum dot in a photonic-crystal cavity. We investigate the interplay between the vacuum phonon field and the vacuum photon field, which allows us to extract detailed information on the solid-state environment.

We study how the single photons emitted from a quantum dot can be efficiently collected in Chapter 5, which is important for the use of quantum dots for quantum computing. The solid-state environment is examined further by investigating how phonons can assist in the excitation of the quantum dot. In an effort to understand how phonons cause decoherence of the emitted photons, we measure the indistinguishability, which is also of crucial importance for quantum information protocols.

In chapter 6 we describe how the quantum dot can be excited resonantly and thus without relying on the absorption of energy by the solid-state environment. The experimental setup is described, and a measurement showing resonant excitation is presented.

While detailed conclusion are presented in each chapter, we present a general conclusion in chapter 7.

Chapter 2

Quantum dots and photonic crystals

Photons are indivisible single quanta of light and thus constitute a quantum mechanical object. The laws of quantum mechanics allow for the unbreakable encryption of data saved in, e.g., the polarization of single photons [5], which has spurred a tremendous interest in the field of quantum cryptograph [10]. Implementation of such encryption schemes requires the triggered emission of single photons into a specific optical mode, a requirement that can be relaxed to the triggered emission of no or a single photon. Triggered generation of single photons has been demonstrated using a single atom [11], ion [12], molecule [13], nitrogen-vacancy (NV) center in diamond [14, 15], and semiconductor quantum dot (QD) [16, 17]. While the field of quantum cryptography has matured to the point, where commercial products utilizing quantum cryptography are now available, the overall field of quantum information processing is still in its infancy. The reason is that quantum information processing using linear optics [6] in addition to single photons requires the photons to be indistinguishable from each other, meaning that they have the same energy, coherence time, and optical mode [18, 19]. QDs are receiving much interest due to the possibilities of engineering the light-matter interaction by embedding them in photonic nanostructures that allow for the manipulation of the light-matter interaction. This offers both insight on the fundamental aspects of quantum mechanics as well as the promise of using a QD as a single-photon nonlin-

earity [7, 8]. While quantum computing can be done with linear optics that approach is inherently probabilistic in contrast to quantum computing using single-photon nonlinearities.

In this chapter we will discuss the basic properties of the self-assembled InAs QDs that are used throughout this work. The internal electronic structure will be described as well as the optical properties that form the basis of our understanding of QDs. We will then move on to describe the nanophotonic platform of photonic crystals and subsequently photonic-crystal cavities that are used for most of the work presented in this thesis. In the last part of this chapter we will present the theory for light-matter interaction and derive the theoretical expressions for measurable quantities such as the spectrum, the dynamics, and the second-order correlation function. In the final part we demonstrate how the local density of optical states (LDOS) picture normally used for describing spontaneous emission is equivalent to the density matrix description of a QD in an optical cavity up to the point where dephasing is introduced.

2.1 Electronic and optical properties of quantum dots

In this work III-V semiconductor quantum dots consisting of small islands of InAs embedded in GaAs are studied. Using the Stranski-Krastanov process quantum dots are grown by molecular beam epitaxy, where the GaAs substrate is initially grown crystal layer by crystal layer. Next InAs is introduced in the chamber, which has the same zinc-blende crystal structure as GaAs but a 7% larger lattice constant [20]. After a few monolayers of InAs have been grown, the lattice mismatch makes it energetically more efficient to form small islands ideally consisting of only InAs, but it may also contain some amount of Ga. Once these islands have been grown, they are capped by a layer of GaAs, causing them to be completely embedded in GaAs. The first monolayers of InAs that did not form islands make up the wetting layer, and a schematic of a quantum dot is shown in the left of Fig. 2.1. Due to the random manner in which the quantum dots are formed, the size of them will also differ with typical values being 15 nm in diameter and 5 nm in height.

2.1.1 Electronic states

Semiconductors are characterized by having an occupied valence band at low energies, in which electrons are bound, and an unoccupied conduction band at high energies, where electrons are free. In between these two bands no electronic states are allowed and this region is called the bandgap. Both InAs and GaAs have direct bandgaps meaning that the lowest energy state in the conduction band and the highest energy state in the valence band coincide at the point in the reciprocal lattice corresponding to an electron wavevector of zero ($\mathbf{k} = 0$). While a free electron has a quadratic dispersion relation, where the curvature gives the mass, the situation is in general much more complex in a crystal structure. However, around the point of the direct bandgap both the conduction and valence bands are approximately quadratic and the electrons can thus be described with the effective mass approximation [21].

For the energies considered here, there is a single conduction band with s-like symmetry, meaning that it has no orbital angular momentum in analogy to the atomic s-orbital. In contrast there are three valence bands, and they have p-like symmetry, meaning that they have orbital angular momentum of 1, again in analogy to the atomic p-orbitals. Two of these valence bands are degenerate at the $\mathbf{k} = 0$ point, while the third band is split off to much lower energies due to the spin-orbit coupling coupling, and it is consequently known as the split-off band. The two bands degenerate at the $\mathbf{k} = 0$ point have different effective masses and are thus called heavy-hole (HH) and light-hole (LH) bands. The spin-orbit coupling means that only the total angular momentum is conserved, and the projection of the total angular momentum onto the growth axis is $J_z = \pm 3/2$ and $J_z = \pm 1/2$ for the HH and LH bands, respectively [22]. Transitions between the valence and conduction bands are thus s to p transitions that are allowed electric dipole transitions following the selection rules. Optical excitation of a semiconductor can thus occur by the absorption of a photon with an energy higher than the bandgap energy, which results in an electron being promoted to the conduction band [23]. The electron leaves behind an unoccupied state in the valence band called the hole, which is described as a quasi-particle also with an effective mass. The electron and hole are created at the same spatial position and due to their opposite charges they can attract each other through the Coulomb force and form an excition, which is annihilated when the electron and hole recombine by emission of a photon or through

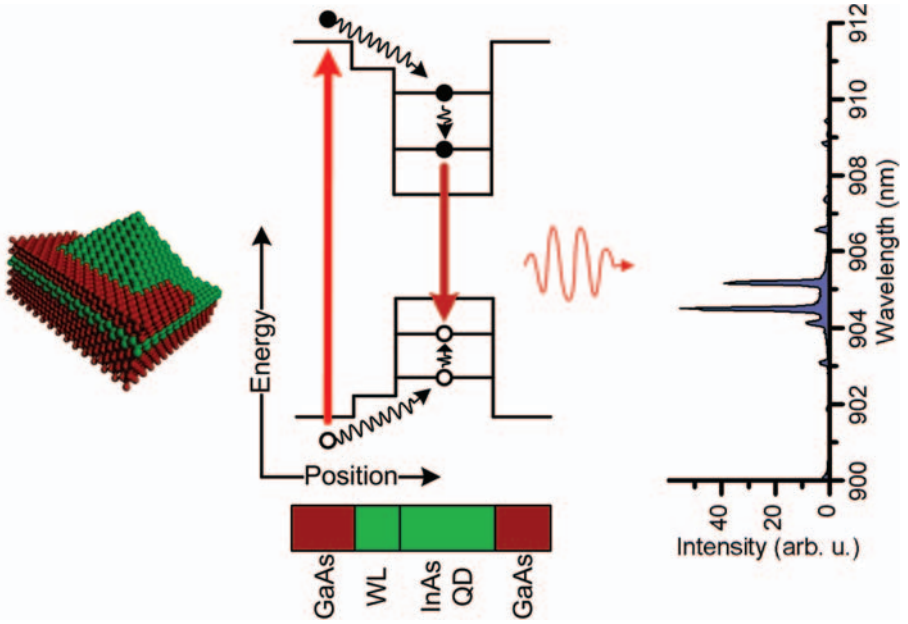

Figure 2.1: Left: Sketch of an InAs quantum dot embedded in GaAs with a thin InAs wetting layer (WL). Middle: Creation of an exciton in the GaAs that relaxes down to the s-shell before recombining optically. Right: Example of a recorded emission spectrum showing a strong exciton line.

non-radiative processes [23].

A sketch of the energy at the point of the direct bandgap ($\mathbf{k} = 0$ point) as a function of position for the quantum dot is shown in Fig. 2.1, where there is a continuum of electronic states in the GaAs and in the InAs wetting layer. Due to the small dimensions of the InAs QD, a potential well in all three spatial dimensions is created, where only discrete states are allowed. Strain during the growth of the QD lifts the degeneracy of the heavy-hole and light-hole bands by shifting the latter down in energy by several tens of meV [24]. The highest energy state in the valence band thus becomes the heavy-hole, and only transitions between the heavy-hole and conduction band will be considered in this work. The size of the QD allows for a confined ground state for both the electron and hole with the lowest and highest energy state in the conduction and valence band, respectively. These states are termed *s*-states due to their

symmetry, and the size of the QD even allows for the confinement of higher and lower energy states in the conduction and valence band, respectively, named p-states. We can use Bloch's theorem to divide the potential of the crystal into an atomic-scale potential, which is periodic with the crystal lattice, and a macroscopic potential, which follows the spatial dependence of the QD. Using this we can write the electron and hole wavefunctions as

$$\psi_{\mathrm{e}}(\mathbf{r}) = F_{\mathrm{e}}(\mathbf{r}) \cdot u_{\mathrm{c}}(\mathbf{r}) \quad \text{and} \quad \psi_{\mathrm{h}}(\mathbf{r}) = F_{\mathrm{h}}(\mathbf{r}) \cdot u_{\mathrm{v}}(\mathbf{r}) \quad , \tag{2.1}$$

where $F_{e,h}(\mathbf{r})$ are the envelope functions for the electron and hole that satisfy Schrödinger's equation using the macroscopic potential, and $u_{c,v}(\mathbf{r})$ are the Bloch functions for the conduction and valence bands that satisfy Schrödinger's equation using the atomic-scale potential [25]. Both envelope functions for the ground states have s-symmetry, while the conduction band has s-symmetry and the valence band has p-symmetry, as discussed. As a result the electron wavefunction has s-symmetry and the hole wavefunction has p-symmetry. This means that only transitions between the s-states or between the p-states are allowed in the QD following the selection rules. It is noted that the sizes of the electron and hole wavefunctions are typically smaller than the size of the QD extracted from scanning electron microscopy (SEM), and in chapter 4 these sizes are extracted. Furthermore, the QDs studied in this work are small, meaning that the exciton in the QD is bound by the confinement potential and not the Coulomb force, and consequently the electrons and holes are moving independently.

The Pauli exclusion principle ensures that only two electrons and two holes with opposite spins can occupy the s-states of the QD [26]. If two excitons are present in the QD, the energy of the exciton that first recombines radiatively will be shifted due to the Coulomb interaction of the two excitons, and this is denoted the bi-exciton. This ensures that any radiative recombination at the exciton energy will result in single photon emission. An example of an emission spectrum from a QD is shown in the right of Fig. 2.1, where the verification of the single photon nature of the emission is presented in chapter 5. The ground state exciton has an electron with a projected total angular momentum of $J_z = \pm 1/2$ and a hole with $J_z = \pm 3/2$, which results in four possible exciton states with $J_z = \pm 1$ and $J_z = \pm 2$. Single photons are circularly polarized and have an angular momentum of 1, meaning that the two former states are bright

states that can decay radiatively while the two latter states are dark states that can only decay nonradiatively. However, when the symmetry of the exciton wavefunctions in the plane orthogonal to the growth direction is broken, the two bright states mix with each other due to the long-range exchange interaction. As a result, the two bright states become linearly polarized and obtain a fine structure splitting in energy of typically a few tens of μeV, while the degeneracy of the dark excitons is lifted by the short-range exchange interaction and both lie a few hundred μeV below the bright states [24]. Typically the in-plane symmetry of the confinement potential is broken due to strain of the lattice during the growth of the QD, as is the case for all the QD samples used in this work [27]. The two resulting linear dipoles will be oriented preferably along the crystal directions. The decay of a bright exciton has a radiative γ_{rad} and nonradiative γ_{nrad} contribution to the decay rate. However, the bright state is coupled to the dark state through the spin-flip rate γ_{bd}, where the spin of a single electron or hole is flipped mediated by phonons and exchange interaction causing the exciton to become dark. The QD is thus a five-level system with two bright excitons, two dark excitions and a ground state consisting of no excitons. However, because the effective mass of the electron is much smaller than that of the hole, spin-flip processes will predominantly flip the electron spin, and the five-level system can be separated into two three-level systems each consisting of a bright and dark exciton and a ground state, cf. Fig. 2.2. Previous work has shown that the nonradiative decay rate of bright ($\gamma^{\mathrm{b}}_{\mathrm{nrad}}$) and dark ($\gamma^{\mathrm{d}}_{\mathrm{nrad}}$) states can be assumed equal, and that the spin-flip rates from bright to dark and the reverse (γ_{bd} and γ_{db}) likewise can be assumed equal, because the thermal energy is much larger than the bright-dark energy splitting [28]. Finally, the spin-flip rates are much slower than both radiative and non-radiative processes [29], which means that the measured decay of a QD will be bi-exponential of the form $A_{\mathrm{fast}}\mathrm{e}^{-\gamma_{\mathrm{fast}}t} + A_{\mathrm{slow}}\mathrm{e}^{-\gamma_{\mathrm{slow}}t}$. Here $\gamma_{\mathrm{fast}} = \gamma_{\mathrm{rad}} + \gamma_{\mathrm{nrad}}$ and $\gamma_{\mathrm{slow}} = \gamma_{\mathrm{nrad}}$, where γ_{rad} is the radiative and γ_{nrad} is the nonradiative decay rate. From experimental decay curves the radiative decay rate can thus be extracted as the difference $\gamma_{\mathrm{rad}} = \gamma_{\mathrm{fast}} - \gamma_{\mathrm{slow}}$.

The discussion so far has resulted in the QD being considered a three-level system, but the solid-state environment also gives rise to a number of features that are unique to solid-state quantum states, of which the most predominant effect is decoherence. Phonons are omnipresent in solids and the interaction

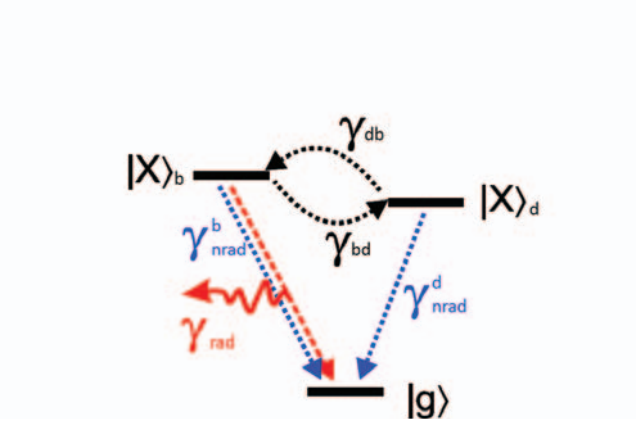

Figure 2.2: Three-level system of the QD with a bright state $|\mathrm{X}\rangle_\mathrm{b}$ that decays with the radiative rate γ_rad and the nonradiative rate $\gamma^\mathrm{b}_\mathrm{nrad}$ to the ground state $|\mathrm{g}\rangle$. The dark state $|\mathrm{X}\rangle_\mathrm{d}$ only decays with a nonradiative rate $\gamma^\mathrm{d}_\mathrm{nrad}$. The bright and dark states are coupled through the spin-flip rates γ_bd and γ_db.

of the bright exciton with lattice phonons has been shown to broaden the spectral linewidth of the QD significantly. By phonon-assisted recombination of the exciton, part of the exciton energy is sent into the lattice by spontaneous emission of acoustic phonons, giving rise to a phonon sideband on the low energy side [30]. However, part of this sideband extends to the higher energy side of the bright state, because the thermal occupation of low-energy phonons is not negligible even at cryogenic temperatures, e.g. 10 K, and absorption as well as stimulated emission of phonons are present. These processes will be discussed in detail in chapter 4, where the experimental evidence for these processes in the setting of cavity quantum electrodynamics is presented, and in chapter 5, where the decoherence resulting from different phonon-mediated excitation schemes is discussed. Acoustic phonons can also couple the QD with free carriers outside the QD and this has been shown to give rise to further broadening of the exciton emission line [31, 32]. Furthermore, the energy levels of the QD are easily shifted by fluctuations of the electrostatic environment that can also broaden the QD linewidth. This will typically happen on a timescale much slower than the dynamics of the QD, but recent work has indicated that these processes can take place also on the timescale of the dynamics [33]. Finally, the presence of carriers in the wetting layer continuum, e.g. generated under continuous wave excitation, can give rise to shifts in the exciton energy through the Coulomb interaction. This is essentially a scattering process, where

excitons scatter off carriers in the wetting layer continuum, and as a result a quasi-continuum of states is formed around the s-state exciton energy. In an emission spectrum this quasi-continuum, also known as multiexcitons, is orders of magnitude weaker than the bare exciton transition [34, 35], but it becomes significant in cavity quantum electrodynamics, where the cavity can strongly enhance the effect [36].

2.1.2 Spontaneous emission

An exciton confined in the QD can recombine optically by spontaneous emission of a single photon. In order to describe this process we need to introduce both the quantized matter, i.e. the QD, and the quantized radiation field. By considering only the bright exciton, a QD can be described as a two level system, where the excited state, $|e\rangle$, corresponds to an excition in the s-shell of the QD, while the ground state, $|g\rangle$, corresponds to no exciton. The frequency difference between these two states is denoted ω_{qd} and we introduce the atomic lowering and raising operators $\hat{\sigma}_- = |g\rangle\langle e|$ and $\hat{\sigma}_+ = |e\rangle\langle g|$. The hamiltonian for a non-interacting two-level system can be written $\hat{\mathrm{H}}_{\mathrm{qd}} = \hbar\omega_{\mathrm{qd}}\hat{\sigma}_+\hat{\sigma}_-$, where the zero point energy level has been placed at the ground state. Similarly, the exciton can decay into the kth optical mode, thereby rasing it from the ground state of no photon, $|0_k\rangle$, to the state of a single photon, $|1_k\rangle$, with frequency ω_{k}. The Hamiltonian for the field is given by $\hat{\mathrm{H}}_{\mathrm{field}} = \hbar\sum_{\mathrm{k}}\omega_{\mathrm{k}}\hat{a}_{\mathrm{k}}\hat{a}_{\mathrm{k}}^\dagger$, and the zero point energy has been omitted for each mode.

The interaction between the QD and the optical field can be described as an electric dipole interaction with a hamiltonian given by $\hat{\mathrm{H}}_{\mathrm{I}} = -\hat{\mathbf{d}}\cdot\hat{\mathbf{E}}(\mathbf{r_0})$, where $\hat{\mathbf{d}}$ is the QD electric dipole moment. $\hat{\mathbf{E}}(\mathbf{r_0})$ is the electric field evaluated at the position of the QD, where we have made use of the dipole approximation stating that the electric field can be assumed constant over the size of the exciton wavefunction. Though recent work has shown that this approximation can break down for QDs [37], it remains a good approximation for the QDs considered in this work, where the sizes of the exciton wavefunction extracted in chapter 4 are much smaller than the variation of the electric field. The electric field operator for a quantized multimode field can be written [38]

$$\hat{\mathbf{E}}(\mathbf{r},t) = \sum_{\mathrm{k}} E_{\mathrm{k}}\left(\hat{a}_{\mathrm{k}}(t)\mathbf{f}_{\mathrm{k}}(\mathbf{r}) + \hat{a}_{\mathrm{k}}^\dagger(t)\mathbf{f}_{\mathrm{k}}^*(\mathbf{r})\right) \quad , \tag{2.2}$$

where $E_{\mathrm{k}} = \sqrt{\hbar\omega_{\mathrm{k}}/(2\epsilon_0 n^2 V)}$ and n is the refractive index, ϵ_0 is the vacuum

permittivity, and V is the effective mode volume. $\mathbf{f}_{\mathrm{k}}(\mathbf{r}) = \hat{\mathbf{e}}_{\mathrm{k}}(\mathbf{r}) f_{\mathrm{k}}(\mathbf{r})$ where the first part describes the polarization, and the second part describes the relative field amplitude normalized to give unity at the maximum of the electric field, $|f(\mathbf{r})|_{\max} = 1$.

The dipole moment of the QD can be written

$$\hat{\mathbf{d}} = \mathbf{d}_{\mathrm{eg}}\hat{\sigma}_{+} + \mathbf{d}^{*}_{\mathrm{eg}}\hat{\sigma}_{-} \quad , \tag{2.3}$$

where $\mathbf{d}_{\mathrm{eg}} = \langle e|\hat{\mathbf{d}}|g\rangle$ is the transition dipole moment. Inserting Eq.(2.2) and (2.3) into the interaction hamiltonian yields

$$\hat{\mathrm{H}}_{\mathrm{I}} = \hbar \sum_{\mathrm{k}} (g_{\mathrm{k}}\hat{\sigma}_{+}\hat{a}_{\mathrm{k}} + g^{*}_{\mathrm{k}}\hat{\sigma}_{-}\hat{a}^{\dagger}_{\mathrm{k}}) \quad , \tag{2.4}$$

where $g_{\mathrm{k}} = -\hbar^{-1} E_{\mathrm{k}} \mathbf{d}_{eg} \cdot \mathbf{f}_{\mathrm{k}}(\mathbf{r}_0)$ is the light-matter interaction strength. We have applied the rotating wave approximation, meaning that we have discarded the counter rotating terms that do not preserve the energy ($\hat{\sigma}_{-}\hat{a}_{\mathrm{k}}$ and $\hat{\sigma}_{+}\hat{a}^{\dagger}_{\mathrm{k}}$ terms). The full hamiltonian for the system can now be written

$$\hat{H} = \hbar\omega_{\mathrm{qd}}\hat{\sigma}_{+}\hat{\sigma}_{-} + \hbar \sum_{\mathrm{k}} \omega_{\mathrm{k}}\hat{a}_{\mathrm{k}}\hat{a}^{\dagger}_{\mathrm{k}} + \hbar \sum_{\mathrm{k}} (g_{\mathrm{k}}\hat{\sigma}_{+}\hat{a}_{\mathrm{k}} + g^{*}_{\mathrm{k}}\hat{\sigma}_{-}\hat{a}^{\dagger}_{\mathrm{k}}) \quad . \tag{2.5}$$

The state vector relevant for this system can now be written

$$|\Psi(t)\rangle = c_{\mathrm{e}}(t)|e, 0_{\mathrm{k}}\rangle + \sum_{\mathrm{k}} c^{\mathrm{k}}_{\mathrm{g}}(t)|g, 1_{\mathrm{k}}\rangle \quad , \tag{2.6}$$

where the first term corresponds to an excited QD and no photon in any of the k modes, while the second term corresponds to no exciton and a photon emitted into the multimode field. We now insert the state vector and the full hamiltonian into the Schrödinger equation, and by projecting onto the states $|e, 0_{\mathrm{k}}\rangle$ and $|g, 1_{\mathrm{k}}\rangle$ we obtain the following two equations

$$\frac{d}{dt}\tilde{c}_{\mathrm{e}}(t) = -i \sum_{\mathrm{k}} g_{\mathrm{k}}\tilde{c}^{\mathrm{k}}_{\mathrm{g}}(t)\mathrm{e}^{i(\omega_{\mathrm{qd}}-\omega_{\mathrm{k}})t} \quad , \tag{2.7}$$

$$\frac{d}{dt}\tilde{c}^{\mathrm{k}}_{\mathrm{g}}(t) = -ig^{*}_{\mathrm{k}}\tilde{c}_{\mathrm{e}}(t)\mathrm{e}^{-i(\omega_{\mathrm{qd}}-\omega_{\mathrm{k}})t} \quad , \tag{2.8}$$

where the slowly varying time operators $\tilde{c}_{\mathrm{e}}(t) = c_{\mathrm{e}}(t)\mathrm{e}^{i\omega_{\mathrm{qd}}t}$ and $\tilde{c}^{\mathrm{k}}_{\mathrm{g}}(t) = c^{\mathrm{k}}_{\mathrm{g}}(t)\mathrm{e}^{i\omega_{\mathrm{k}}t}$ have been introduced. Direct integration of Eq. (2.8) and insertion into Eq. (2.7)

gives

$$\frac{d}{dt}\tilde{c}_{\mathrm{e}}(t) = -\int_0^t \sum_{\mathrm{k}} |g_{\mathrm{k}}|^2 \tilde{c}_{\mathrm{e}}(t') \mathrm{e}^{i(\omega_{\mathrm{qd}}-\omega_{\mathrm{k}})(t-t')} dt' \quad . \tag{2.9}$$

Finally, we introduce a frequency integral together with a delta function and insert the expression for the coupling strength which yields

$$\frac{d}{dt}\tilde{c}_{\mathrm{e}}(t) = -\frac{|\mathbf{d}_{\mathrm{eg}}|^2}{2\hbar\epsilon_0} \int_0^t \int_{-\infty}^{\infty} \omega \rho(\omega, \mathbf{r}_0, \hat{\mathbf{e}}_{\mathrm{qd}}) \tilde{c}_{\mathrm{e}}(t') \mathrm{e}^{i(\omega_{\mathrm{qd}}-\omega)(t-t')} d\omega dt' \quad , \tag{2.10}$$

where $\hat{\mathbf{e}}_{\mathrm{qd}}$ is the dipole orientation and the projected local density of optical states (LDOS) is defined as

$$\rho(\omega, \mathbf{r}_0, \hat{\mathbf{e}}_{\mathrm{qd}}) = \sum_{\mathrm{k}} \frac{|f_{\mathrm{k}}(\mathbf{r}_0)|^2}{n^2 V} |\hat{\mathbf{e}}_{\mathrm{qd}} \cdot \hat{\mathbf{e}}_{\mathrm{k}}|^2 \delta(\omega - \omega_{\mathrm{k}}) \quad . \tag{2.11}$$

Eq. (2.10) gives a powerful relation that describes the dynamics of a QD (or any two-level emitter), where the first part of the equation contains the key QD property, namely the size of the transition dipole moment, and the second part contains all information of the local optical environment described by the LDOS. In the Wigner-Weisskopf approximation the LDOS varies slowly over the linewidth of the QD, and it can be pulled outside the frequency integral and evaluated at the QD frequency. This results in an exponential decay of the QD with the decay rate $\Gamma = \frac{\pi |\mathbf{d}_{\mathrm{eg}}|^2}{\hbar\epsilon_0} \omega_{\mathrm{qd}} \rho(\omega_{\mathrm{qd}}, \mathbf{r}_0, \hat{\mathbf{e}}_{\mathrm{qd}})$. In a homogenous medium the LDOS does not depend on $\mathbf{r}_0$ or $\hat{\mathbf{e}}_{\mathrm{qd}}$ due to the symmetry and it can be calculated to give $\rho(\omega) = \frac{n\omega^2}{3\pi^2 c^3}$. The decay rate in a homogenous medium is thus

$$\Gamma_{\mathrm{hom}} = \frac{|\mathbf{d}_{\mathrm{eg}}|^2 n \omega_{\mathrm{qd}}^3}{3\epsilon_0 \hbar \pi c^3} \quad . \tag{2.12}$$

In section 2.4.4 the equivalence of the LDOS description to the celebrated Jaynes-Cummings model is described and the limitations of the LDOS approach are highlighted.

2.2 Photonic crystals

In the previous section we saw that the dynamics of a QD depends on both the size of the transition dipole moment and the local optical environment.

While the former is hard to control due to the randomness of the growth, the latter can be carefully engineered. There is an immense body of research on semiconductors and we can draw on this very mature technology for the fabrication of nanostructures around the QDs.

The principle of photonic crystals can be understood by considered the one-dimensional system of a Bragg reflector, where alternating layers of high and low refractive index materials are placed periodically along the propagation direction of the electric field [39, 40]. While the dispersion relation in a homogenous medium is given by $\omega = ck/n$ allowing for optical modes at all frequencies, the periodicity of this structure introduce a photonic bandgap, where no optical modes are allowed, and the bandgap widens when increasing the refractive index difference. It should be pointed out, that while no extended states are allowed, evanescent states that decay exponentially into the photonic crystal do exist for crystals of finite extent. However, the bandgap only exists for waves propagating orthogonally to the plane of the layers and by considering off-axis propagation optical modes become present within the bandgap. This one-dimensional system can be generalized to two-dimensions by introducing holes in a otherwise homogenous dielectric material. The rods of air are ordered in a triangular lattice, which is characterized by the hole radius r and lattice constant a, cf. Fig. 2.3. For certain values of r/a this structure introduces a complete bandgap, where both TE and TM polarized light propagating within the plane are not present [41]. Light propagating orthogonal to this plane is still allowed, causing the LDOS to not completely vanish. We consider a membrane that is thin in the direction orthogonal to the plane of the photonic crystal. The GaAs-air interface gives rise to total internal reflection of fields with an incident angle larger than approximately 17 degrees, and for smaller angles the fields are still partly reflected due to the high-low refractive index interface. The strong suppression of optical modes makes the LDOS and thus the decay rate of the QD strongly suppressed with inhibition factors up to 70 [28], and for this reason the photonic-crystal membrane is said to have a pseudo-bandgap.

As described earlier, the QDs are grown by depositing single atomic layers using molecular beam epitaxy on a GaAs-wafer. When the growth of the sample is finished, the structure, from the bottom and up, consists of; the GaAs-wafer, a 1530 nm sacrificial layer of AlGaAs, 77 nm of GaAs, the InAs QD layer,

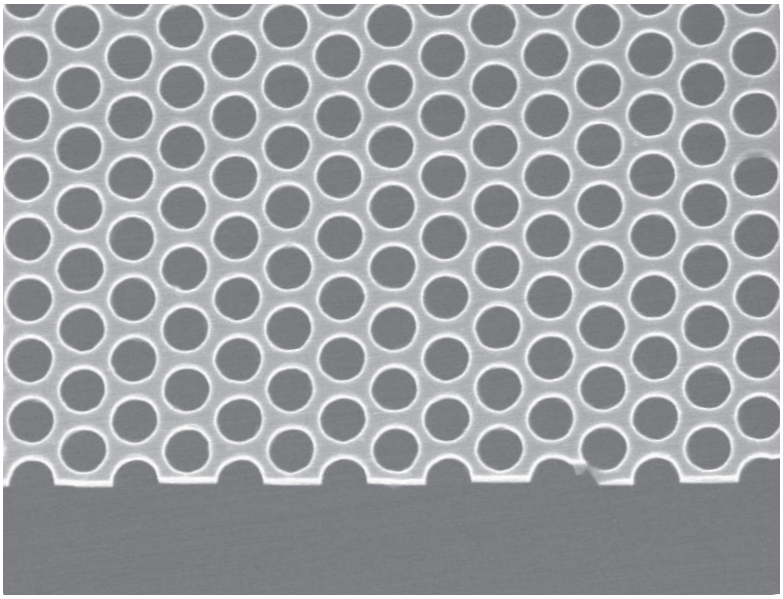

Figure 2.3: Scanning electron microscope image of a cleaved photonic-crystal membrane.

and finally 77 nm of GaAs. We now give a short outline of how the photonic crystal is made. First an etch mask is deposited, followed by deposition of an electron beam resist. Thereafter, the photonic-crystal pattern is written with high precision using electron beam lithography. Reactive ion etching is now used to remove the etch mask followed by removal of the electron beam resist. By inductively coupled plasma reactive ion etching of the wafer, the air rods are now etched in the GaAs. Finally, the sacrificial layer is removed by selective underetching, and the photonic-crystal membrane remains [42], cf. Fig. 2.3. Typical values for the lattice parameters in our samples are $r/a = 0.28$ and $a = 260$ nm, which ensures the aforementioned pseudo-bandgap for the TE modes. In order to obtain the bandgap for both the TE and the TM modes a higher r/a-ratio is needed, e.g. a complete bandgap exists for $r/a = 0.48$ [41], but because such structures contain little material they often collapse and are thus very difficult to fabricate. It has, however, been shown that a complete bandgap can be achieved by not having symmetric rods but rather triangles [43].

Finally we note that Maxwell's equations for dielectric media are scalable. The properties of a photonic crystal are thus solely given by r and a, and any design can be scaled to fit the wavelength of the QD.

2.3 Photonic-crystal cavities

By introducing a defect in the photonic crystal, we can create a localized mode with a frequency in the bandgap. Such a localized mode will be strongly bound to the defect and decay exponentially into the photonic crystal. The photonic crystal acts like a 2D frequency-specific mirror, and because the confinement is on the order of the wavelength the modes are discrete [41]. Such defects can be realized in many ways, and examples include removing three holes which is denoted an L3 defect [44], removing one hole which is denoted an H1 defect [45], and not removing but rather shifting some of the holes which is denoted an H0 defect [46]. In the following we will focus on the first of the above.

2.3.1 Confining light

The L3 cavity is formed by leaving out three air holes along a vertical line in Fig. 2.4. The frequency of the localized mode lies within the bandgap, which gives rise to a high quality (Q) factor, that is defined as $Q = \omega_{\mathrm{ca}}/\kappa$, where ω_{ca} is the center frequency of the cavity and κ is the decay rate of the cavity. Furthermore, because the cavity mode is strongly localized around the position of the defect that is on the nanoscale, the effective mode volume of the cavity becomes on the order of the wavelength, $V \sim 0.7(\lambda_0/n)^3$ [47]. This is particularly important, because the light-matter interaction strength depends on the ratio Q/V, as will be shown in the next section.

The discretization of modes gives rise to six optical modes of the L3 cavity, where the mode with the lowest frequency (M1) has the highest Q-factor and the lowest mode volume. Simply omitting three holes does give rise to a localized mode, but the Q-factors are rather low. This can be understood by considering the very abrupt change in the envelope function of the electric field that occurs at the edges of the cavity. As a result, the Fourier transform of the electric field has a large component at small wavevectors that corresponds to out-of-plane leaky modes. By shifting the position of the holes at the ends of the cavity, the electric field envelope function becomes much smother, and the

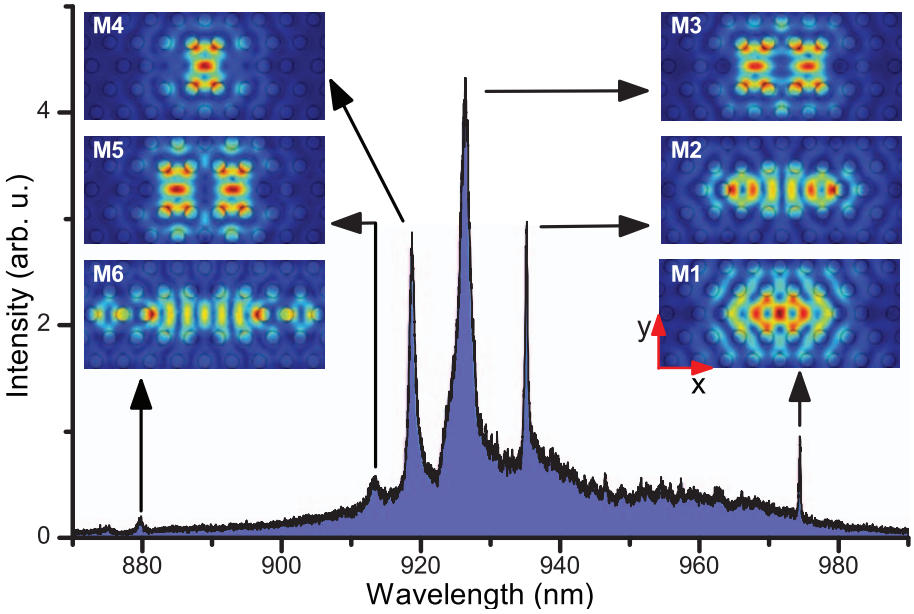

Figure 2.4: Emission spectrum from an L3 photonic-crystal cavity. The optical modes are labeled M1-M6 and the insets show the norm of the corresponding simulated electric fields. M1, M2, M4, and M6 are all y-polarized in the far-field, while M3 and M5 are x-polarized.

Fourier transform of the field has only very small components inside this leaky region. This is known as gentle confinement of the light [44], and it greatly increases the Q-factor while the mode volume stays small. In our samples we have shifted the first three holes at the ends of the cavity by 0.175a, 0.025a, and 0.175a, respectively [47].

In Fig. 2.4 the emission spectra from an L3 cavity is shown, where the optical modes are labeled (M1-M6), and the corresponding simulated electric fields are also shown. The modes M1, M2, M4, and M6 are all co-polarized along the y-axis in the far-field, while M3 and M5 show the orthogonal polarization along the x-axis in the far-field. The modes M1, M2, and M4 typically have Q-factors in the range $3000 - 7000$ in our sample, with M1 always having the highest, while the modes M3, M5, and M6 all have low Q-factors around 500 and below.

2.4 Light-matter interaction in a cavity

The study of single QDs embedded in cavities is the main focus of this thesis and in order to capture all the quantum mechanical features of the interaction, we need to apply a fully quantized theory to describe both the QD and the electric cavity field. In section 2.1.2 the spontaneous emission of a QD into a continuum of modes was described, whereas we now describe the cavity field as a single quasi-mode and consider the interaction with a QD two-level system using the celebrated Jaynes-Cummings (JC) model [48].

2.4.1 Jaynes-Cummings model

Whereas spontaneous emission was described in the Schrödinger picture, the following theory will be described in the density matrix picture. As we shall see later, this is done to allow for the inclusion of mixed states, i.e. classical uncertainties. We start by considering the full hamiltonian from Eq. (2.5), but for only a single mode of the electric field:

$$\begin{aligned} \hat{H} &= \hat{H}_{\mathrm{qd}} + \hat{H}_{\mathrm{field}} + \hat{H}_{\mathrm{I}} \\ &= \hbar\omega_{qd}\hat{\sigma}_+\hat{\sigma}_- + \hbar\omega_{\mathrm{ca}}\hat{a}^\dagger\hat{a} + \hbar(g\hat{\sigma}_+\hat{a} + g^*\hat{\sigma}_-\hat{a}^\dagger) \quad . \end{aligned} \tag{2.13}$$

This hamiltonian can be simplified by moving into a frame rotating with the frequency of the cavity field ω_{ca}, which is equivalent to the introduction of slowly varying operators done in the Schrödinger picture in section 2.1.2. By insertion into the Schrödinger equation it is easily verified, that a unitary transformation, $U(t)$, of a state vector is equivalent to transforming the hamiltonian in the following way:

$$\hat{H}_{\mathrm{rot}} = \hat{U}^\dagger(t)\hat{H}\hat{U}(t) - i\hbar\hat{U}^\dagger(t)\frac{d}{dt}\hat{U}(t) \quad . \tag{2.14}$$

The unitary operator needed in this case is $\hat{U}(t) = \mathrm{e}^{-i\omega_{\mathrm{ca}}(\hat{\sigma}_+\hat{\sigma}_- + \hat{a}^\dagger\hat{a})t}$ and the hamiltonian in this new rotating frame becomes

$$\hat{H}_{\mathrm{rot}} = \hbar\Delta\hat{\sigma}_+\hat{\sigma}_- + \hbar(g\hat{\sigma}_+\hat{a} + g^*\hat{\sigma}_-\hat{a}^\dagger) \quad , \tag{2.15}$$

where $\Delta = \omega_{\mathrm{qd}} - \omega_{\mathrm{ca}}$. From now on the subscript will be dropped as we are consistently within the rotating frame. The above hamiltonian captures all the features of the coherent light-matter interaction, but in a real physical

system dissipation is always present. We may think of the density matrix, that includes the QD and cavity field, as a reduced density matrix for our system, $\hat{\rho}_{\mathrm{S}} = \mathrm{Tr}_{\mathrm{R}}\hat{\rho}_{\mathrm{SR}}$, where the reservoir has been traced out of the complete density matrix $\hat{\rho}_{\mathrm{SR}}$. Solutions to the equation of motion should be of the form [49]

$$\hat{\rho}_{\mathrm{SR}}(t) = \hat{\rho}_{\mathrm{S}}(t) \otimes \hat{\rho}_{\mathrm{R}}(t_i) + \hat{\rho}_{\mathrm{c}}(t) \ , \tag{2.16}$$

where $\rho_{\mathrm{R}}(t_i)$ is the state of the reservoir at initial time t_i where the interaction starts, and the system-reservoir interaction energy has been assumed small. The contribution to the density matrix, $\hat{\rho}_{\mathrm{c}}(t)$, arises from the interaction between the system and reservoir and if the interaction is set to zero, the subsystems are independent. Instead of using this equation to obtain the time evolution of the subsystem consisting of the QD and cavity field, we turn to a general framework known as the Markov master equation of Lindblad form [50]. The density matrix must be Hermitian, nonnegative, and of unit trace. A general concern when including dissipation phenomenologically is that these criteria for the density matrix may no longer be fulfilled. However, if the dissipation process associated with the operator $\hat{R}$ occurs on a faster timescale than the rest of the dynamics and with a magnitude of Γ, then Lindblad terms of the form $\mathcal{L}(\Gamma, \hat{R}) = \Gamma\left(\hat{R}\hat{\rho}\hat{R}^{\dagger} - \frac{1}{2}\hat{R}^{\dagger}\hat{R}\hat{\rho} - \frac{1}{2}\hat{\rho}\hat{R}^{\dagger}\hat{R}\right)$ can be added to the equation governing the time evolution of the density matrix, without violating any of the criteria for the density matrix [51]. We thus write the master equation for the density matrix operator as [52]

$$\dot{\rho} = -i\hbar^{-1}[\hat{H}, \rho] + \mathcal{L}(\kappa, \hat{a}) + \mathcal{L}(\gamma, \hat{\sigma}_{-}) + \mathcal{L}(\gamma_{\mathrm{dp}}/2, \hat{\sigma}_{\mathrm{z}}) \ , \tag{2.17}$$

where $\hat{\sigma}_{\mathrm{z}} = [\hat{\sigma}_{+}, \hat{\sigma}_{-}]$. As indicated in the sketch in Fig. 2.5, the first term is responsible for the coherent light-matter interaction, where a QD can decay by emitting into the cavity and if the coupling is strong enough the single photon in the cavity can be reabsorbed by the QD, and the excitation thus coherently oscillates back and forth. The three last terms correspond to dissipation of the cavity, dissipation of the QD, and decoherence of the QD, respectively. Cavity dissipation is due to imperfect confinement of the light and the cavity decay rate is given by $\kappa = \omega_{\mathrm{ca}}/Q$. Although other modes are strongly inhibited by the photonic crystal, the QD can still emit into radiation modes, which is included as the decay rate γ. Finally, the decoherence of the exciton is included as a pure dephasing rate, γ_{dp}, which corresponds to white noise on the exciton energy level, caused by e.g. phonons or changes in the electrostatic environment.

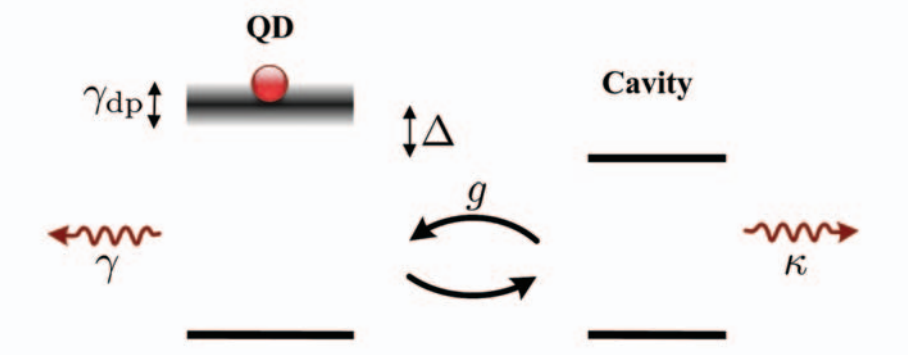

Figure 2.5: Schematic of the dissipative Jaynes-Cummings model, where both the QD and cavity are described as two-level systems. The QD is initially excited, and it is dephased by the pure dephasing rate γ_{dp} and decays to the environment with the decay rate γ. The QD is detuned by Δ from the cavity, and it couples coherently to the cavity with the coupling strength g. The losses of the cavity are given by the decay rate κ.

Equations of motion

It is necessary to choose a representation of the master equation, where the QD and field operators commute. A complete basis spanned by the states $\{|e,1\rangle, |g,1\rangle, |e,0\rangle, |g,0\rangle\}$ is chosen and the operators are given by

$$\hat{a} = \begin{pmatrix} 0 & 0 \\ 1 & 0 \end{pmatrix} \otimes \mathbb{I} \quad \text{and} \quad \hat{\sigma}_- = \mathbb{I} \otimes \begin{pmatrix} 0 & 0 \\ 1 & 0 \end{pmatrix} \tag{2.18}$$

In this complete basis the master equation becomes:

$$\dot{\rho} = \begin{pmatrix} 0 & 0 & 0 & 0 \\ 0 & ig\rho_{23} - ig^*\rho_{32} & i\Delta\rho_{23} + ig^*(\rho_{22} - \rho_{33}) & -ig^*\rho_{34} \\ 0 & -i\Delta\rho_{32} - ig(\rho_{22} - \rho_{33}) & ig^*\rho_{32} - ig\rho_{23} & -i\Delta\rho_{34} - ig\rho_{24} \\ 0 & ig\rho_{43} & i\Delta\rho_{43} + ig^*\rho_{42} & 0 \end{pmatrix}$$
$$+ \begin{pmatrix} 0 & 0 & 0 & 0 \\ 0 & -\kappa\rho_{22} & -\frac{\gamma+\kappa+2\gamma_{\mathrm{dp}}}{2}\rho_{23} & -\frac{\kappa}{2}\rho_{24} \\ 0 & -\frac{\gamma+\kappa+2\gamma_{\mathrm{dp}}}{2}\rho_{32} & -\gamma\rho_{33} & -\frac{\gamma+2\gamma_{\mathrm{dp}}}{2}\rho_{34} \\ 0 & -\frac{\kappa}{2}\rho_{42} & -\frac{\gamma+2\gamma_{\mathrm{dp}}}{2}\rho_{43} & \kappa\rho_{22} + \gamma\rho_{33} \end{pmatrix} \tag{2.19}$$

The elements $\{\rho_{11}, \rho_{22}, \rho_{33}, \rho_{44}\}$ correspond to the populations of the states $\{|e,1\rangle, |g,1\rangle, |e,0\rangle, |g,0\rangle\}$. We restrict to consider only a single excitation in the system, which is the reason why element ρ_{11} is zero in Eq. (2.19) and does not couple to the other elements. The first matrix in Eq. (2.19) captures the coherent light-matter interaction, while the second matrix originates from the dissipative Lindblad terms. The dynamics of the populations of the QD and cavity field make out a subset and are governed by the following equation:

$$\begin{pmatrix} \dot{\rho}_{22} \\ \dot{\rho}_{23} \\ \dot{\rho}_{32} \\ \dot{\rho}_{33} \end{pmatrix} = \begin{pmatrix} -\kappa & ig & -ig^* & 0 \\ ig^* & i\Delta - \frac{\kappa+\gamma+2\gamma_{\mathrm{dp}}}{2} & 0 & -ig^* \\ -ig & 0 & -i\Delta - \frac{\kappa+\gamma+2\gamma_{\mathrm{dp}}}{2} & ig \\ 0 & -ig & ig^* & -\gamma \end{pmatrix} \begin{pmatrix} \rho_{22} \\ \rho_{23} \\ \rho_{32} \\ \rho_{33} \end{pmatrix} \tag{2.20}$$

This can be written in the more compact form $\dot{\rho}_{\mathrm{v}}(t) = \mathbf{M}\rho_{\mathrm{v}}(t)$. In the absence of any light-matter coupling both the cavity field (ρ_{22}) and the QD (ρ_{33}) populations decay exponentially with the rates κ and γ, respectively, while the pure dephasing rate only gives rise to a decay of the polarization (ρ_{23}), i.e. coherence. A general solution to Eq. (2.20) can be expressed as [53]

$$\rho_{\mathrm{v}}(t+\tau) = \mathrm{e}^{\mathbf{M}\tau}\rho_{\mathrm{v}}(t) = U(\tau)\rho_{\mathrm{v}}(t) \quad . \tag{2.21}$$

Under non-resonant excitation of a QD, the exciton created above the bandgap will fall down to the s-shell on a typical timescale of ~ 10 ps, while the decay mechanism of the QD is typically on a much slower timescale $0.1 - 1$ ns. The QD can thus be assumed to be in the excited state at the initial time, meaning that $\rho_{33}(0) = 1$, $\rho_{22}(0) = 0$, and $\rho_{23}(0) = \rho_{32}(0) = 0$. Obtaining a general analytical solution of Eq. (2.20) is very complicated, but in the absence of detuning ($\Delta = 0$) and pure dephasing ($\gamma_{dp} = 0$) we can obtain the following solution

$$\begin{aligned} \rho_{33}(\tau) = U_{44}(\tau) = {} & \frac{(\kappa-\gamma)(\kappa-\gamma+\beta) - 8|g|^2}{2\beta^2}\mathrm{e}^{-\frac{1}{2}(\kappa+\gamma-\beta)\tau} \\ & + \frac{(\kappa-\gamma)(\kappa-\gamma-\beta) - 8|g|^2}{2\beta^2}\mathrm{e}^{-\frac{1}{2}(\kappa+\gamma+\beta)\tau} \\ & - 8\frac{|g|^2}{\beta^2}\mathrm{e}^{-\frac{1}{2}(\kappa+\gamma)\tau} \quad , \end{aligned} \tag{2.22}$$

where $\beta = \sqrt{(\kappa-\gamma)^2 - 16|g|^2}$. The size of g relative to the dissipative rates κ and γ thus determines whether or not the exponent is real or complex and

we will now discuss these two distinct regimes. Worth noting, however, is that the solution always contains three terms due to the three quantities, ρ_{22}, ρ_{33}, and $\rho_{23} = \rho_{32}^*$.

Weak coupling

From Eq. (2.22) we see that the QD decays irreversibly if $4|g| < |\kappa - \gamma|$, meaning that the coupling strength is smaller than the dissipative terms. While obtaining an analytical solution of Eq. (2.20) is very complicated, we can adiabatically eliminate the polarization terms by setting $\dot{\rho}_{23} = 0$, and we get the following expression

$$\rho_{23} = \frac{ig^*}{i\Delta - \gamma_{\text{tot}}}(\rho_{33} - \rho_{22}) \quad , \tag{2.23}$$

where $\gamma_{\text{tot}} = (\kappa + \gamma + 2\gamma_{\text{dp}})/2$. We note that in photonic-crystal cavities the cavity rate is often much larger than the two others, $\kappa \gg \{\gamma, \gamma_{dp}\}$. Inserting this into Eq. (2.20) and solving for ρ_{33}, shows that the QD decays exponentially with a decay rate given by

$$\Gamma = \gamma + 2|g|^2 \frac{\gamma_{\text{tot}}}{\gamma_{\text{tot}}^2 + \Delta^2} \tag{2.24}$$

The decay rate is enhanced following a lorentzian shape, where the width is determined approximately by the cavity rate. The enhancement of the decay rate is known as Purcell enhancement [54], and the Purcell factor is defined as the QD decay rate relative to that of a homogenous environment. On resonance this gives

$$F_{\text{P}} = \frac{\Gamma}{\Gamma_{\text{hom}}} = \frac{\gamma}{\Gamma_{\text{hom}}} + \frac{3}{4\pi^2}\frac{Q}{V}\left(\frac{\lambda}{n}\right)^3 \frac{|\mathbf{d}_{\text{eg}} \cdot \mathbf{f}(\mathbf{r_0})|^2}{|\mathbf{d}_{\text{eg}}|^2} \quad , \tag{2.25}$$

where we have assumed $\kappa \gg \{\gamma, \gamma_{dp}\}$, inserted the definitions of the coupling strength and κ, and used Eq. (2.12) from section 2.1.2. The first term in Eq. (2.25) is the decay of the QD in the absence of any cavity relative to the decay rate in a homogenous medium. In a photonic-crystal cavity γ is strongly inhibited by the surrounding structure [55], while the inhibition is not nearly as strong in micropillar cavities [56]. However, in either cavity this term is much smaller than the second term that is due to the cavity. The importance of a high Q-factor and low mode volume is evident from this equation, but also

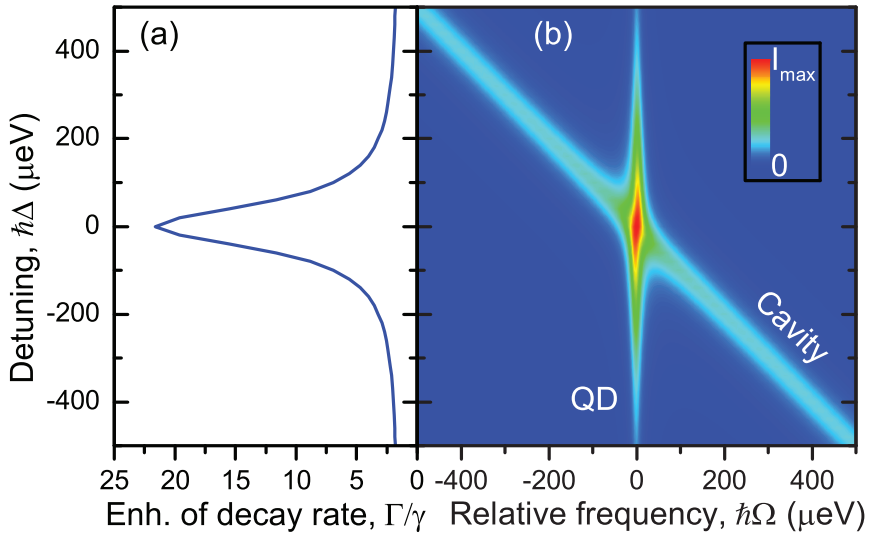

Figure 2.6: **a)** Enhancement of the decay rate as a function of detuning in the weak coupling, where $\hbar\kappa = 100$ μeV, $\hbar\gamma = 1$ μeV, $\hbar\gamma_{\mathrm{dp}} = 10$ μeV, and $|g| = \kappa/5$. **b)** Cavity emission spectra as a function of detuning calculated using Eq. (2.37). A small inhomogenous contribution is added to the cavity peak in order to make it visible. The intensity of the spectra increases on resonance and the crossing of the two peaks is the tell-tale of weak coupling.

the position of the QD dipole relative to the cavity field and alignment of the transition dipole moment with the field polarization are clearly important. In Fig. 2.6(a) the decay rate of the QD is plotted as a function of detuning, and we see how the enhancement predominately is given by the linewidth of the cavity. Finally we note that the method of adiabatic elimination corresponds to making the Markovian Wigner-Weisskopf approximation and only holds when the system is well inside the weak coupling regime, $4|g| \ll |\kappa - \gamma|$. For larger values of g, β remains a real number and the QD does decay irreversibly, but the backaction from the cavity field onto the QD will result in non-Markovian dynamics, which we will present the experimental proof of in chapter 3. The corresponding emission spectra are shown in Fig. 2.6(b), where a crossing between the cavity and QD peak is seen, and the intensity increases significantly

when on resonance.

Strong coupling

In the case where β is imaginary it is instructive to write Eq. (2.22) as

$$\rho_{33}(\tau) = \frac{\mathrm{e}^{-\frac{1}{2}(\kappa+\gamma)\tau}}{2\beta^2}\left[\left(\beta^2+\kappa-\gamma\right)\cos(\Omega\tau) + i2(\kappa-\gamma)\beta\sin(\Omega\tau) - 16|g|^2\right] \quad , \tag{2.26}$$

from which it is clear that the population of the QD oscillates with the frequency $\Omega = 2|g|\sqrt{1-\left(\frac{\kappa-\gamma}{4|g|}\right)^2}$, and the oscillations are damped exponentially with the rate $(\kappa+\gamma)/2$. This means that the excitation coherently oscillates back and forth between the QD and the cavity field, meaning that they are entangled until the excitation eventually leaks out predominately by cavity losses. The oscillations of the QD population are known as Rabi oscillations [57] and in Fig. 2.7(a) the decay is plotted for a few different detunings. In Fig. 2.7(b) the corresponding spectra are plotted as a function of detuning, and an avoided crossing between the QD and cavity field peaks is observed. This splitting occurs because the QD and cavity are entangled, and it is not possible to distinguish between them close to resonance.

2.4.2 Emission spectra

We now turn to calculating the emission spectrum from the coupled system, because this quantity can be measured experimentally and has frequently been used to characterize QD-cavity systems [58]. The Wiener-Khinchin theorem states that the spectrum is given by [59, 38]

$$S(\omega) = \frac{1}{2\pi}\lim_{T\to\infty}\int_0^T dt\int_0^T dt'\langle\hat{E}^{(-)}(t)\hat{E}^{(+)}(t')\rangle\mathrm{e}^{-i\omega(t-t')} \quad . \tag{2.27}$$

In the case of stationary conditions this can be simplified greatly as only the time difference will be of importance, but such conditions do not in general apply in QD-cavity systems. However, the spectrum can be written [60]

$$S(\Omega) = \frac{2}{\pi}Re\left[\int_0^\infty d\tau\mathrm{e}^{i\Omega\tau}\int_0^\infty dt\langle\hat{E}^{(-)}(t+\tau)\hat{E}^{(+)}(t)\rangle\right] \quad , \tag{2.28}$$

where $\Omega \equiv \omega - \omega_{\mathrm{qd}}$ is the relative observation frequency, and $\hat{E}^{(\pm)}(t)$ are the positive and negative frequency parts of the electric field operator. The electric

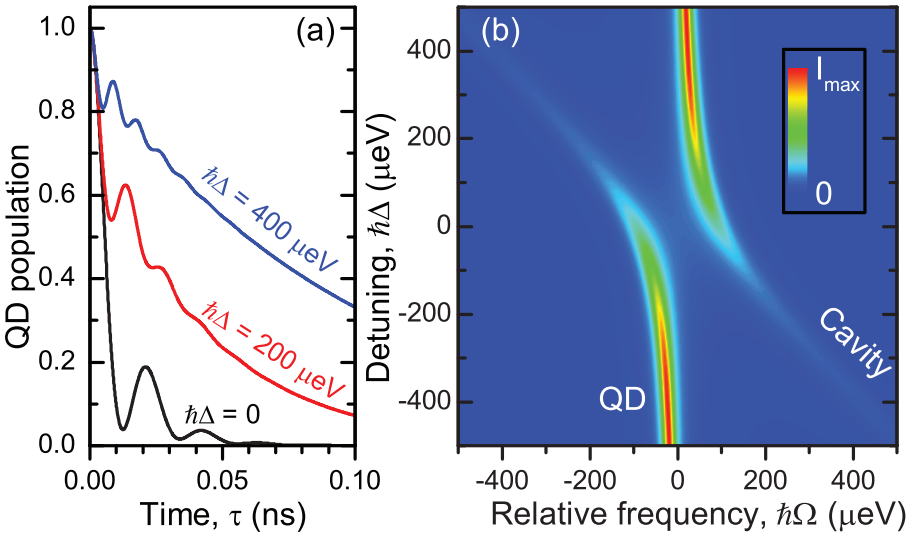

Figure 2.7: **a)** Three representative decay curves of the QD at different detunings showing damped Rabi oscillations for the parameters $\hbar\kappa = 100$ μeV, $\hbar\gamma = 1$ μeV, $\hbar\gamma_{\mathrm{dp}} = 10$ μeV, $|g| = \kappa$. **b)** Cavity emission spectra as a function of detuning showing Rabi splitting close to resonance as expected from the dynamics. The avoided crossing of the two peaks is considered the tell-tale of strong coupling.

field that can be measured in a spectrometer will in general contain emission from both the cavity and QD, which means that we can express the electric field operator as [49]

$$\hat{E}^{(+)}(t) = \eta_{\mathrm{ca}}\sqrt{\kappa}\hat{a}(t) + \eta_{\mathrm{qd}}\sqrt{\gamma}\hat{\sigma}_{-}(t) \quad , \tag{2.29}$$

where any time retardation between the two operators have been neglected, which is usually a good approximation in nanophotonic cavities. The coefficients η_{ca} and η_{qd} are complex coefficients that describe the collection efficiencies of the cavity and QD electric field, respectively, and their relative phase.

Combining Eq. (2.29) and (2.28) allows to express the full spectrum as

$$S(\Omega) = \frac{2}{\pi} Re \int_0^\infty d\tau \mathrm{e}^{i\Omega\tau} \int_0^\infty dt \left[|\eta_{\mathrm{ca}}|^2 \kappa s_{\mathrm{ca}} + |\eta_{\mathrm{qd}}|^2 \gamma s_{\mathrm{qd}} + \eta_{\mathrm{ca}} \eta_{\mathrm{qd}}^* \sqrt{\kappa\gamma} s_{\mathrm{dc}} + \eta_{\mathrm{ca}}^* \eta_{\mathrm{qd}} \sqrt{\kappa\gamma} s_{\mathrm{cd}} \right] \quad , \tag{2.30}$$

where

$$\begin{aligned} s_{\mathrm{ca}}(t', \tau) &= \langle \hat{a}^\dagger(t' + \tau) \hat{a}(t') \rangle \quad , \\ s_{\mathrm{qd}}(t', \tau) &= \langle \hat{\sigma}_+(t' + \tau) \hat{\sigma}_-(t') \rangle \quad , \\ s_{\mathrm{cd}}(t', \tau) &= \langle \hat{a}^\dagger(t' + \tau) \hat{\sigma}_-(t') \rangle \quad , \\ s_{\mathrm{dc}}(t', \tau) &= \langle \hat{\sigma}_+(t' + \tau) \hat{a}(t') \rangle \quad . \end{aligned}$$

In order to calculate the two-time expectation values above, we employ the quantum regression theorem in differential form, which states that given a set of operators $\hat{A}_\mathrm{j}$, whose expectation values satisfy a closed set of linear differential equations

$$\partial_\tau \langle \hat{A}_\mathrm{j}(t + \tau) \rangle = \sum_\mathrm{k} L_{\mathrm{j,k}} \langle \hat{A}_\mathrm{k}(t + \tau) \rangle \quad ,$$

then the two-time averages the operator $\hat{A}_\mathrm{j}$ with any other operator $\hat{B}$ also satisfy the same differential equation [61]

$$\partial_\tau \langle \hat{A}_\mathrm{j}(t + \tau) \hat{B}(t) \rangle = \sum_\mathrm{k} L_{\mathrm{j,k}} \langle \hat{A}_\mathrm{k}(t + \tau) \hat{B}(t) \rangle$$

This means that the equation governing the evolution of $s_{\mathrm{ca}}(t', \tau)$ is the same as the equation governing $\langle \hat{a}^\dagger(\tau) \rangle = Tr(\rho(\tau)\hat{a}^\dagger) = \rho_{42}(\tau)$. The equation containing the cavity spectrum, s_{ca}, can thus be written

$$\frac{d}{d\tau} \begin{pmatrix} s_{\mathrm{ca}} \\ s_{\mathrm{dc}} \end{pmatrix} = \mathbf{W} \begin{pmatrix} s_{\mathrm{ca}} \\ s_{\mathrm{dc}} \end{pmatrix} \quad , \quad \mathbf{W} = \begin{pmatrix} -\frac{\kappa}{2} & ig \\ ig^* & i\Delta - \frac{\gamma + \gamma_{\mathrm{dp}}}{2} \end{pmatrix} \quad , \tag{2.31}$$

which has been extracted from the master equation (2.19). The general solution to this equation can be written in the form

$$s_{\mathrm{ca}}(t', \tau) = K_1(t') \mathrm{e}^{\lambda_+ \tau} v_{+,1} + K_2(t') \mathrm{e}^{\lambda_- \tau} v_{-,1} \quad , \tag{2.32}$$

$$s_{\mathrm{dc}}(t', \tau) = K_1(t') \mathrm{e}^{\lambda_+ \tau} v_{+,2} + K_2(t') \mathrm{e}^{\lambda_- \tau} v_{-,2} \quad , \tag{2.33}$$

where $v_{+,1}$ is the first element of the eigenvector v_+ and $\lambda_\pm$ are the corresponding eigenvalues given by:

$$v_\pm = \begin{pmatrix} \frac{i}{g^*}\left(i\Delta - \frac{\gamma+\gamma_{\rm dp}}{2} - \lambda_\pm\right) \\ 1 \end{pmatrix} \quad , \quad \lambda_\pm = \frac{1}{4}\left(-\gamma - \gamma_{\rm dp} - \kappa + i2\Delta \pm \sqrt{\alpha}\right) \quad ,$$
$$\alpha = (\kappa + \gamma + \gamma_{\rm dp} - 2i\Delta)^2 + 4i\kappa(2\Delta + i\gamma + i\gamma_{\rm dp}) - 16|g|^2 \quad . \tag{2.34}$$

$K_1(t')$ and $K_2(t')$ are constants with respect to τ, and by evaluating $s_{\rm ca}(t',\tau)$ and $s_{\rm ca}(t',\tau)$ at time $\tau = 0$ we find them to be given by

$$K_1(t') = \frac{1}{v_{-,1} - v_{+,1}}(v_{-,1}\rho_{23}(t') - \rho_{22}(t')) \quad , \tag{2.35}$$

$$K_2(t') = \frac{1}{v_{-,1} - v_{+,1}}(\rho_{22}(t') - v_{+,1}\rho_{23}(t')) \quad . \tag{2.36}$$

Combining these expression and inserting them back into Eq. (2.30) gives us the following expression for the cavity spectrum

$$S_{\rm ca} = -\frac{2|\eta_{\rm ca}|^2\kappa}{\pi} Re\left[\frac{v_{+,1}}{i\Omega + \lambda_+}\int_0^\infty dt' K_1(t') + \frac{v_{-,1}}{i\Omega + \lambda_-}\int_0^\infty dt' K_2(t')\right] \quad , \tag{2.37}$$

and for the cross-term

$$S_{\rm dc} = -\frac{2\eta_{\rm ca}\eta_{\rm qd}^*\sqrt{\kappa\gamma}}{\pi} Re\left[\frac{1}{i\Omega + \lambda_+}\int_0^\infty dt' K_1(t') + \frac{1}{i\Omega + \lambda_-}\int_0^\infty dt' K_2(t')\right] \quad . \tag{2.38}$$

While we have derived the pole structure of the cavity spectrum, we note that a fully analytical solution requires an analytical solution of Eq. (2.20), which is very complicated and for that reason the spectrum needs to be calculated numerically. In Fig. 2.6(b) the cavity spectrum is calculated as a function of detuning in the weak coupling regime, where the anticipated crossing of the cavity and QD peaks is observed. The cavity spectrum is very weak compared to the QD spectrum for far-detuned conditions, and in this figure a small inhomogeneous contribution has been added at the cavity frequency in order to make the cavity visible. Close to resonance the cavity spectrum becomes dominant because most of the QD emission couples out through the cavity as evident from the Purcell enhancement. In Fig. 2.7(b) the same calculation is done in the strong coupling regime, and we have not added any inhomogeneous

contribution. We observe an avoided crossing, and the Rabi splitting between two identical peaks is observed in perfect correspondence with the dynamical properties. We note that the effect of dephasing is twofold. It broadens the QD linewidth and it gives rise to a larger intensity in the cavity peak. In both figures, although most clear for strong coupling, the QD peak is shifted slightly in frequency even for large detunings. This energy shift can be considered the cavity-assisted Lamb shift, where the modification of the LDOS gives rise a frequency shift of the QD. It occurs because part of the emission is now at the larger or smaller cavity frequency and in order to preserve the total energy, the QD peak shifts slightly in the opposite direction, which we will show experimentally in the next chapter.

Calculating the QD spectrum and the remaining cross-term is now easy, because they also satisfy Eq. (2.31) and their solutions are thus also given by Eq. (2.33), with the only difference that $K_1(t')$ and $K_2(t')$ are now called $L_1(t')$ and $L_2(t')$ and are given by

$$L_1(t') = \frac{1}{v_{-,1} - v_{+,1}}(v_{-,1}\rho_{33}(t') - \rho_{32}(t')) \ , \tag{2.39}$$

$$L_2(t') = \frac{1}{v_{-,1} - v_{+,1}}(\rho_{32}(t') - v_{+,1}\rho_{33}(t')) \ . \tag{2.40}$$

Again we can combine the equations and insert them into Eq. (2.30) to obtain the following expressions for the QD spectrum and the remaining cross-term:

$$\begin{aligned} S_{\mathrm{qd}} &= -\frac{2|\eta_{\mathrm{qd}}|^2\gamma}{\pi} Re\left[\frac{1}{i\Omega + \lambda_+}\int_0^\infty dt' L_1(t') + \frac{1}{i\Omega + \lambda_-}\int_0^\infty dt' L_2(t')\right] \ , \\ S_{\mathrm{cd}} &= -\frac{2\eta_{\mathrm{ca}}^*\eta_{\mathrm{qd}}\sqrt{\kappa\gamma}}{\pi} Re\left[\frac{v_{+,1}}{i\Omega + \lambda_+}\int_0^\infty dt' L_1(t') + \frac{v_{-,1}}{i\Omega + \lambda_-}\int_0^\infty dt' L_2(t')\right] \ . \end{aligned} \tag{2.41}$$

Using the above equations we now plot the cavity and QD spectra in Fig. 2.8(a) for a detuned system in the weak coupling regime. We have set $|\eta_{\mathrm{ca}}|^2 = |\eta_{\mathrm{qd}}|^2 = 1/2$, and we notice that while both have peaks at the QD frequency only the cavity spectrum has a peak at the cavity frequency. As detuning increases the total intensity in the cavity spectrum drops and the QD spectrum dominates, while the cavity spectrum dominates on resonance. In Fig. 2.8(b) the total spectrum from Eq. (2.30) is plotted, where we have introduced the relative phase ϕ as $\eta_{\mathrm{ca}}^*\eta_{\mathrm{qd}} = \mathrm{e}^{i\phi}|\eta_{\mathrm{ca}}| \cdot |\eta_{\mathrm{qd}}|$. Changing the relative

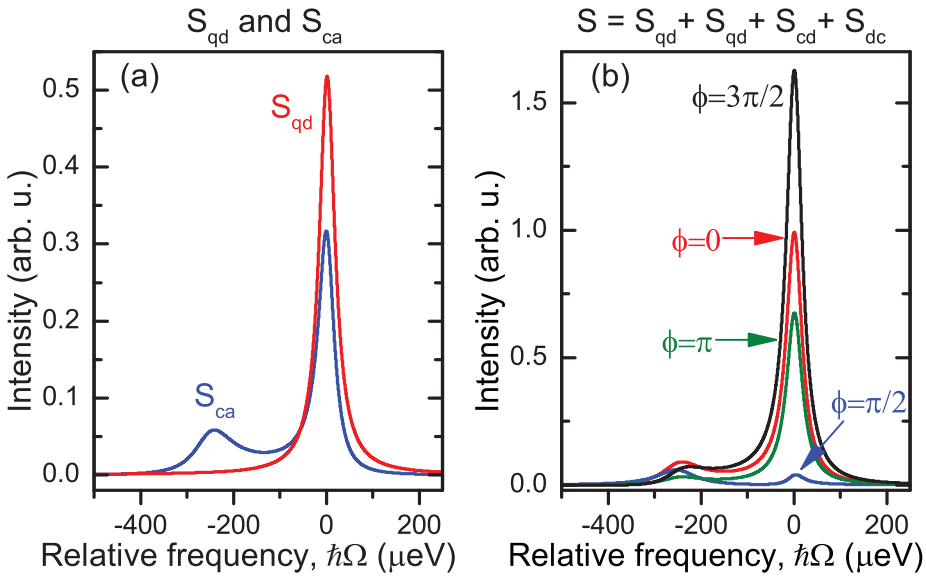

Figure 2.8: A detuned system in the weak coupling regime with parameters $\hbar\Delta = 250$ μeV, $\hbar\kappa = 100$ μeV, $\hbar\gamma = 1$ μeV, $\hbar\gamma_{\mathrm{dp}} = 20$ μeV, and $|g| = \kappa/5$. **a)** Both the QD and cavity spectra have peaks at the QD frequency, while only the cavity spectrum has a peak at the cavity frequency. **b)** The total emission spectra containing both QD, cavity and interference terms with $|\eta_{\mathrm{ca}}|^2 = |\eta_{\mathrm{qd}}|^2 = 1/2$ and $\eta^*_{\mathrm{ca}}\eta_{\mathrm{qd}} = \mathrm{e}^{i\phi}|\eta_{\mathrm{ca}}| \cdot |\eta_{\mathrm{qd}}|$. Changing the relative phase can drastically alter the total emission spectrum.

phase not only changes the total intensity by an order of magnitude but also the qualitative shape of spectrum, with the cavity peak being negligible for $\phi = 3\pi/4$ but dominating for $\phi = \pi/2$. The relative phase can easily change experimentally when detuning is changed or depending on alignment, and much care thus needs to be taken when comparing experimentally measured spectra with theory as we will discuss more in the following chapter.

As noted, all the spectra have the same pole structure and from Eq. (2.37) we can find the approximate Rabi splitting between the two peaks on resonance

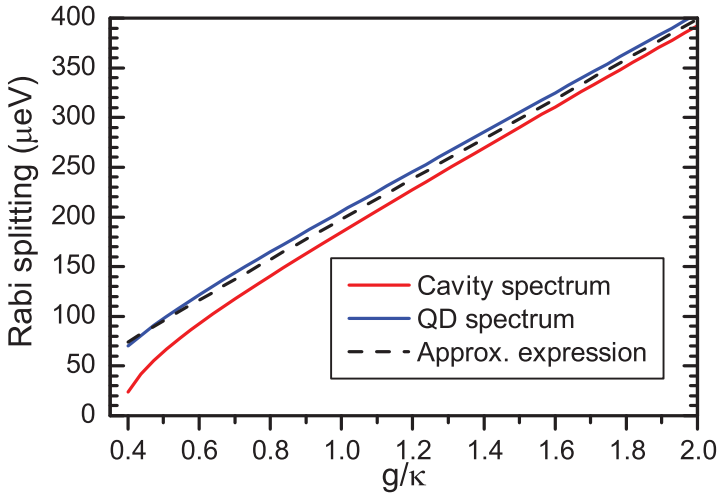

Figure 2.9: The Rabi splitting on resonance is plotted as a function of the coupling strength for the parameters $\hbar\kappa = 10\hbar\gamma_{\mathrm{dp}} = 100\hbar\gamma = 100$ μeV. By numerical investigation, the rabi splitting is extracted from the cavity and QD spectrum, and we compare them to the Rabi splitting obtained from the approximate expression in Eq. (2.42). We find a good agreement with the Rabi splitting extracted from the QD spectrum, while the Rabi splitting extracted from the cavity spectrum shows a large deviation.

to be

$$\Delta\Omega \simeq \sqrt{4|g|^2 - \left(\frac{\kappa - \gamma - \gamma_{\mathrm{dp}}}{2}\right)^2} \tag{2.42}$$

However, it is noted that this is only an approximate expression since the pole structure actually gives rise to four peaks, that also depend on the numerators. This also leaves room for the Rabi splitting to vary between the cavity and QD spectrum, which numerical investigation reveals is the case. In Fig. 2.9 the Rabi splitting extracted from both the cavity and QD spectrum is shown together with the value obtained from the approximate expression in Eq. (2.42). While the Rabi splitting extracted from the QD spectrum agrees well with the approximate expression, the Rabi splitting extracted from the cavity spectrum shows large deviations at small coupling strengths. Varying the collection ef-

ficiencies of the QD spectrum relative to the cavity spectrum can thus alter the total spectrum significantly without changing any other parameters. This emphasizes that care must be taken when extracting quantitative information from the emission spectra. Furthermore, we note that the Rabi splitting extracted from cavity spectrum is significantly smaller than the expected value at smaller coupling strengths, and if mainly the cavity spectrum is detected experimentally, this would lead to a significant underestimate of the coupling strength.

2.4.3 Second order coherence

The last measurable quantity that we will discuss is the second order coherence of the emitted electric field, which reveals information on the statistics of the emitted field. Fock states, or number states, constitute the basis for the quantum theory of light, and they are characterized by having no uncertainty in the photon number n, i.e. $(\Delta n)^2 = 0$, which makes it easy to evaluate the second order coherence function as [38]

$$g^{(2)}(\tau = 0) = 1 - \frac{1}{n} \quad \text{for} \quad n \geq 1. \tag{2.43}$$

Single photon emission thus has a vanishing $g^{(2)}(0)$, and this provides a crucial experimental check of single photon emission. Moreover, this quantity is experimentally accessible by directing the emission onto a $50:50$ beamsplitter and recording the coincidence counts on the detectors with the time delay τ.

We now consider two experimentally distinct cases, where the QD-cavity system is excited either pulsed or continuously. Under pulsed conditions it is trivial that $g^{(2)}(0) = 0$ since only a single excitation is present in the system. Under continuous excitation the situation becomes slightly more complicated, but if we consider the QD-cavity system well inside the weak coupling regime, where the adiabatic approximation applies, we obtain the expression [38]

$$g^{(2)}(\tau) = 1 - \mathrm{e}^{-\Gamma\tau} \quad , \tag{2.44}$$

where Γ is given by Eq. (2.24). For details on how this function is calculated we refer to chapter 6, where the same method is used but for the different situation of a resonantly driven QD.

2.4.4 Relation to the local density of states

In the above calculations the density matrix is used to describe the state of the system, but the calculations can also be done using the LDOS description from section 2.1.2. In the following we will show that the two approaches are equivalent up to the point where pure dephasing is introduced. We start by noting that the local density of states can be expressed in the following way [62]

$$\rho(\omega, \mathbf{r_0}, \hat{\mathbf{e}}_{\mathrm{qd}}) = \frac{2\omega}{\pi c^2} \mathrm{Im}\{\hat{\mathbf{e}}_{\mathrm{qd}} \cdot \mathbf{G}(\omega, \mathbf{r}_0, \mathbf{r}_0) \cdot \hat{\mathbf{e}}_{\mathrm{qd}}\} \ , \tag{2.45}$$

where $\mathbf{G}(\omega, \mathbf{r}_0, \mathbf{r}_0)$ is the Green's tensor for the electromagnetic field. The imaginary part of the Green's tensor only has a transverse part, which can be written [63]

$$\mathbf{G}^T(\omega, \mathbf{r}, \mathbf{r}') = \frac{c^2}{n^2 V} \sum_{\mu} \frac{\mathbf{f}_\mu(\mathbf{r}) \mathbf{f}_\mu^*(\mathbf{r}')}{2\tilde{\omega}_\mu(\tilde{\omega}_\mu - \omega)} \ , \tag{2.46}$$

where $\tilde{\omega}_\mu = \omega_{\mathrm{ca}} - i\kappa/2$ and it has been assumed that one cavity mode dominates the expansion of the Green's tensor. The LDOS for an emitter can thus be expressed

$$\rho(\omega, \mathbf{r_0}, \hat{\mathbf{e}}_{\mathrm{qd}}) = \rho_{\mathrm{bg}}(\omega, \mathbf{r_0}, \hat{\mathbf{e}}_{\mathrm{qd}}) + \rho_{\mathrm{ca}}(\omega, \mathbf{r_0}, \hat{\mathbf{e}}_{\mathrm{qd}}) \quad \text{, where} \tag{2.47}$$

$$\rho_{\mathrm{bg}}(\omega, \mathbf{r_0}, \hat{\mathbf{e}}_{\mathrm{qd}}) = \frac{\hbar\epsilon_0}{\pi} \frac{1}{\omega |\mathbf{d}_{\mathrm{eg}}|^2} \gamma \qquad \text{and} \tag{2.48}$$

$$\rho_{\mathrm{ca}}(\omega, \mathbf{r_0}, \hat{\mathbf{e}}_{\mathrm{qd}}) = \frac{1}{\pi n^2 V} |\mathbf{f}(\mathbf{r_0})|^2 |\hat{\mathbf{e}}_{\mathrm{qd}} \cdot \hat{\mathbf{e}}_{\mathrm{ca}}|^2 \frac{\kappa/2}{(\omega - \omega_{\mathrm{ca}})^2 + (\kappa/2)^2} \quad . \tag{2.49}$$

The first term in Eq. (2.47) gives the LDOS in the absence of the cavity. This term depends on the inhibition of spontaneous emission in the photonic crystal, but for the comparison to the Jaynes-Cummings model it has been constructed so that it gives rise to a frequency-independent decay rate. The second term is the LDOS originating from the cavity that has been found by substituting Eq. (2.46) into Eq. (2.45) and assuming that the QD-cavity detuning is much smaller than the frequency of the cavity. Inserting this LDOS into Eq. (2.10) gives the following expression

$$\frac{d}{dt} c_{\mathrm{e}}(t) = -\frac{\gamma}{2} c_{\mathrm{e}}(t) - |g|^2 \int_0^t c_{\mathrm{e}}(t') \mathrm{e}^{(-\kappa/2 + i\Delta)(t - t')} dt' \tag{2.50}$$

This equation can be solved by performing a Laplace transformation, isolating the coefficient c_{e}, and transforming back to time domain, thereby obtaining

an analytical expression for $c_e(t)$. The population of the QD is now easily computed as $|c_e(t)|^2$ and the expression is found to be equal to Eq. (2.22), which was found using the density matrix description.

Within this framework we can also calculate the dynamics of the cavity, the emission spectrum, etc. [64] just like in the density matrix description. The above derivation was done by considering a pure state, and pure dephasing, which is a classical probability, was not included. Pure dephasing can be included in the above calculations but it requires quantum Monte Carlo simulations. The density matrix allows for the inclusion of classical probabilities and pure dephasing is easily included through the Lindblad terms that automatically preserve the properties of the density matrix, and for this reason the main derivation in this chapter has been done using that description.

Chapter 3

Quantitative analysis of quantum dots in cavity quantum electrodynamics

Cavity quantum electrodynamics (CQED) provides a way of enhancing and controlling the light-matter interaction between a single emitter and a cavity field. It has potential applications in the field of quantum information processing [65] as a few-photon nonlinearity [66], and as a controlled-NOT gate, where the state of a solid-state quantum bit conditionally controlled by the state of a photonic quantum bit [67] has already been demonstrated. The field was pioneered by a number of founding experiments on single atoms [1], but scaling of these systems to larger networks remains a major challenge. Solid-state implementations with quantum dots embedded in nanophotonic structures are a promising platform that, although in its infancy, could potentially solve the problem of scalability and lead to quantum-information processing on an optical chip [68].

In this chapter we present a comprehensive study of the dynamical and spectral properties of CQED systems including a quantitative comparison to theory. Experiments are performed on single QDs embedded either in a micropillar cavity or in a photonic-crystal cavity. It is demonstrated that while the dynamics of single QDs tuned through the resonances of both micropil-

lar and photonic-crystal cavities are well described by theory, this is not the case for the spectral measurements. We attribute the discrepancy to the fact that the details of the out-coupling of photons from the cavity to the detector are not well known, and mutual interference between the different propagation paths can occur.

For a single QD tuned through resonance with the fundamental mode of a micropillar cavity we observe non-Markovian, i.e. memory dependent, effects in the dynamics. While the system is in the weak coupling regime, the light-matter coupling strength is sufficiently large for the cavity to exert backaction on the QD. As a result the QD decays irreversibly, but the non-Markovian coupling to the photon reservoir gives rise to a non-exponential decay.

For the photonic-crystal cavity we observe an anti-crossing in the measured spectra when tuning the cavity through the QD resonance, which suggests strong coupling between the QD and cavity. From the spectral Rabi splitting and from time-resolved measurements we determine the light-matter coupling strength, but the two obtained values differ by more than a factor of 4. The decay rate is found to be significantly slower than expected from the anti-crossing, which proves that the QD is in fact not in the strong coupling regime despite the expectations from spectral measurements. We attribute this difference to the feeding of the cavity by mainly multiexcitons but also other QDs that may give rise to a collective Rabi splitting.

The main part of the quantitative analysis of dynamics and emission spectra presented in this chapter is based on the work we have published in [69], while the observation of non-Markovian dynamics for a single QD in a micropillar cavity is based on the work we have published in [56].

3.1 Micropillar cavities

The first demonstration of a significant Purcell enhancement in a solid-state system, was done by measuring the enhanced decay of an ensemble of QDs embedded in a micropillar cavity [70]. Shortly after, single-photon emission was demonstrated [17, 71] and finally the generation of indistinguishable photons from a QD embedded in a micropillar was demonstrated [72]. Since then, experimental proof of strong coupling in a micropillar cavity and in a photonic-crystal cavity was published simultaneously [73, 74]. The geometry of micropillars

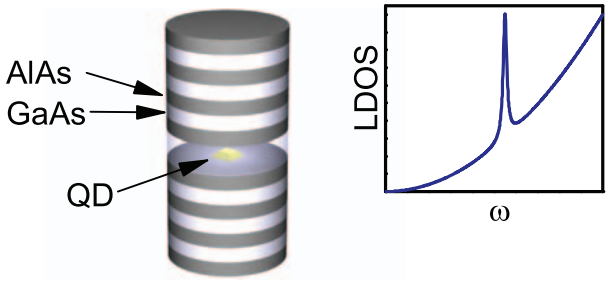

Figure 3.1: Sketch of a micropillar cavity with a single QD embedded and the corresponding LDOS.

makes it possible to excite the sample orthogonally to the primary emission direction, which has allowed for resonant excitation of a single QD showing Mollow triplets [75] due to the dressing of the QD two-level system by the excitation laser [76].

3.1.1 Optical properties

The micropillar investigated has a height of ~ 9 µm and a diameter of 1.7 µm and consists of alternating GaAs and AlAs layers surrounding a central GaAs cavity with a layer of low density InAs QDs ($60-90$ µm^{-2}) embedded, cf. the sketch in Fig. 3.1. The alternating layers have a thickness of $(\lambda/n)/4$ and form a 1D photonic crystal, and the central cavity with thickness λ/n permits a cavity mode in analogy to the L3 photonic-crystal cavity. There are 30 periods of alternating layers beneath the cavity and only 26 above the cavity in order to make the cavity leak primarily in the upward direction, where it can be collected efficiently. Because the micropillar consists of the same material as the photonic-crystal membrane, the same fabrication method that was outlined in section 2.2 can be used. However, because the total number of layers exceed 110 and because the pillar has a height of ~ 9 µm, great care has to be taken during the growth to ensures that the layers are flat and during the etch to ensure that the outside of the pillar is smooth since this might otherwise degrade the Q-factor. The micropillar sample investigated in this work is fabricated by our collaborators at the University of Würzburg and more details on the

fabrications process can be found in [77]. While the QDs are randomly positioned inside the cavity, they are by design always placed at the antinode of the cavity field, thereby ensuring an effective coupling to the cavity mode. While the layers above and below the central cavity region work as Bragg mirrors, the QD can still couple to radiation modes that leak out perpendicularly to the micropillar. The symmetry of the pillar implies that radiation modes always have an incidence angle close to zero and there is no total internal reflection taking place, that would otherwise help limit the effect of radiation modes. The transition from high to low refractive index does, however, still give rise to some reflections. Very high Q-factors of ~ 50000 can be reached [78], but in general the mode volume is $\sim 10\ (\lambda/n)^3$ [79], which is an order of magnitude larger than in L3 photonic-crystal cavities.

Because the background decay rate, i.e. the decay rate when far detuned from the cavity mode, is not significantly altered, the LDOS for a QD embedded in a micropillar cavity can be sketched as shown in Fig 3.1. The small size of the central GaAs cavity results in discrete optical modes, and so far we've only been refering to the high-Q fundamental mode of the cavity. In general it is possible to identify at least 4 modes, where the 3 higher-order modes typically lie closely spaced within a small range (~ 3 nm) situated at around ~ 10 nm shorter wavelengths than the fundamental mode.

3.1.2 Experimental setup

If the thermal energy is too large, the shallow confinement potential of the QDs cannot keep excitons confined and non-radiative recombination becomes large. Emission can therefore only be seen from the QDs if the temperature is below ~ 70 K, and in order to reduce the effects of dephasing from the environment we typically cool the sample to 10 K using liquid helium. The sample is attached to a copper sample holder using silver glue and is placed in a helium flow cryostat, Microstat HiRes II from Oxford Instruments, where liquid helium is pumped from a dewar into a cold finger, that is thermally anchored to the sample mount. Approximately 2 mm above the sample a window with diameter 25 mm and thickness 1.5 mm is placed which allows for the optical access in a large solid angle. Using a turbo pump the sample chamber is pumped down to $\sim 10^{-6}$ mbar. The cyostat is mounted on two translation stages, which enables

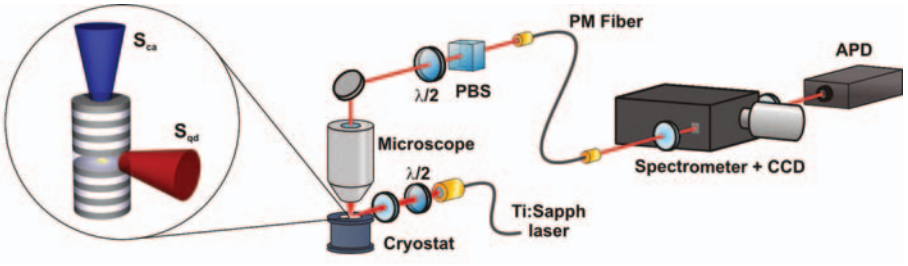

Figure 3.2: Experimental setup for spectral and time-resolved measurements using side-excitation of micropillar cavities. The zoom-in shows a sketch of the micropillar with the corresponding cavity and QD emission spectra.

positioning of the sample with a precision of 0.1 μm relative to the excitation optics [80].

For excitation of the sample we use a mode-locked Ti:Saphh laser, Mira 900 from Coherent, which is pumped by a 5 W laser at 532 nm, Verdi from Coherent. Wile the laser can always be operated in continuous wave (CW) mode, optics can be added or removed to switch between femto-second and pico-second mode. However, we only use pico-second mode where the pulse width is $\sim$ 3 ps, which is much shorter than the dynamics of the QD and excitation can thus be considered a delta pulse. The corresponding spectral width is $\sim$ 0.4 nm, which is narrow enough to efficiently excite higher levels of the QDs, e.g. p-shell excitation. Furthermore, the Ti:Sapph laser has a wide tuning range of $750 - 950$ nm, where purging with nitrogen is needed for mode-locked operation above 900 nm. For power control, the output of the laser is directed through two sets of half-wave-plates ($\lambda/2$) and polarizing beamsplitters (PBS) and if needed neutral density (ND) filters before coupling into a single-mode fiber.

The p-shell of the QD is typically $\sim$ 20 nm blue detuned from the emission, which means that the Bragg mirrors also reject most of the excitation laser when attempting to excite the micropillar from the top. Therefore, we excite the micropillar from the side, as shown in Fig. 3.2. The output of the single-mode fiber is collimated by a fiber-coupler and the output passes through a $\lambda/2$-plate for polarization control before it is directed onto a lens that focusses the light to a spot size of 8 μm with an incidence angle of 15° with respect to

the substrate. This side-excitation is particularly useful for both p-shell and s-shell excitation as it allows for easy separation of the excitation laser and emission.

The emission from the sample is collected by a microscope objective, CFI Super Plan Flour ELWD 40XC from Nikon, with a numerical aperture (NA) of 0.6. The window of the cryostat imposes a certain minimum working distance and it also gives rise to spherical abberations of the emission, and this objective was found to be the best solution as it has a long working distance of $2.8 - 3.6$ mm, a reasonably high NA, and the possibility to compensate for spherical abberations from the window. The spot size of the objective has been measured to be 2.4 µm [80] and the transmission is 77% in the range $800 - 950$ nm. The objective is mounted in a customized Olympus BXFM system, which is not shown in Fig. 3.2, and it allows for the distance between the microscope objective and the sample to be varied. It also makes it possible to remove the mirror that directs the emission to the $\lambda/2$-plate and PBS, and the emission can be sent to a CCD camera for imaging. At the same time a beam-splitter cube, that reflects $\sim 10\%$ and transmits $\sim 90\%$, can be inserted before the mirror, and it directs a white light source onto the sample while most of the light reflected from the sample is transmitted to the CCD for imaging.

After being collimated by the microscope objective, the emission from the sample is directed onto a $\lambda/2$-plate and PBS for polarization filtering before being coupled into a single-mode polarization-maintaining (PM) fiber. The PM fiber is situated at the image plane, and it provides the spatial filtering needed for experiments on single QDs. A gaussian beam can be coupled into the fiber with an efficiency up to $\sim 80\%$. For a dipole pattern half of the emission is in the direction opposite of detection, and maximally 51% of the radiation in the direction towards detection can be coupled into a single mode fiber [81]. However, the QD couples to the micropillar cavity mode, which results in a more complex radiation pattern.

Despite of the loss in the fiber coupling, it is still advantageous to use a fiber, since the output of the fiber remains independent of the alignment into the fiber. The output of the fiber is collimated and sent to a 0.5 m spectrometer, PI Acton 2-500i from Princeton Instruments, where a 1200 g/mm or 150 g/mm grating can be used, cf. Fig. 3.2. While the former has a high resolution down to ~ 0.025 nm it also suffers from lower transmission and only a small wavelength

region of ~ 40 nm can be viewed on the CCD. In contrast, the latter has a low resolution, but a larger transmission and wavelength region on the CCD. For spectral measurements the output of the spectrometer can be directed onto a CCD, which is peltier-cooled down to $-75°$ in order to reduce the noise. For lifetime-measurements, the output of the spectrometer is directed onto an avalanche photo diode (APD), PDM-50CT from Micro Photon Devices, that has a high time resolution of 50 ps and low dark counts of 75 counts/s but a low quantum efficiency of 5% at 900 nm. After each detection event the APD has a dead time of 70 ns, where no photons can be detected, and there is a 0.5% afterpulsing probability.

Before coupling the laser into the single mode fiber, a portion of the beam is picked out and sent to a fast triggering diode. Using a PicoHarp 300 from PicoQuant, the output of the triggering diode is correlated with the output from the APD with a resolution of 4 ps. If a single photon is detected by the APD, the PicoHarp electronics calculate the time-difference to the last pulse from the triggering diode and builds up a histogram with single-photon detection events versus arrival time. The setup also includes a Hanbury-Brown and Twiss (HBT) setup and a Hong-Ou-Mandel interferometer, but these will be explained in detail in chapter 5.

3.1.3 Observation of non-Markovian dynamics

In this section we present a systematic study of the dynamics of a single QD tuned through the resonance of the fundamental mode of a micropillar cavity. The system is shown to be in neither the weak nor strong coupling regime, but rather in an intermediate regime, where the QD decays irreversibly but non-Markovian, i.e. memory dependent, which are usually features attributed to the weak and strong coupling regime, respectively. Both the strong coupling and intermediate regime are manifestations of non-Markovian effects, because the QD-cavity coupling is so strong that there is "memory" in the system, meaning that the population at one instant of time depends on its value at previous times, which leads to light-matter entanglement. While the ability to enter the strong coupling regime has been demonstrated by recording detuning-dependent spectra [73], the results presented here constitute the first experimental demonstration of non-Markovian dynamics in solid-state cavity QED to our knowledge [56], thus complementing results on atomic systems [82].

The experimental signature of non-Markovian coupling between a two-level emitter and a radiation bath is the deviation of the spontaneous emission intensity from an exponential decay. This can realized by recasting Eq. (2.20) for the Jaynes-Cummings model to the integro-differential form

$$\begin{aligned}\dot{\rho}_{\mathrm{qd}}(t) &= -\gamma\rho_{\mathrm{qd}}(t) - |g|^2[G(t) + G^*(t)] \,, \\ \dot{\rho}_{\mathrm{ca}}(t) &= -\kappa\rho_{\mathrm{ca}}(t) + |g|^2[G(t) + G^*(t)] \,, \\ G(t) &= \int_0^t [\rho_{\mathrm{qd}}(t') - \rho_{\mathrm{ca}}(t')]\mathrm{e}^{-(\gamma_{\mathrm{tot}} - i\Delta)(t-t')}dt' \,,\end{aligned} \tag{3.1}$$

where $\gamma_{\mathrm{tot}} = (\kappa + \gamma + 2\gamma_{\mathrm{dp}})/2$. Here $G(t)$ is the memory kernel of the system and we can recognize the three distinct regimes: $|\gamma_{\mathrm{tot}} - i\Delta| \gg 2|g|$ is the weak coupling Markovian regime, where the Wigner-Weisskopf approximation holds and the QD decays exponentially. $2|g| \lesssim |\gamma_{\mathrm{tot}} - i\Delta|$ defines an intermediate non-Markovian regime, where the Wigner-Weisskopf approximation breaks down and the QD decays irreversibly but non-exponentially due to the back-action from the cavity. Finally, $2|g| > |\gamma_{\mathrm{tot}} - i\Delta|$ defines the strong coupling regime, where the excitation coherently oscillates back and forth between the QD and cavity due to the strong coherent back-action from the cavity. We will show that the particular system we are investigating is in the intermediate regime, which is revealed by performing time-resolved measurements.

Initially we search many cavities in order to find a QD coupled to a cavity mode and situated at a slightly higher energy, thereby allowing for the QD to be tuned through the cavity mode resonance by increasing the temperature. After finding such a QD-cavity system we tune the excitation laser to the p-shell of the QD, which results in a very clean spectrum, cf. Fig. 3.3(a). The Q-factor of the cavity is measured under strong above-band excitation power to ensure that all QDs are saturated [83], and we find $Q = 12200$ corresponding to $\hbar\kappa = 110\,\mu\mathrm{eV}$ by deconvoluting the spectrum with the instrument response function (IRF) of the spectrometer. The QD emission shifts to lower energies much faster than the cavity mode when increasing temperature, which allows for systematic variations of the detuning by controlling the temperature. In Fig. 3.3(b) the recorded decay curve and corresponding fit are displayed under far-detuned conditions ($\hbar\Delta = 362\ \mu\mathrm{eV}$) as well as the IRF of the setup, which is measured by propagating a laser pulse through the setup and adjusting the power to be similar to that of the emission. The decay curves are modeled by

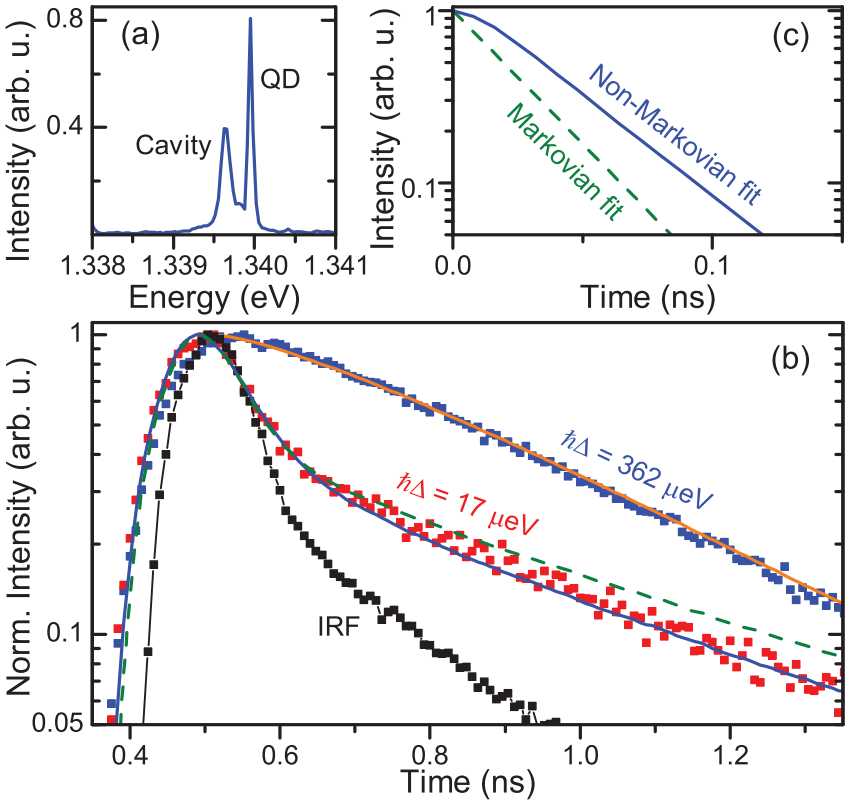

Figure 3.3: **a)** Emission spectrum at 10 K under p-shell excitation. **b)** Measured curves of the QD decay close to and far from resonance. For $\hbar\Delta = 362$ μeV the decay is Markovian and bi-exponential, and the fit is excellent. The data for $\hbar\Delta = 17$ μeV is modeled with the non-Markovian model obtained by solving Eq. (3.1) (solid blue curve) with an additional exponential decay accounting for the recombination of dark excitons. The green dashed curve represents the case, where the data is modeled with a Markovian bi-exponential decay and the same slow rate is used. A pronounced offset from the Markovian theory is observed. **c)** The fast part of the Markovian and non-Markovian fits to the decay curve at $\hbar\Delta = 17$ μeV without convolution with the IRF, which highlights the deviations from the Markovian theory.

convoluting a bi-exponential function including a background with the measured IRF. By blocking the laser a background file is recorded from which the dark counts are extracted. Afterpulsing also contributes to the background and this is calculated using the counts in the measured decay curve and added to the background. The offset between the IRF and measured decay curve is important for the convolution process, and by starting the fit much before the excitation, the reduced $\tilde{\chi}^2$ is calculated as a function of offset. Usually a clear minimum can be found, which gives the offset. Finally, the starting time for the fit is chosen to be at the maximum of the decay curve. With the background, offset, and start time as fixed parameters, the four parameters for the bi-exponential decay are now fitted to the decay curve. The normalized residuals are plotted for each time-bin and if the fit is good there should not be any systematic deviations. Similarly, $\tilde{\chi}^2$ is calculated for the fit and if $\tilde{\chi}^2 \simeq 1$ the agreement between the observed and expected distributions is satisfactory [84]. For verification we also fit single exponentials to the data, but $\tilde{\chi}^2$ is usually significantly higher, indicating that this is not the correct model. More details on the fitting routine can be found in [85, 80]. The far-detuned decay curve ($\hbar\Delta = 362$ μeV) in Fig. 3.3(b) is bi-exponential and as outlined in section 2.1.1 we extract the background radiative decay rate as $\gamma = \gamma_{\text{fast}} - \gamma_{\text{slow}} = 1.94\ \text{ns}^{-1}$ corresponding to $\hbar\gamma = 1.3$ μeV.

Close to resonance ($\hbar\Delta = 17$ μeV) the fast decay is modeled with the full solution obtained from Eq. (3.1), with the experimental values of Δ, κ, γ, and γ_{dp}. The slow part of the decay, that is due to the recombination of dark excitons, is still modeled with an exponential. Fig. 3.3(b) shows the comparison between experiment and theory (solid blue line) close to resonance, from which we extract $\hbar|g| = 22.6 \pm 0.9$ μeV. The system is in the intermediate coupling regime ($2|g| \lesssim |\gamma_{\text{tot}} - i\Delta|$) as verified by evaluating $\hbar|\gamma_{\text{tot}} - i\Delta| = 64.1$ μeV. Describing the data with the Markovian bi-exponential model is shown in Fig. 3.3(b) (dotted green line), where the same slow component has been used. Erroneously describing the data using this model leads to significant deviations between the theory and data that are visible in the raw data in Fig. 3.3(b). We stress, that the number of parameters used for both the Markovian and non-Markovian modeling are the same. In order to highlight the deviations from the Markovian theory, we plot the fast part of the Markovian and non-Markovian fits to the decay curve at $\hbar\Delta = 17$ μeV without the convolution with the IRF in

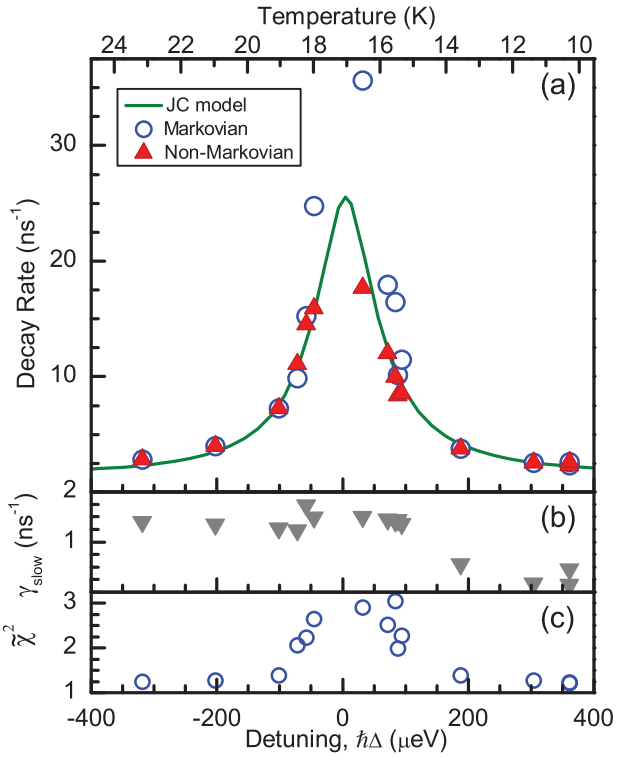

Figure 3.4: **a)** Detuning-dependent decay rates of the QD extracted using the Markovian approximation and the full non-Markovian model, where large deviations are observed close to resonance. The prediction from the Jaynes-Cummings model with no free parameters is seen to be in excellent agreement with the data. The upper temperature scale is approximate. **b)** The slow decay rate extracted for each measured decay curve. **c)** Reduced-chi-squared for the Markovian model showing the inability of the model to describe the data close to resonance.

Fig. 3.3(c). The inability of modeling the decay curves with the Markovian bi-exponential model is quantified by $\tilde{\chi}^2$, which we have plotted in Fig. 3.4(c). Close to resonance we observe significant deviations from the optimum value of unity proving that the Markovian model does not agree with the data, while all the non-Markovian fits give a value of $\tilde{\chi}^2$ close to unity [56].

Alternatively the deviations from the Markovian behavior observed in the experiment can be displayed by comparing the decay rate extracted from the Markovian model with the generalized decay rate $1/\langle t \rangle = \int_0^\infty \rho_{\mathrm{qd}} dt / \int_0^\infty t \rho_{\mathrm{qd}} dt$ obtained from the non-Markovian decay, cf. Fig. 3.4(a). The slow components are modeled for each decay curve individually, cf. Fig. 3.4(b), where a weak temperature dependence is observed, and in Fig. 3.4(a) only the radiative rate is shown. While the Markovian and non-Markovian rates as expected agree under far-detuned conditions, very pronounced deviations are observed close to resonance. Importantly, the rates extracted without making the Markovian approximation are seen to be described excellently by the predictions of the Jaynes-Cummings model without any adjustable parameters, as evident from Fig. 3.4(a). Making the Markovian approximation close to resonance greatly overestimates the decay rate to 35.6 ns^{-1}, while the correct value in the full non-Markovian model is 17.7 ns^{-1}. This would in turn lead to a large overestimate of the coupling strength. While previous studies have employed global-fitting routines to extract parameters from spectral measurements [58] or assumed reasonable values for the parameters [86], we stress that there are no free parameters in the comparison in Fig. 3.4(a), thereby making this the first quantitative study of a QD-based cavity QED system [56]. The role of pure dephasing is made clear by noting that the full-width at half-maximum (FWHM) of the Purcell enhanced region in Fig. 3.4(a) is 99.3 μeV, which is larger than the 88.3 μeV expected from a model without dephasing. This means, that pure dephasing broadens the Purcell enhanced region because it increases the linewidth of the QD, and the data in Fig. 3.4(a) constitutes the first experimental proof of this mechanism that was first predicted in [87].

Finally it is discussed how the remaining parameters for the comparison between experiment and theory were determined. The single-photon nature of the emission from the QD was verified by performing autocorrelation measurements using a Hanbury-Brown and Twiss interferometer, and details on this setup can be found in chapter 5. For large detunings we measure an antibunching of $g^{(2)}(\tau = 0) = 13.2\%$ under pulsed excitation conditions, proving that the QD acts as a single-photon emitter, where background emission only constitutes 6.6% of the total signal [69]. The coherence of the emission is measured by sending the emission to a Hong-Ou-Mandel interferometer [88, 72], where consecutively emitted photons are interfered on a 50 : 50 beamsplitter

and the coincidence counts are measured. If the photons are indistinguishable they will always bunch together in one arm, leading to a vanishing coincidence count a zero time delay. Dephasing will, however, randomly shift the QD emission frequency leading to a degradation of this effect, and we extract a degree of indistinguishability of 48%. From this overlap the pure dephasing rate of the QD can be extracted to $\hbar\gamma_{\mathrm{dp}} = 6.3 \pm 2.2$ μeV at T= 16.3 K. Details on both the physical effect and setup are presented in chapter 5. Below 60 K, the dephasing rate has been shown to depend linearly on temperature [89], which allows us to extract the derivative $\hbar\partial\gamma_{\mathrm{dp}}/\partial \mathrm{T} = 0.39 \pm 0.13$ μeV/K, which is valid in the temperature range where we perform the experiments $(10 - 23$ K) [56].

3.1.4 Detuning-dependent emission spectra

We now perform a similar comparison between experiment and theory in the spectral domain. For every detuning we have also recorded the emission spectrum and a few representative spectra are shown in Fig. 3.5. As shown in Eq. (2.30) the emission spectrum consists of both a cavity and QD part as well as the interference terms, but the individual prefactors are undetermined. The cavity contribution is expected to be dominant in the micropillar cavity due to the geometry, and in the modeling of the recorded spectra we therefore assume $\eta_{\mathrm{qd}} = 0$. On resonance we have performed an autocorrelation measurement of the emission that yields the value $g^{(2)}(\tau = 0) = 34.5\%$, which indicates additional feeding of the cavity from other QDs or multiexcitons. The detected signal can therefore be expressed as $I = I_{\mathrm{qd}} + I_{\mathrm{bg}}$, where the former part originates from the QD and the latter is due to the background. A background due to other recombination processes will have a thermal distribution [38] and is likely to be uncorrelated with the QD signal. Inserting the expression for the detected signal into the definition of the autocorrelation, $g^{(2)}(\tau = 0) = \frac{\langle I^2 \rangle}{\langle I \rangle^2}$, means that the background constitutes $\frac{g^{(2)}(\tau=0)}{2}$ of the total signal. An inhomogenous contribution to the cavity spectrum of 17.3% is therefore added to the calculated cavity spectrum. At each detuning the spectrum is calculated using the parameters determined from the time-resolved measurements, and the spectrum is convoluted with the spectral IRF and normalized to the QD peak, cf. Fig. 3.5.

We immediately notice that the calculated spectra consistently underesti-

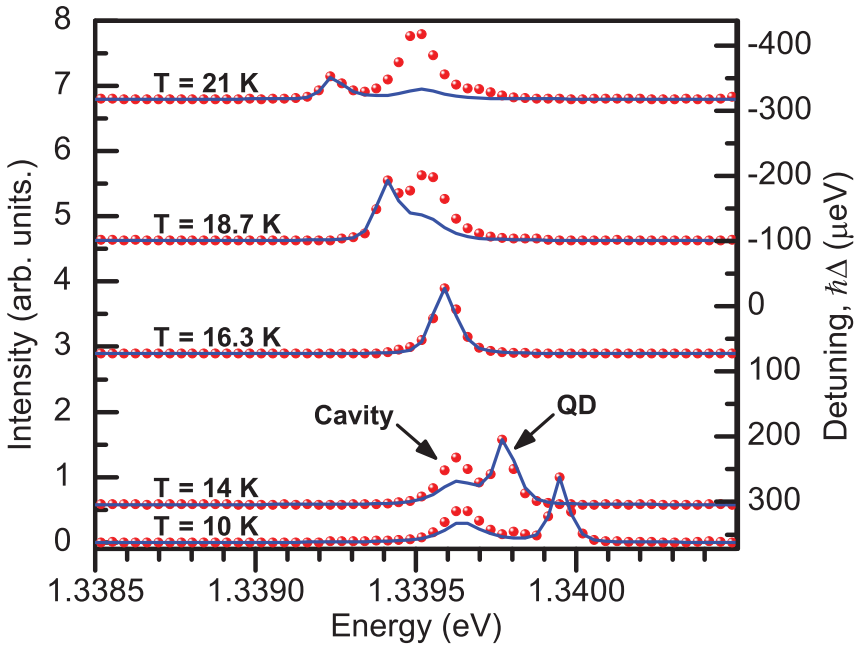

Figure 3.5: The measured spectra (red circles) for a QD in a micropillar cavity for various values of detuning, which is controlled by changing the temperature. The blue lines are the corresponding cavity spectra calculated without any free fitting parameters.

mate the intensity at the cavity peak. The asymmetry in the relative QD-cavity intensity cannot be reproduced by the theory and the disagreement between experiment and theory is large. There are, however, a number of effects that are not included in the theory, which may explain this discrepancy. Firstly, both the QD and interference terms are not included in the comparison. Because the coefficients η_{qd} and η_{ca} are not determined experimentally and are expected to be detuning dependent, the QD and interference terms cannot be included when performing the quantitative comparison, and in the previous chapter we demonstrated how important these contributions are for the total spectrum. Secondly, feeding of the cavity by other QDs and multiexcitons is known to increase the intensity at the cavity peak even when they are far detuned [36], which may contribute to the observed disagreement. Finally, all

the time-resolved measurements, including autocorrelation and two-photon interference measurements, all probe the dynamics and coherence at short time scales (of the order nanoseconds). In contrast, the spectra are integrated over much longer timescales (of the order seconds), which implies that they are sensitive to slow dephasing mechanisms, e.g. spectral diffusion, where changes in the electrostatic environment broadens the QD linewidth. As a result, spectral measurement can reveal a much broader QD compared to what is expected from time-resolved measurements. These complications lead to the conclusion that it is favorable to extract quantitative information about the system through time-resolved measurements rather than from spectral measurements, where we have observed systematic deviations between experiment and theory [69].

3.2 Photonic-crystal cavities

QD-cavity systems in the strong coupling regime have been the subject of an intense study [90, 91, 92] since the first demonstration of Rabi splitting in the spectrum [74, 73]. Due to the limited time-resolution offered by APDs, the strong coupling regime has been studied exclusively in the spectral domain, where e.g. global-fitting routines have been employed to extract the parameters from the vast parameter space [58]. Most notable, the appearance of a third peak at the bare cavity frequency was observed in an otherwise strongly coupled system, which was attributed to blinking of the QD [93]. In the following we present spectral measurements on a system that appears to be in the strong coupling regime, but time-resolved measurements prove that the system is in fact in the weak coupling regime.

3.2.1 Experimental setup

The setup used for measurements on photonic-crystal cavities is the same as used for micropillar cavities shown in Fig. 3.2 with minor modifications. The geometry of the photonic-crystal cavity does not easily allow for side-excitation, and instead a dichroic mirror, which reflects light below $\sim$ 860 nm and transmits light above $\sim$ 900 nm, is inserted on top of the microscope objective. The cavities of interest all have emission wavelengths above 900 nm, where the dichroic mirror transmits all the light, and the detection is done as shown in Fig. 3.2. For the data presented here, the QD is excited below 860 nm, where

the dichroic mirror reflects all light and thus allows for an easy separation of the excitation and emission. After coupling the excitation out of the single-mode fiber, the beam propagates through a PBS followed by a $\lambda/2$-plate for polarization control before being incident on the dichroic mirror. The mode structure of a photonic-crystal cavity was shown in Fig. 2.4, and we now excite the QDs spatially in the cavity by tuning the excitation laser into resonance with the M6-mode at 850 nm while observing the emission around the fundamental M1-mode at 952 nm. In this way we ensure that only QDs spatially coupled to the cavity are excited, and the spectrum becomes much cleaner compared to above-band excitation. In order to ensure efficient in-coupling, the polarization of the excitation laser is adjusted to match that of the M6-mode.

The detuning can still be varied by changing the temperature, but as seen in the case of micropillar cavities this results in a relatively small variable range ~ 1 meV. However, for photonic-crystal cavities we also have the possibility to change the cavity frequency by depositing small amounts of Nitrogen gas on the sample, which results in a small decrease in the radius of the holes [94]. Effectively this makes the cavity larger and the wavelength of the cavity shifts to longer wavelengths without any significant changes to the Q-factor of the cavity and combining this with temperature tuning gives a tuning range of over 6 meV. In practice, however, the cavity slowly drifts towards longer wavelengths even when Nitrogen is not introduced intentionally and the pressure remains low, $\sim 10^{-6}$ mbar, which has also been observed by others [35]. We find that the determining factor for this modewalking is the size of the window for the optical access. For the measurements we vary between two different lids, where the only difference is the diameter of the window seen by the sample which is 25 and 10 mm, respectively. Modewalking is significantly faster for the latter, where the mode drifts almost 0.8 nm over 90 min. as opposed to the former, where the cavity mode drifts less than 0.2 nm in the same time. Furthermore, it is observed that the drift always saturates after a characteristic time, which for the 25 mm window happens after almost 6 hours where it has drifted about 1 nm. We also observe that increasing the temperature to $16 - 18$ K results in the evaporation of the condensed material and the cavity wavelength thus goes back to the initial wavelength [95]. We note that a determining factor for the rate of modewalking seems to be the solid angle of the window seen from the

sample. The larger this solid angle is, the slower the modewalking happens. We note, that the timescale of the modewalking has to be much longer than the characteristic measurement times in order for the assumption of stable conditions to apply. This was indeed the case for the two lids mentioned, but we have also constructed a lid with a small nozzle that allows for the controllable deposition of Nitrogen onto the sample, and this resulted in a very fast modewalking that did not allow for measurements.

3.2.2 Detuning-dependent emission spectra

The cavity studied here has a lattice constant $a = 240$ nm and hole radius $r = 65$ nm, and the three holes at each end of the cavity have been shifted in order to increase the Q-factor as explained in section 2.3. The Q-factor is measured to a moderate 6690 ± 37 corresponding to $\hbar\kappa = 195 \pm 1$ μeV under high excitation power. The detuning-dependent spectra are shown in Fig. 3.6(a), where the cavity is tuned through the QD while the temperature is fixed at T= 10 K.

The measured spectrum is the spectrum emitted from the QD-cavity system convoluted with the spectrometer IRF. Importantly the convolution theorem states that a convolution in one domain is a simple product in the complementary domain [96]. Using this we can deconvolute the measured spectra by performing an inverse Fourier transform, dividing by the inverse Fourier transformed IRF and multiply by a bandpass filter in order to reduce noise, before finally transforming back to the frequency domain [97]. The validity of this procedure is carefully checked by convoluting the deconvoluted spectra with the IRF and comparing to the measured spectra. The deconvoluted spectra are fitted by two Lorentzians each having the center, width, and amplitude as free parameters, and in Fig. 3.6 the measured spectra are shown together with the convoluted fits [69]. The limitations to the quantitative knowledge that can be extracted from spectral measurements, as was discussed in the context of micropillars in the previous section, also applies to photonic-crystal cavities. However, in the following we will focus on investigating the Rabi splitting that has been widely studied in the literature [74, 73, 93, 58] and is considered to be a robust measure of the light-matter coupling strength between the QD and cavity.

Figures 3.6(b)-(d) show the quantities extracted from modeling the mea-

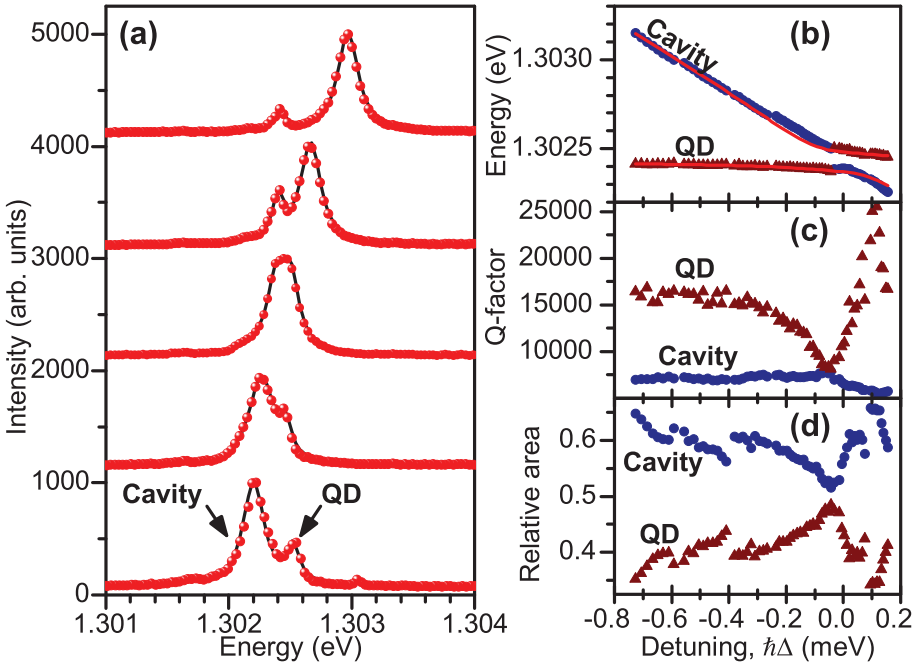

Figure 3.6: **a)** The recorded emission spectra (red circles) of a QD-cavity system, where the cavity is tuned through the QD by gas deposition at T = 10 K. The black line is the fit with two Lorentzians after convolution with the spectrometer IRF. **b-d)** The resonance energy, Q-factor, and relative area of the two peaks, respectively, as a function of detuning. Red lines are the fit of the cavity spectra from the JC model used to extract the coupling strength. The relative area of e.g. the QD is defined as $A_{qd}/(A_{qd}+A_{ca})$ where A_{qd} (A_{ca}) is the area of the QD (cavity) peak.

sured spectra, i.e. the energy of the two resonances, their Q-factors and the area of each Lorentzian relative to the total area. In Fig. 3.6(b) a clear anti-crossing is observed close to resonance, which is considered to be the tell-tale sign of strong coupling. Fig. 3.6(c) shows that the Q-factors become identical on resonance, but for a strongly coupled system the two peaks are expected to share the total linewidth on resonance. This means that while the cavity and QD have the linewidths κ and $\gamma + 2\gamma_{dp}$ far from resonance, their linewidths

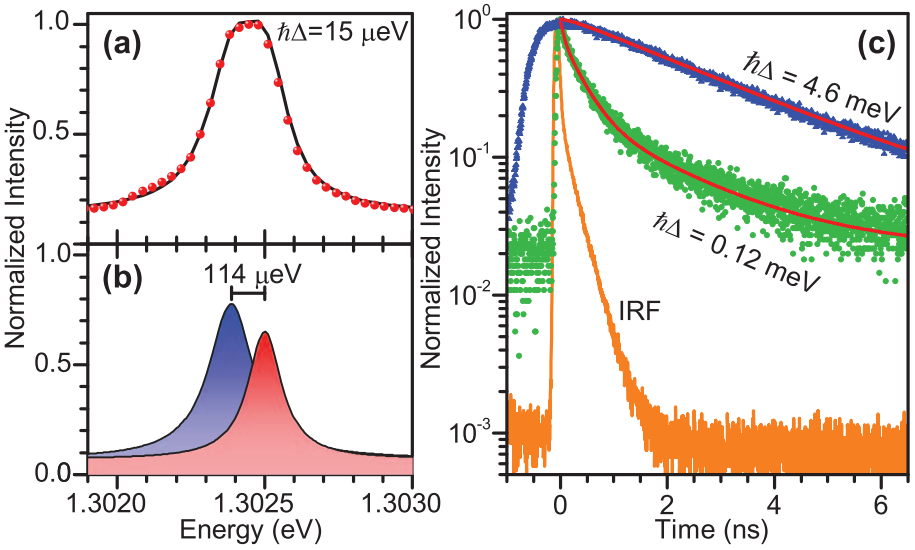

Figure 3.7: **a)** The measured emission spectrum (red circles) at detuning $\hbar\Delta = 15$ μeV together with the double Lorentzian fit. **b)** The deconvoluted fit decomposed into the two Lorentzians showing a Rabi splitting of $\hbar\Omega = 114$ μeV. **c)** The measured decay curves close to resonance ($\hbar\Delta = 0.12$ meV) and far-detuned ($\hbar\Delta = 4.6$ meV) along with their fits (red lines) showing a strong Purcell enhancement. We extract the decay rates 18.5 ns^{-1} and 0.39 ns^{-1}, respectively, and the IRF of the APD is shown for reference.

should both equal $(\kappa + \gamma + 2\gamma_{\text{dp}})/2$ corresponding to Q= 12820 on resonance, which is seen not to be the case in Fig. 3.6(c) although the Q-factor of the cavity does increase slightly. We note that the increase in Q-factors for the QD peak observed for positive detunings is most likely an artifact of the deconvolution process because the Q-factor of the QD is close to the resolution of the spectrometer, which corresponds to Q= 32560. Finally, Fig. 3.6(d) shows that while the relative area of the cavity peak dominates away from resonance, the two peaks have almost equal intensity on resonance, as expected for a system in the strong coupling regime [69].

Fig. 3.7(a) shows the spectrum recorded almost at resonance ($\hbar\Delta = 15$ μeV) together with the convoluted double Lorentzian fit, and in Fig. 3.7(b) the fit

is decomposed into the two Lorentzian functions. We observe a clear splitting between the two peaks that have almost the same width and area, as can also be seen in Fig. 3.6(c-d). This is also expected for a strongly coupled system, where the single excitation coherently oscillates back and forth between the QD and cavity mode thereby creating two indistinguishable alternatives. The splitting between the two peaks is $\hbar\Omega = 114$ μeV. Assuming the splitting is a vacuum Rabi splitting we extract the coupling strength $\hbar g = 92.4$ μeV using the Jaynes-Cummings model with the measured values for the parameters κ and γ, and using a realistic pure dephasing rate of $\hbar\gamma_{\mathrm{dp}} = 4$ μeV [56]. The ability of this model to describe the detuning dependence of the resonance energies is evident from Fig. 3.6(b), where there is an excellent agreement.

Finally we note, that the energy of the QD peak in Fig. 3.6(b) is shifted slightly down for negative detunings and up for positive detunings with respect to the center of the splitting on resonance. This energy shift can be considered the cavity-assisted Lamb shift, where the modification of the LDOS gives rise to a frequency shift. As is evident from Fig. 3.6(b) this cavity-assisted Lamb shift depends on detuning, which is reproduced by the model, and we attribute it to conservation of energy. Initially the QD is excited but part of the emission is at the higher cavity frequency, and in order to fulfil energy conservation in the emission spectrum, the QD energy is shifted in the direction opposite of the cavity.

3.2.3 Comparing spectra with dynamics

As described in section 3.1.3 a quantitative measure of the coupling strength can be obtained from time-resolved measurements, which allows us to test the validity of the Rabi splitting extracted from the spectra. In Fig. 3.7(c) examples of measured decay curves for large detunings ($\hbar\Delta = 4.6$ meV) and close to resonance ($\hbar\Delta = 0.12$ meV), respectively, are shown together with their fits. As described, the decay curve of a QD is expected to be bi-exponential, where the slow rate only contains the non-radiative rate, while the fast also contains the radiative rate. For very large detunings the radiative rate is strongly inhibited by the photonic crystal, and the decay curves consequently appear to be single-exponential. We use the same fitting routine that was outlined previously and for the far-detuned decay curve in Fig. 3.7(c) we extract a decay rate of 0.39 ns^{-1}, corresponding to $\hbar\gamma = 0.2$ μeV.

When the QD is tuned closer to resonance the decay rate gets Purcell enhanced and consequently the decay becomes bi-exponential. However, for detunings $\hbar|\Delta| < 0.5$ meV additional exciton lines and multiexcitons feed the cavity and this cannot be spectrally filtered because of the small detuning. As a result an extra exponential decay must be added in order to model the decay curves successfully, where we extract the fast decay rate that will be dominated by the resonant exciton [69]. We will discuss this in detail in the next chapter. From the decay curve close to resonance ($\hbar\Delta = 0.12$ meV) we extract a rate of 18.5 ns^{-1}, corresponding to a Purcell enhancement of 47.4 obtained by comparing to the far-detuned case. Similarly we can compute the emission into the cavity mode relative to the total emission, i.e. the beta factor, which gives us $\beta = (18.5 - 0.39)/18.5 = 97.9\%$.

By using the expression for the Purcell factor derived in Eq. (2.25) we conclude that the coupling strength in the photonic-crystal cavity is only 3.2% of the maximum achievable value for an emitter positioned optimally in an antinode of the cavity with aligned dipole moment, while for comparison this value is 19% for the previously studied micropillar cavity. Because light is confined much tighter in the photonic-crystal cavity it is also more sensitive to the spatial position of the QD, and the probability of having a QD at the maximum of the field is thus lower.

From the time-resolved data we now extract a coupling strength of $\hbar|g| = 22 \pm 0.7$ μeV, which surprisingly is more than four times smaller than that obtained from the spectral Rabi splitting. This proves that the system is in fact not in the strong coupling regime but rather well inside the weak coupling regime. This pronounced discrepancy is another example of the incompatibility of the information extracted from spectral and time-resolved measurements. For the latter measurements only a narrow spectral region is sent to the APD, and we can be confident that we are primarily probing the dynamics of the single excition line. In contrast, spectral measurements also contain contributions from other QDs and/or multiexcitons that feed the cavity [98, 99], which has been experimentally confirmed by autocorrelation measurements of the cavity peak that showed bunching although the cavity was being fed by a single QD [36].

Consequently we suggest that the additional feeding of the cavity can give rise to collective effects and that the Rabi splitting observed spectrally is due

not to the coupling strength of the single exciton but rather to the collective coupling strength of all the emitters. The clean spectra in Fig. 3.6(a) suggest that there are no other excitons contributing to the coupling, but the intensity in the cavity peak is systematically larger than the intensity in the QD peak, cf. Fig. 3.6(d), which supports the hypothesis that multiexcitons are feeding the cavity. As described in chapter 2, multiexcitons originate from a single QD where, e.g., a ground state exciton scatters of an additional charge in either the wetting layer or higher states of the QD. Through the scattering process, the exciton is brought to a virtual level at ,e.g., a lower energy from where it recombines optically. This creates a quasi-continuum on both energy sides of the ground state exciton, but this is several orders of magnitude weaker than the ground state exciton [34, 35]. However, when the QD is embedded in a high-Q cavity this background will experience a significant and broadband Purcell enhancement and contribute to the cavity intensity [36]. The situation of a continuum of emitters all with equal coupling strengths has been studied in [100], where it was shown that the collective effects could give rise to strong coupling. This can be understood by considering the well-known situation of N identical emitters that give rise to a collective coupling strength $\sqrt{N}$ times larger than the individual coupling strengths. As a model system, we have studied the case of two emitters without assuming them to be identical, and have verified that adding an additional emitter can bring the system into strong coupling [64]. While the observed anti-crossing and equal area of the two peaks agree with vacuum Rabi splitting, the lower cavity Q-factor did not increase on resonance as expected for a single QD coupled to the cavity, since the total linewidth should be shared between the two peaks. However, if a multiexcitonic background is also coupling to the cavity, the total linewidth of the system would be much larger and could potentially explain why the lower cavity Q-factor does not increase on resonance. This collective coupling could also potentially explain the surprisingly large Rabi splitting observed in other strong-coupling experiments that were initially suggested to be a consequence of the giant oscillator strength of the large QDs [73], but this explanation was found unsatisfactory through detailed measurements of the oscillator strength [101].

3.3 Conclusion

We have performed a quantitative analysis of the dynamics and emission spectra of single QDs embedded in two of the commonly studied cavities. Measurements of the dynamics of a single QD in a micropillar revealed that the dynamics become non-Markovian when the QD is close to resonance with the cavity. The non-Markovian effects arising from the back-action from the photon reservoir revealed themselves as a offset in the measured decay curves that could not be explained by an exponential decay. Failing to account for the non-Markovian effects was shown to lead to a large overestimate of the light-matter coupling strength. We described the dynamics by the full dissipative Jaynes-Cummings model, where we independently measured all the parameters and we found an excellent agreement with no free parameters, thus providing a quantitative understanding. The observation of non-Markovian dynamics is, to our knowledge, the first experimental demonstration in solid-state cavity QED.

After determining all the parameters and having shown the agreement with theory for the dynamics, we performed the same comparison in the spectral domain. The full emission spectrum contains both a cavity and QD part as well as their mutual interference terms, but we miss the microscopic insight into the parameters determining the relative contributions and from geometrical consideration we compared only with the spectrum arising from the cavity part. Even after accounting for inhomogenous contributions to the cavity, we find a large disagreement between measured and calculated spectra. We attribute a large part of this discrepancy to the neglection of the QD and interference terms. This lead us to the conclusion that spectra cannot be used for quantitative comparisons without insight into the microscopic mixing of the different contributions to the spectrum.

We have performed a similar analysis on a single QD in a photonic-crystal cavity by recording the detuning-dependent emission spectra, where clear signs of strong coupling were observed. The two peaks showed an anti-crossing and although the expected linewidth narrowing on resonance did not occur, the relative areas of the two peaks did become close to equal as expected for a strongly coupled system. Assuming that the observed anti-crossing was due to a vacuum Rabi splitting, we extracted the coupling strength $\hbar|g| = 92.4$ μeV.

Time-resolved measurements did, however, reveal that the system was in fact not strongly coupled by rather well inside the weak coupling regime and

we extracted a coupling strength of $\hbar|g| = 22 \pm 0.7$ μeV, which is less than one fourth of that extracted from the splitting. As argued, time-resolved measurements allow us to reliably extract information on the single exciton due to the spectral filtering, whereas spectral measurements are sensitive to feeding of the cavity by multiexcitons and other QDs. We suggest, that the spectral splitting is a result of collective effects, where the single exciton and a multiexcitonic background interacts with the cavity and gives rise to a collective Rabi splitting. This effect could explain the observed discrepancy between parameters extracted from the spectral measurements as well as the disagreement with time-resolved measurements.

Chapter 4

Measuring the effective phonon density of states of a quantum dot

Mechanical motion due to thermal vibrations, i.e. phonons, is omnipresent in solid-state systems and inevitably leads to decoherence of quantum superposition states encoded in the system. Understanding and ultimately engineering phonon processes may thus lead to new opportunities for coherent quantum optics in all solid-state systems. Photonic crystal cavities provide an exciting platform that not only allows for studies of the cavity quantum electrodynamics of the interaction between a single emitter and a localized electromagnetic field, but also their interaction with the mechanical degrees of freedom of the photonic-crystal membrane. Recent work on cavity optomechanics has demonstrated how the cavity structure modifies the interaction between the optical and phononic modes [102, 103], which can even give rise to mechanical modes localized within the cavity [104] that can be modulated using gigahertz acoustic phonons [105]. Furthermore, the emerging field of quantum optomechanics explores the ultimate quantum mechanical motion of, e.g., nanomembranes [9], and generating carriers in semiconductor membranes has been proven to enable novel mechanical cooling mechanisms [106, 107].

In this chapter we explore the mechanical degrees of freedom in cavity quan-

tum electrodynamics. Although the solid-state environment is non-Markovian in its nature, it has successfully been described as Markovian because the timescale of the correlations of the environment are orders of magnitude faster than those of the optical transitions in the QD [108]. However, the influence of the non-Markovian environment has been observed for QDs in bulk as a phonon sideband mainly on the low energy side of the zero-phonon line, and it arises from the accompanying emission of phonons [30]. Previous studies were only possible at elevated temperatures, where the phonon dephasing is very pronounced, and quantities governing the phonon interaction could be modeled [109]. In addition, a temperature dependent broadening of the zero-phonon line was also observed, which could be attributed to thermal activation of spectral diffusion [31] and interaction with linewidth-broadened phonons [110].

The modification of optomechanical properties arising from the introduction of optical cavities in photonic-crystal membranes, naturally leads to the speculation that the effective phonon density of states experienced by a single QD in the cavity may be modified. As a result, this could possibly minimize the deteriorating influence of decoherence processes. The phonon-mediated coupling in a cavity has been studied spectrally [111], but as discussed in chapter 3 it is difficult to perform a quantitative comparison based on emission spectra. Previous temporal studies [86] of the phonon-mediated coupling have also not been able to perform a quantitative analysis but have rather relied on assuming reasonable values for the parameters.

In this chapter we study the temporal evolution of a single QD embedded in a photonic-crystal cavity. We will show how the cavity enhances the electron-phonon coupling and how a quantitative comparison allows us to for the first time extract the effective phonon density of states, which governs all the phonon dephasing properties of the QD. With this description we can also explain the differences to other cavities such as Anderson localized cavities in a photonic-crystal waveguide and micropillar cavities that do not show similar broadband Purcell enhancements. Remarkably, we demonstrate that the phonons interacting with the QD are very well described as bulk phonons despite the inhomogeneity of the cavity. This chapter is based on the work we have submitted for publication in [55].

4.1 Electron-phonon interaction

Although the dissipative Jaynes-Cummings model derived in section 2.4 excellently describes both the coherent light-matter interaction as well as the optical dissipation, as shown in the previous chapter, the inclusion of the solid-state environment as a simple pure dephasing of the energy levels does not suffice for describing a QD in a photonic-crystal cavity. In the following we will outline a theory that takes the non-Markovian solid-state environment into account by including processes, where the polariton quasi-particle is dephased by phonon processes mediated by longitudinal acoustic (LA) phonons. We exclude transverse acoustic (TA) phonons because they only couple through the piezoelectric constant, which is much smaller than the deformation potential that LA phonons couple through. The piezoelectric coupling is a polar interaction mechanism that relies on the change of the electric dipole orientation when mechanical stress is applied. Polar mechanisms are completely absent if the system is locally electrically neutral, i.e., if the electron and hole wave functions are identical. The large electron-hole overlap in QDs therefore strongly reduces all polar interactions and TA phonons are as a result neglected [112]. Optical phonons are out of phase movements of the atoms in the lattice, which in the simple diatomic linear chain model can be understood as the two atoms within the unit cell moving in opposite direction, as opposed to acoustic phonons where the two atoms move in the same direction [21]. The dispersion relation for longitudinal optical (LO) phonons is non-zero at zero phonon wavevector and the energy of them is calculated to 36.8 meV [112]. This energy is an order of magnitude larger than the QD-cavity detunings considered here and consequently we can neglect LO phonons, although in chapter 5 we show how they can be used for efficient excitation of QDs. Finally, we note that although photon-phonon interaction has recently been observed by optically pumping the cavity [104], these effects are strongly dependent on the number of photons in the cavity and are orders of magnitude smaller than the coupling to LA phonons described here.

The hamiltonian shown in Eq. (2.15) describes the coherent light-matter interaction. We now add the electron-phonon interaction terms and obtain the

hamiltonian [108]

$$\begin{aligned}\hat{\mathrm{H}} = &\hbar\Delta\hat{\sigma}_+\hat{\sigma}_- + \hbar g(\hat{\sigma}_+\hat{a} + \hat{\sigma}_-\hat{a}^\dagger) \\ &+ \hat{\sigma}_+\hat{\sigma}_- \sum_{\mathbf{k}} \mathbf{M}^{\mathbf{k}}(\hat{b}^\dagger_{-\mathbf{k}} + \hat{b}_{\mathbf{k}}) + \sum_{\mathbf{k}} \hbar\omega_{\mathbf{k}}\hat{b}^\dagger_{\mathbf{k}}\hat{b}_{\mathbf{k}} \ , \end{aligned} \tag{4.1}$$

where the third term describes the electron-phonon interaction and the last term describes the free phononic modes. $\hat{b}_{\mathbf{k}}$ and $\hat{b}^\dagger_{\mathbf{k}}$ are the bosonic annihilation and creation operators for the kth phonon mode, and $\mathbf{M}^{\mathbf{k}} = \mathbf{M}^{\mathbf{k}}_{\mathrm{ee}} - \mathbf{M}^{\mathbf{k}}_{\mathrm{gg}}$ is the effective interaction matrix element, here expressed as the difference between the excited and ground state interaction matrix elements. We see that interaction with the phonons does not give rise to real transitions but rather virtual transitions, where a phonon in the kth mode is absorbed and a phonon is emitted into the $-k$th mode, while preserving the QD population. Deriving the equations of motion is rather complicated but shown in full detail in [108]. Here it suffices to note that the electron-phonon interaction is treated by applying the time-convolutionless approach, which essentially includes the electron-phonon interaction as a Lindblad term with a time-dependent scattering rate. This approach preserves the non-Markovian description of the dynamics. The equation of motion are thus the same as derived in Eq.(2.17):

$$\dot{\rho} = -i\hbar^{-1}[\hat{H}_{JC}, \rho] + \mathcal{L}(\kappa, \hat{a}) + \mathcal{L}(\gamma, \hat{\sigma}_-) + S_{LA}(t) \ , \tag{4.2}$$

only with the addition of a time-dependent scattering term, $S_{LA}(t)$, arising from the interaction with the LA phonons. We have also excluded the pure dephasing rate as this is now described by the electron-phonon interaction. The coupling strength g is assumed to be real. The hamiltonian $\hat{H}_{JC}$ contains the first two terms in Eq. (4.1), as derived in section 2.4. The equations of motion for the populations can be written as three coupled differential equations [113] with additional time-dependent terms in the polarization. When considering the dynamics, a long-time limit can be taken and the equations can be written in the form

$$\begin{aligned}\dot{\rho}_{\mathrm{qd}} &= -\gamma\rho_{\mathrm{qd}} - g^2[K(t) + K^*(t)] \ , \\ \dot{\rho}_{\mathrm{ca}} &= -\kappa\rho_{\mathrm{ca}} + g^2[K(t) + K^*(t)] \ , \\ K(t) &= \int_0^t dt' \mathrm{e}^{-(\gamma_{\mathrm{tot}} - i\Delta + \mathrm{Re}(\gamma_{12}))(t-t')} \left[\left(1 + \frac{\mathcal{G}^>}{g}\right)\rho_{\mathrm{qd}}(t') - \left(1 + \frac{\mathcal{G}^<}{g}\right)\rho_{\mathrm{ca}}(t')\right] \end{aligned} \tag{4.3}$$

where $K(t)$ serves as a memory kernel and the influence of the electron-phonon interaction enters through $\mathcal{G}^{\gtrless}$ and γ_{12}. By setting these terms to zero we recover the result from the Jaynes-Cummings model shown in Eq.(3.1), with the only difference that there is no pure dephasing rate, i.e. $\gamma_{\rm tot} = (\kappa + \gamma)/2$. The rate γ contains both coupling to radiation modes and nonradiative recombinations. The real part of the quantities $\mathcal{G}^{\gtrless}$ renormalizes the light-matter coupling strength g, but in general $\mathrm{Re}[\mathcal{G}^{<}] \neq \mathrm{Re}[\mathcal{G}^{>}]$ thus the renormalization does not correspond to an overall change in the value of g. The imaginary part of $\mathcal{G}^{\gtrless}$ gives rise to additional decay or growth of the polarizations. The real part of γ_{12} gives rise to a pure dephasing rate and the imaginary part gives rise to a small energy shift that has been absorbed into the detuning Δ [108]. In order to gain more insight on these processes, we now consider the case of resonance ($\Delta = 0$), where the two quantities can be expressed as

$$\mathcal{G}^{\gtrless}_{\Delta=0} = \frac{1}{2\hbar^2}\int_0^\infty \sin(2gt')D^{\gtrless}(t')dt' \,, \tag{4.4}$$

$$\gamma_{12}^{\Delta=0} = \frac{1}{\hbar^2}\int_0^\infty D^{<}(t') - \sin^2(gt')[D^{<}(t') + D^{>}(t')]dt' \,, \tag{4.5}$$

where $D^{\gtrless}$ are the phonon-bath correlation functions. It is clear that the relevant figure of merit is the timescale over which the phonon bath correlations decay (typically a few picoseconds) relative to the timescale over which Rabi oscillations occur. If the latter occurs on a much slower timescale, then the renormalization of the coupling strength vanishes ($\mathcal{G}^{\gtrless}_{\Delta=0} = 0$) and $\gamma_{12}^{\Delta=0} = \frac{1}{\hbar^2}\int_0^\infty D^{<}(t')dt'$ becomes the pure dephasing rate. The effect of the electron-phonon interaction on the Purcell enhancement in the weak coupling regime can be derived by adiabatically eliminating the polarization in Eq. (4.3). The detuning-dependent decay rate can then be expressed as [108]

$$\Gamma = \gamma + 2g^2\frac{\gamma_{\rm tot}}{\gamma_{\rm tot}^2 + \Delta^2}\left[1 + \frac{1}{\hbar^2\gamma_{\rm tot}}\Phi(\Omega = \Delta, T)\right] \,, \tag{4.6}$$

where the effective phonon density experienced by the QD is defined as

$$\Phi(\Omega, T) = \pi\sum_{\mathbf{k}} |\mathbf{M}^{\mathbf{k}}|^2 \left[n_{\mathbf{k}}(T)\delta(\Omega + \Omega_{\mathbf{k}}) + (n_{\mathbf{k}}(T) + 1)\delta(\Omega - \Omega_{\mathbf{k}})\right] \,. \tag{4.7}$$

In the last equation, $n_{\mathbf{k}}(T) = (\mathrm{e}^{\hbar\Omega_{\mathbf{k}}/k_BT} - 1)^{-1}$ is the Bose-Einstein distribution, and $\Omega_{\mathbf{k}}$ is the frequency for the kth phonon mode. $\Phi(\Omega, T)$ can be

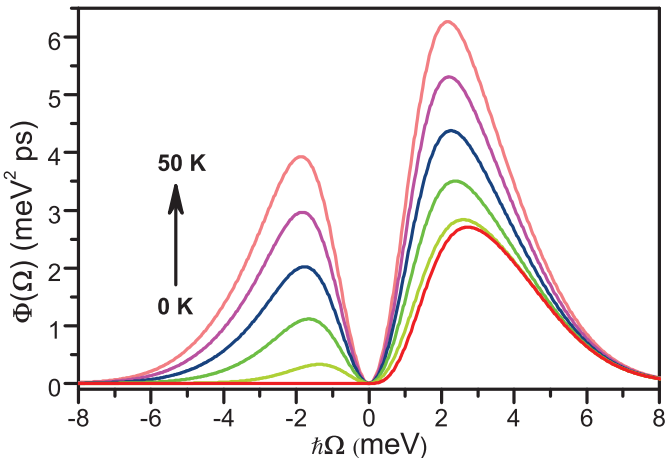

Figure 4.1: The effective phonon density versus energy plotted for 0 to 50 K with steps of 10 K. The asymmetry reflects the difference between emission of phonons, responsible for the decay at positive detunings, and absorption of phonons that are available but sparse at negative detunings. This can be viewed as the difference between vacuum and thermal fluctuations of the phonon field.

considered the effective phonon density experienced by the QD, because when evaluated at a given detuning and temperature it tells how phonons can assist the QD in decaying into the cavity mode. This happens with the accompanying emission or absorption of a phonon with the energy given by the detuning. The effective phonon density is plotted in Fig. 4.1 for the parameters extracted later in this chapter and shows a pronounced asymmetry at low temperatures. The strong asymmetry at low temperatures illustrates the fact that for positive detunings $\omega_{\mathrm{qd}} > \omega_{\mathrm{ca}}$, a QD detuned many linewidths away from the cavity resonance can still emit photons into the cavity mode through the accompanying emission of a phonon, while a negatively detuned QD relies on the absorption of a phonon, which is unlikely at low temperatures. For example, at T = 10 K and phonon energies larger than 1 meV, which are typical values in the present experiment, we estimate $n \leq 0.45$, meaning that the probability for phonon emission ($\propto n + 1$) and absorption ($\propto n$) varies significantly. As the temperature increases the asymmetry becomes less pronounced, but it does not

vanish because the thermal occupation of the phonon modes gives rise to stimulated phonon emission. The broad energy range of $\Phi(\Omega, T)$ and the relation in Eq. (4.6) gives rise to a broadband enhancement of the decay rate when the interaction with LA phonons is included. Alternatively, the term $\hbar^{-2}\Phi(\Omega, T)$ that has dimensions of a rate can be considered a phonon scattering rate describing the possibility of an exciton to scatter off a phonon and decay optically into the cavity mode.

4.2 Detuning-dependent dynamics

For measurements on the photonic-crystal cavities we use the experimental setup described in section 3.2.1, where confocal microscopy is employed and a dichroic mirror is used to separate the excitation from the emission. The cavity is excited by tuning the laser into resonance with the M6-mode situated at 850 nm, which results in a clean emission spectrum around the fundamental M1-mode, since only QDs spatially coupled to the cavity are excited. As described previously, the detuning between the QD and the cavity is controlled by both temperature tuning in the range $10 - 46$ K and deposition of Nitrogen gas on the sample, which redshifts the QD and cavity resonance, respectively. After polarization selection, the emission is sent to a spectrometer, where the output can be directed to a CCD camera for spectral measurements or to an APD for time-resolved measurements. For this cavity we measure $Q = 6690 \pm 37$, corresponding to a cavity decay rate of $\hbar\kappa = 195 \pm 1$ μeV, by saturating the QDs and recording the cavity linewidth. Fig. 4.2 shows examples of recorded decay curves for three very different detunings together with their fits. The presence of both bright and dark exciton states results in a bi-exponential decay, where the fast rate is approximately equal to the sum of the radiative and non-radiative rate, while the slow rate is equal to the non-radiative rate. The fast rate, which gives the decay of the bright exciton, is therefore the relevant rate for the comparison to theory. For large detunings, the QD decays very slowly because the radiative rate is strongly suppressed due to the presence of the photonic bandgap. The decay in this case is well fitted by a single exponential since the radiative rate is smaller than the non-radiative rate. This is evidenced by the low value of the goodness-of-fit parameter $\tilde{\chi}^2 = 1.11$ obtained for the fit in Fig. 4.2(a), where the temporal resolution (IRF), taken under the

same experimental conditions, is accounted for by convoluting the fit with the measured IRF before comparing to the recorded decay curve, as described in more detail in section 3.1.3. We obtain the decay rate $\Gamma = 0.39$ ns^{-1} from the far-detuned ($\hbar\Delta = 4.59$ meV) decay curve shown in Fig. 4.2(a), and since the cavity is not expected to contribute to the decay rate of the QD at such large detunings, we can use this decay rate to determine the background decay rate to $\hbar\gamma = 0.2$ μeV. For smaller detunings the radiative decay rate is enhanced and the decay is bi-exponential as expected, and in Fig. 4.2(b) such a decay curve is shown ($\hbar\Delta = 1.33$ meV), where we extract the rates $\Gamma_{\text{fast}} = 3.24$ ns^{-1} and $\Gamma_{\text{slow}} = 0.66$ ns^{-1}. The bi-exponential decay proves that it is not a charged exciton, e.g., an exciton and an additional electron, because charged excitons do not have dark states and consequently their decay follows a single exponential model. The exciton also displays a linear power dependency, which rules out bi-excitons that have super-linear power dependencies. This makes it possible to conclude that it is a neutral exciton we are measuring on. Finally, in Fig. 4.2(c) a decay curve close to resonance ($\hbar\Delta = 0.12$ meV) is shown. Here we observe that we cannot fit the data with a bi-exponential model, as evidenced by an increase in $\tilde{\chi}^2$. For detunings larger than the cavity linewidth, the exciton dynamics under the sole influence of phonons is probed, because only a small spectral region around the QD is sent to the APD. However, when the QD is close to resonance with the cavity, the emission from other QDs and/or multiexcitons that decay through the cavity will also influence the recorded decay curves, since it is not possible to spectrally filter these contribution away [55]. An example of a spectrum recorded under far-detuned conditions is shown in Fig. 4.3(b), where it is illustrated that a small spectral region is filtered out for time-resolved measurements which only away from resonance guarantees that we probe just the single exciton. Consequently we observe that for detunings $\hbar|\Delta| < 0.5$ meV the decay curves appear to be triple-exponential, where the fast rate is expected to be dominated by the resonant exciton, cf. Fig. 4.2(c).

As argued in section 3.2.3 the clean spectra, cf. Fig. 4.3(b), indicates that there are no significant contributions from other QDs, while the intense cavity indicates that multiexcitons are feeding the cavity as previous work has demonstrated [36]. However the multiexcitonic background is typically more than two orders of magnitude smaller than the exciton peak [34, 35]. This is due to the fact that the multiexcitonic background can be considered as the

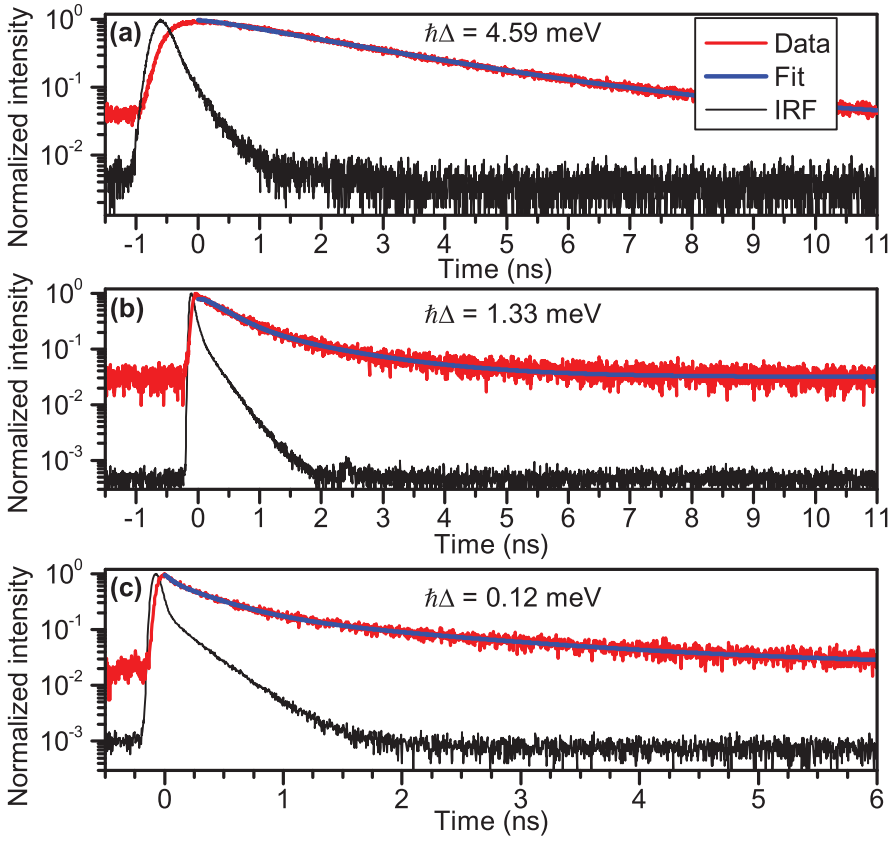

Figure 4.2: Recorded decay curves for three different detunings together with their fits that take the recorded time-resolution (IRF) into account. **a)** For the QD far-detuned from the cavity ($\hbar\Delta = 4.59$ meV) the decay is single exponential showing a decay rate of $\Gamma = 0.39$ ns^{-1} and a goodness-of-fit of $\tilde{\chi}^2 = 1.11$. **b)** For moderate detunings ($\hbar\Delta = 1.33$ meV) the decay is bi-exponential with $\Gamma_{\text{fast}} = 3.24$ ns^{-1}, $\Gamma_{\text{slow}} = 0.66$ ns^{-1}, and $\tilde{\chi}^2 = 1.09$. **c)** Close to resonance ($\hbar\Delta = 0.12$ meV) the decay becomes triple-exponential with $\Gamma_{\text{fast}} = 18.6$ ns^{-1}, $\Gamma_{\text{middle}} = 3.61$ ns^{-1}, $\Gamma_{\text{slow}} = 0.56$ ns^{-1}, and $\tilde{\chi}^2 = 0.98$

exciton scattering off other carriers via the Coulomb interaction, but with a low scattering rate. Therefore, the neutral exciton is expected to be dominant in intensity and have the fastest decay rate close to resonance, where the cavity

and QD cannot be separated spectrally. If we consider multiexcitons to form a continuum, where each constituent has a Purcell-enhanced amplitude and decay rate dictated by the cavity, then the resulting decay can be described as a single exponential decay with an effective amplitude and decay rate. For this reason we attribute the additional exponential with the middle decay rate to the multiexcitonic background. Following the reasoning above, the slow decay rates obtained from the bi- and triple-exponential fits should not change, which in Fig. 4.2(c) is shown to also be the case.

In Fig. 4.3(c) the measured decay rates are plotted as a function of detuning. Because temperature varies across the data set, the color of each data point corresponds to the temperature used for that particular measurement. We observe a large and very broadband Purcell enhancement of the QD decay rate. Though we can not access the statistical uncertainty of each point, since the uncertainty obtained from the fit will mainly reflect the quality of the fit and not the reproducibility of the data point, we can still still judge the statistical uncertainty from the point-to-point fluctuations in Fig. 4.3(c) since the sampling of the detuning is very high. Close to resonance we observe a large scattering of the data points, which we attribute to the presence of multiexcitons. From the data points close to resonance we extract the coupling strength to $\hbar g = 22 \pm 0.7$ μeV using Eq. (4.6) with the independently measured values of κ and γ and the fact that on resonance $\Phi(\Omega = 0, T) \simeq 0$, cf. Fig. 4.1. The applied excitation power is 1.5 times the saturation power of the QD except for $\hbar\Delta < -0.5$ meV and $\hbar\Delta > 2$ meV, where the power is 0.7 times the saturation power [55].

For comparison we have plotted the Purcell enhancement expected from the Jaynes-Cummings model using these parameters. In Fig. 4.3(c) we see the complete inability of this model to describe the measured data. However, we also plot the model introduced in the previous section that includes LA phonon-assisted transitions and we observe a very good agreement. Through the effective phonon density, $\Phi(\Omega, T)$, this model also depends on temperature and in Fig. 4.3(c) we have shaded the area between the theory curve for the highest (46 K) and lowest (10 K) temperature. The data away from resonance are seen to fall in-between these two curves while a larger degree of scattering is observed close to resonance. In order to make a complete comparison we have calculated the expected decay rates for each measured decay rate at

the temperature used experimentally (black diamonds). Fig. 4.3(d) shows the residuals $(\Gamma_{\mathrm{exp}} - \Gamma_{\mathrm{the}})/\Gamma_{\mathrm{exp}}$ between the experimental, Γ_{exp}, and theoretical, Γ_{the}, decay rates. We have inserted a guide to the eye that shows the excellent agreement for $\hbar|\Delta| > 0.5$ meV, while a larger degree of scattering is observed close to resonance.

The broadband Purcell enhancement occurs because for positive detunings the QD emits a photon into the cavity mode while the residual energy is emitted as a LA phonon, i.e. a lattice vibration as illustrated in the right of Fig. 4.3(a). This gives rise to the broadband enhancement even at T$=$ 10 K, since it does not depend solely on the thermal occupation of the phononic modes. At around $\hbar\Delta = 2$ meV the data points at higher temperatures show an increase in the decay rate although detuning is increased slightly. This occurs because the thermal occupation of the phononic modes gives rise to stimulated emission of a phonon, and this is also expected from theory. For negative detunings the QD relies on the absorption of phonons, that are sparse at low temperatures, and as a result the QD primarily decays through leaky radiation modes, as indicated in the left of Fig. 4.3(a). In the following we will discuss how we have calculated the decay rates from the LA phonon model.

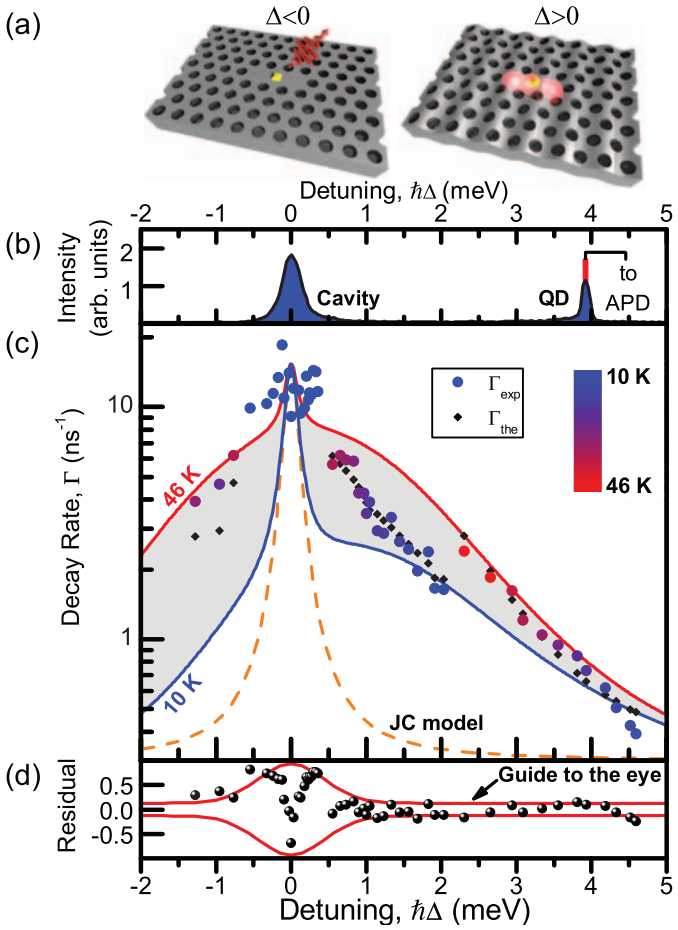

Figure 4.3: **a)** Illustration of the physical mechanism behind the phonon-enhanced Purcell effect. For negative (positive) detuning, the QD (yellow point) can decay into the cavity by absorbing (emitting) a phonon. At T = 0 K no phonon absorbtion is possible and residual spontaneous emission (red wavepacket) will dominate for negative detunings. **b)** Emission spectrum with the indication of the spectral range detected by the APD. **c)** Measured decay rate (Γ_{exp}) vs. detuning with the color specifying the experimental temperature. The theory is plotted for the highest and lowest experimental temperatures (solid curves) and also calculated at the detuning and temperature of the individual measurements (Γ_{the}) showing a very good agreement. **d)** Residuals $(\Gamma_{\mathrm{exp}} - \Gamma_{\mathrm{the}})/\Gamma_{\mathrm{exp}}$ with a guide to the eye at ± 0.13 for detuned conditions.

4.3 Extracting the effective phonon density of states

Having determined the parameters κ, γ, and g independently we can extract the effective phonon density by rearranging Eq. (4.6) to give

$$\Phi(\Omega = \Delta_{\mathrm{exp}}, \mathrm{T}_{\mathrm{exp}}) = \hbar^2 \gamma_{\mathrm{tot}} \left[\frac{(\Gamma_{\mathrm{exp}} - \gamma)(\gamma_{\mathrm{tot}}^2 + \Delta_{\mathrm{exp}}^2)}{2g^2 \gamma_{\mathrm{tot}}} - 1 \right] , \tag{4.8}$$

where Γ_{exp} is the measured decay rate at a given detuning Δ_{exp} and temperature $\mathrm{T}_{\mathrm{exp}}$. We have done this for all the measured decay rates and in Fig. 4.4(a) the extracted effective phonon density is shown. As the decay rates, this quantity also has a temperature dependence and the color of each data point corresponds to the temperature at which it was recorded.

Due to the linear dispersion of LA phonons, the effective phonon density vanishes at zero phonon energy. The effective phonon density depends on the thermal occupation of the phonon modes, i.e. temperature, which varies across the data set, but we can compensate for the effect of temperature. Following the definition in Eq. (4.7), the effective phonon density goes as n on the negative energy side, while it goes as $(n+1)$ on the positive side. By multiplying with the inverse, i.e. n^{-1} and $(n+1)^{-1}$, on the negative and positive side, respectively, we can cancel out the temperature dependence. This can alternatively be written as $\Phi(\Omega = \Delta) \cdot \mathrm{sgn}(\Omega)(1 - \mathrm{e}^{-\hbar\Omega/k_B T})$, which is the effective phonon density of states (DOS) that for a given detuning tells how many phononic states are available to assist in an optical transition into the cavity mode. The eff. phonon DOS extracted from experiment is shown in Fig. 4.4(b). The observed energy dependence of the eff. phonon DOS is a direct signature of the non-Markovianity of the phonon reservoir, since it would be a flat line in the case of a Markovian reservoir. We note that the eff. phonon DOS is a general concept, where no assumptions on the nature of the phonons have been made, and, e.g., localized phononic modes would give rise to sharp peaks at their resonance frequencies. The eff. phonon DOS is low for small phonon energies and grows rapidly with energy, reaching a maximum at about 3 meV before rapidly decreasing. This energy cutoff originates from the phonon wavelength (of about 7 nm) becoming comparable in size to the wavefunctions of the exciton confined in the QD [114], which makes the overlap integral between

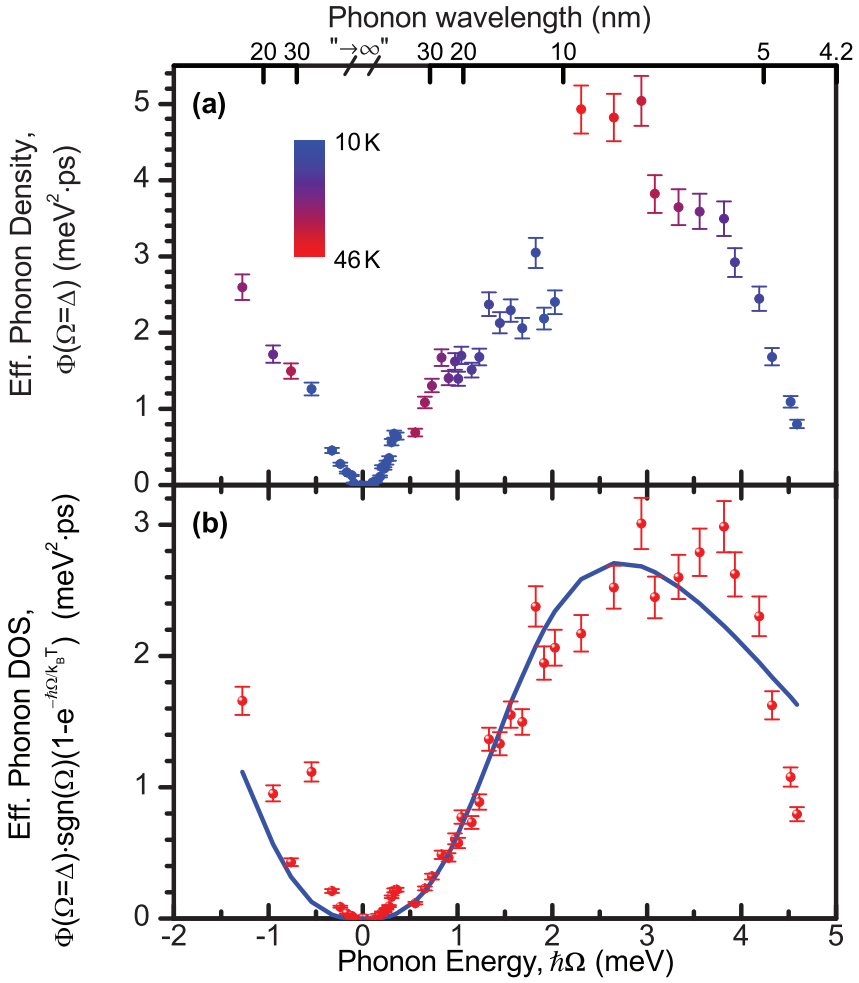

Figure 4.4: **a)** The effective phonon density extracted from the data in Fig. 4.3(c) using Eq. (4.8). The color scale indicates the experimental temperature at each data point and the upper axis indicates the corresponding phonon wavelengths. **b)** The effective phonon density of states (DOS) extracted from **(a)** by canceling out the temperature dependence. A cutoff is observed at large phonon energies (short wavelengths), and the solid blue curve shows the corresponding theory assuming bulk LA phonons in GaAs.

the exciton wavefunctions and the phonon mode vanish and thus the electron-phonon coupling strength go to zero. Consequently, a larger spatial extent of the QD corresponds to a smaller extent in k-space, and it therefore couples to fewer phonon modes. Though difficult with current technology, this does imply that tailoring the QD size may be employed for influencing phonon-dephasing processes.

4.4 Modeling with bulk phonons

We will now derive the eff. phonon DOS assuming that the QD is interacting with bulk phonons and compare this theory to the experimental data in Fig. 4.4(b). When assuming bulk phonons, we can expand them in terms of plane waves. This allows us to express the electron-phonon coupling strength for the kth phonon mode as

$$M^k = \sqrt{\frac{\hbar k}{2dc_l V}} \left(D_e \int d\mathbf{r} |\psi_e(\mathbf{r})|^2 e^{-i\mathbf{k}\cdot\mathbf{r}} - D_g \int d\mathbf{r} |\psi_g(\mathbf{r})|^2 e^{-i\mathbf{k}\cdot\mathbf{r}} \right) \quad , \quad (4.9)$$

where $D_\mathrm{e} = -14.6$ eV and $D_\mathrm{g} = -4.8$ eV are the deformation potentials [112], $c_l = 5110\ \frac{\mathrm{m}}{\mathrm{s}}$ is the longitudinal speed of sound averaged over the three different crystal axes, $d = 5370\ \frac{\mathrm{kg}}{\mathrm{m}^3}$ is the density of GaAs, and V is the phonon quantization volume. The subscripts e and g denote the excited and ground state of the electron. The values for GaAs are used because bulk phonons are primarily located in the GaAs. The electron wavefunctions are assumed to be gaussians and symmetric in the xy-plane orthogonal to the growth direction, which allows us to express them as

$$\psi_\nu(\mathbf{r}) = \frac{1}{\pi^{3/4} l_{\nu,xy} l_{\nu,z}^{1/2}} e^{-(x^2+y^2)/2l_{\nu,xy}^2} e^{-z^2/2l_{\nu,z}^2} \quad , \quad (4.10)$$

where $\nu = \{\mathrm{e}, \mathrm{g}\}$, and $l_{\nu,xy}$ and $l_{\nu,z}$ are the widths. Inserting these wavefunctions into Eq. (4.9) gives the following expression for the effective phonon density assuming bulk phonons [55]

$$\Phi(\Omega, \mathrm{T}) = \frac{\hbar}{4\pi d c_l^5} \frac{\Omega^3}{1 - e^{-\hbar\Omega/k_\mathrm{B}T}} \int_0^1 du \left(D_\mathrm{e} e^{\tilde{\Omega}_{e,\mathrm{xy}}^2 (u^2-1) - \tilde{\Omega}_{e,z}^2 u^2} - D_\mathrm{g} e^{\tilde{\Omega}_{g,\mathrm{xy}}^2 (u^2-1) - \tilde{\Omega}_{g,z}^2 u^2} \right)^2 \quad , \quad (4.11)$$

where $\tilde{\Omega}_{\nu,\mu} = \frac{\Omega l_{\nu,\mu}}{2c_l}$ and $\mu = \{\mathrm{xy}, \mathrm{z}\}$. From this expression it is evident that the multiplication with $\mathrm{sgn}(\Omega)(1 - \mathrm{e}^{-\hbar\Omega/k_B T})$ cancels out the temperature dependence and ensures positivity of the function. From Eq. (4.11) we see that the phonon density depends on the integral over the excited and ground state wavefunctions of the electron weighed by their respective deformation potentials, but importantly it also depends on the overlap between the excited and ground state wavefunctions. In Fig. 4.4(b) we have modeled the data with the function $\Phi(\Omega, \mathrm{T}) \cdot \mathrm{sgn}(\Omega)(1 - \mathrm{e}^{-\hbar\Omega/k_B T})$, where $\Phi(\Omega, \mathrm{T})$ is given by Eq. (4.11). The free parameters in the fit are the widths of the excited ($l_{\mathrm{e,xy}}$ and $l_{\mathrm{e,z}}$) and ground ($l_{\mathrm{g,xy}}$ and $l_{\mathrm{g,z}}$) state wavefunctions of the electron and an overall amplitude of the function. We further impose the restriction that the heights of the wavefunctions must be smaller than the widths, i.e. $l_{\mathrm{e,xy}} > l_{\mathrm{e,z}}$. A remarkable good agreement between the experimental data and the model for bulk phonons is found in Fig. 4.4(b), where the theory captures the essential features of growth at small phonon energies until reaching the phonon cut-off at around 3 meV and rapidly decreasing. We obtain the following realistic widths of the electron wavefunctions; $l_{\mathrm{e,xy}} = 3.4$ nm, $l_{\mathrm{e,z}} = 1.4$ nm, $l_{\mathrm{g,xy}} = 3.9$ nm, and $l_{\mathrm{g,z}} = 2.3$ nm. We show the model with the above sizes to be in excellent agreement with the data, but because the four parameters for the sizes of the wavefunctions do not have drastically different influences on the theory curve, there may be other combinations of sizes in the vast parameter space that give equally good agreements. Using these sizes we can, however, perform an important consistency check by computing the oscillator strength to be 15.5, which is in very good agreement with previous measurements on the same QDs that showed an oscillator strength of ~ 13.3 [28]. In Fig. 4.4(b) we observe the phonon cut-off, where the eff. phonon DOS decreases when the phonon wavelength is around 7 nm and it has reduced significantly at 4.5 nm, when the phonon wavelength is almost equal to the size of the electron wavefunctions.

The remarkable success of the bulk-phonon theory excludes effects of localization of phonon modes in the cavity. Phonon localization in an L3 photonic-crystal cavity has been reported at energies up to 4.1 μeV [104], while the typical phonon energies required for the phonon-assisted optical recombinations are above 0.5 meV. The corresponding phonon wavelengths are 42 nm and below, which is much smaller than the cavity dimensions, and thus ex-

plains the success of the bulk-phonon theory. We note that localized phonons could play a role for the minor deviations from theory observed at small phonon energies, but in this region the effect of multiexcitons is also expected to be pronounced. In addition to the four size parameters, the only other free parameter in the fit in Fig. 4.4(b) is the overall amplitude, for which we obtain the value 5.56. This corresponds to dividing the speed of sound in Eq. (4.11) by 1.41. Since the speed of sound is anisotropic in GaAs, which we have not explicitly accounted for in the theory, the overall amplitude can partly be attributed to this anisotropy. However, uncertainties in, e.g., the deformation potential may also contribute to the overall amplitude. For large detunings the quantity $\hbar^{-2}\Phi(\Delta \gg 0, \mathrm{T})$ enters in the theory as an effective pure-dephasing rate, but its value is typically 3 orders of magnitude larger than dephasing rates extracted when interpreting experiments with a Markovian model [115], which stresses the importance of accounting for the microscopic non-Markovian dephasing processes.

4.5 Comparison with other cavities

The broadband Purcell enhancement of the decay rate observed in the L3 photonic-crystal cavity was curiously not observed for the micropillar cavity, as discussed in section 3.1.3, despite comparable parameters. In order to explain the origin of this difference we experimentally study another type of cavity, namely an Anderson-localized (AL) cavity formed due to disorder in a photonic-crystal waveguide. The sample is displayed in the inset of Fig. 4.5 with the y-component of the simulated electric field overlayed the SEM image. In the sample, random cavities are generated by randomly perturbing the hole positions in the three rows of holes on each side of the waveguide with a standard deviation of 3% of the lattice parameter a. The Anderson-localized nature of the cavities together with cavity QED effects in this sample was previously demonstrated [116]. In Fig. 4.5 we present detuning-dependent measurements of the decay rate of a single QD close to resonance with an AL cavity. We observe no broadband Purcell enhancement, and the detuning dependence is well described by the Markovian Jaynes-Cummings model, despite the fact that the measured coupling strength and Q-factor of the AL and L3 cavities do not differ significantly. Thus we find $\hbar\kappa_{\mathrm{AL}} = 230 \pm 12$ μeV

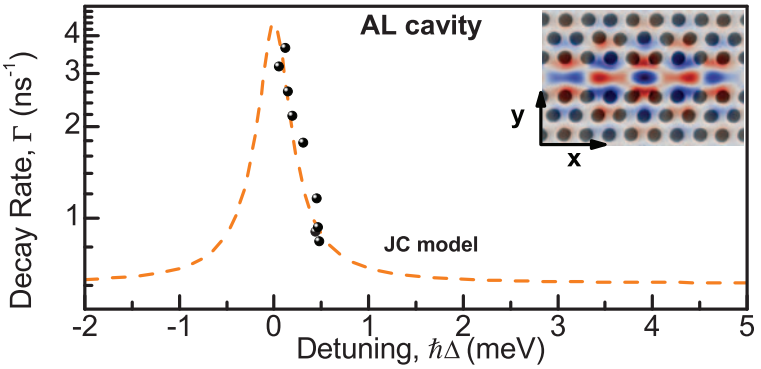

Figure 4.5: Detuning-dependent decay rate of a single QD close to resonance with an AL cavity. There is no broadband Purcell enhancement, and the data are well described by the Markovian JC model. Inset shows a SEM image of the sample, where the y-component of the simulated electric field is overlayed.

($Q = 5700 \pm 288$) and $\hbar g_{\mathrm{AL}} = 13.3$ μeV for the AL cavity, which should be compared to $\hbar\kappa = 195 \pm 1$ μeV and $\hbar g = 22 \pm 0.7$ μeV for the L3 cavity. As we demonstrate in the following, a crucial difference between the two cavities stems from the different background decay rates that we determine to $\hbar\gamma_{\mathrm{AL}} = 0.4$ μeV and $\hbar\gamma = 0.2$ μeV for the AL and L3 cavities respectively.

The difference between AL and micropillar cavities on the one hand and L3 photonic-crystal cavities on the other can be explained from Eq. (4.6). The Purcell enhancement factor Γ/γ is plotted in Fig. 4.6 for the three different cavities using the same effective phonon density and with the remaining parameters determined from experimental data. We find that the background decay rate γ plays a decisive role in determining the visibility of the broadband Purcell enhancement originating from phonon processes. The rate γ varies significantly for the different cavity geometries. The insets in Fig. 4.6 show sketches of the LDOS for the L3 and AL cavities highlighting that while the former appear in the bandgap, where the optical decay rate is strongly suppressed [28], AL cavities appear as random resonances on top of a background LDOS representing the waveguide mode [116], which gives rise to an emission channel. Similarly, the coupling to radiation modes is not strongly suppressed

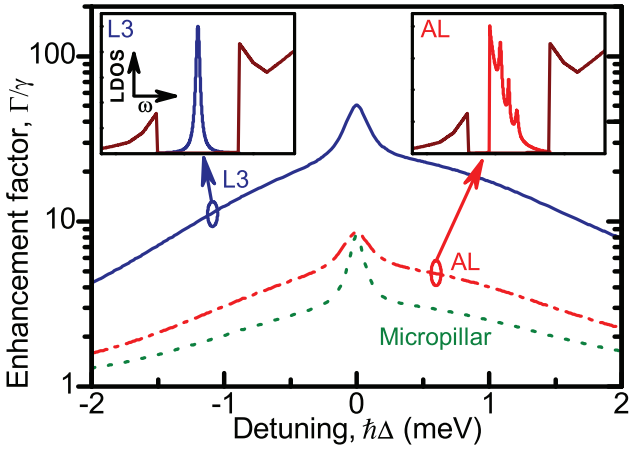

Figure 4.6: Calculation of the enhancement factor for the L3 photonic-crystal cavity, AL cavity, and micropillar cavity at T = 30 K. The parameters extracted from experiment are used and the same eff. phonon DOS extracted from the L3 cavity is used for all three cavities. Although g is almost identical for the L3 and micropillar cavity a huge difference in enhancement is seen due to background decay rate γ. Insets show sketches of the optical LDOS for the L3 and AL cavities.

in micropillar cavities, as the LDOS sketch in Fig. 3.1 indicates.

From Eq. (4.6) we deduce that two requirements need to be fulfilled in order to see broadband Purcell enhancement: $\frac{\Phi(\Delta)}{\hbar^2\gamma_{\mathrm{tot}}} \geq 1$ and $\frac{2g^2}{\hbar^2\gamma}\frac{\Phi(\delta)}{\Delta^2} \geq 1$. The former weak requirement is for a cavity with $Q = 6690$, as the L3 cavity, fulfilled for detunings above 0.5 meV, while the latter and stronger requirement can be evaluated to $\frac{2g^2}{\gamma} \times (0.6\ \mathrm{ps}) = 4.47 \geq 1$ for a typical detuning of 2 meV. This value evaluated for the L3 cavity is 5.5 and 6.1 times larger than that for the AL and micropillar cavities respectively, thus explaining the observed differences between the cavities.

4.6 Conclusion

We have observed the broadband Purcell enhancement for a QD in a photonic-crystal cavity. While the inability of the Jaynes-Cummings model to describe

the experiment was evident, we successfully modeled the data with a microscopic theory taking the non-Markovian interaction with LA phonons into account. Using this theory we have recorded the effective phonon density of states, which was made possible by the nanocavity that increased the sensitivity to phonon dephasing processes. The effective phonon density of states describes all the dephasing processes of the QD, and from it we have been able to extract the size of the exciton wavefunctions. We performed an important consistency check by computing the oscillator strength and comparing it to previous measurements on the same QDs, which showed a very good agreement. At short phonon wavelengths we observed a cutoff in the effective phonon density of states due to the phonon wavelength becoming comparable in size to the exciton wavefunctions, which results in the interaction matrix element vanishing. Remarkably, the measured effective phonon density of states is well described by a bulk phonon theory, despite the inhomogeneity of the photonic-crystal cavity. This was understood by considering the wavelength of the phonons relevant for the phonon-assisted transitions, where we noted that these are typically an order of magnitude smaller than the dimension of the cavity, thereby explaining the success of the bulk phonon theory. Localized phonon modes could still play a role for the minor deviations observed at small phonon energies, but multiexcitons are also expected to give significant contributions to the these deviations. Finally, we compared the broadband behavior in the L3 photonic-crystal cavity to an Anderson localized cavity in a photonic-crystal waveguide and the micropillar cavity studied previously. The broadband behavior is only observed in the L3 cavity and using the LA phonon theory we were able to show that a significant difference stems from the smaller background decay rate that is crucial for the visibility of the phonon-assisted processes.

Chapter 5

Efficient generation of indistinguishable photons using phonon-mediated excitation

Single photons are the basis of optical quantum computing, and they must be generated on-demand in a specific optical mode. On-demand implies that every excitation event must lead to the emission of a single photon and into a specific optical mode means that every emitted photon must be collected by, e.g., the microscope objective. For quantum cryptography applications, optical losses can be corrected for and the requirement can be relaxed to the generation of a single or no photon on-demand. One way of obtaining single photons is to use heralded single photons from a parametric down-conversion process in a crystal, where a single photon of the pump field is converted into two photons. These two photons have half the frequency of the incoming photon, and they are emitted in two different optical modes. Detection of a photon in one of the modes implies that there is a single photon in the other mode. Heralded sources are, however, not on-demand but rather probabilistic, and scaling these systems for quantum computing is difficult. One of the most impressive demonstrations of on-demand generation of single photons has been done using molecules as

emitters, where a collection efficiency of 96% has been reached [117]. Some of the most efficient semiconductor solid-state single-photon sources include nanowires and micropillar cavities, where collection efficiencies at the first lens of 72% [118] and 79% [33], respectively, have been demonstrated.

Implementation of quantum computing using linear optics imposes the additional and very strong requirement that the single photons generated on-demand in a specific optical mode must be indistinguishable from each other [6]. Recent work has demonstrated that high degrees of indistinguishability can be achieved by tailoring the nanophotonic structure [33] and by resonantly exciting the QD [119].

Reducing decoherence processes in quantum dots is therefore of high importance for the utilization of QDs for quantum-information processing, since dephasing reduces the indistinguishability. Usually the dephasing of the emitter is attributed to spectral diffusion and the interaction with phonons. Spectral diffusion is the consequence of Coulomb shifts of the QD transition due to the interaction with free or trapped carriers outside the QD, i.e. fluctuations of the electrostatic environment. Although these processes are expected to be on a timescale much slower than the nanosecond timescale of the QD dynamics, recent work has indicated that rapid changes in the electrostatic environment may be responsible for the decrease in indistinguishability [33]. In the last chapter we saw how the interaction between the exciton in the QD and LA phonons can alter the dynamics of the QD significantly. The same interaction gives rise to dephasing of just the QD transition on the very short picosecond timescale compared to the nanosecond timescale of the dynamics. This dephases the QD and consequently degrades the degree of indistinguishability.

In this chapter we study a QD in an L3 photonic-crystal cavity that acts as a highly efficient single-photon source. We demonstrate that the high collection efficiency is a broadband feature and does not depend strongly on the coupling of the QD to the cavity mode. Numerical simulations of the emission from the QD have been performed in order to understand the high collection efficiency, but the agreement was found to be poor, and we discuss the possible reasons for this. We demonstrate selective phonon-mediated excitation of the QD by the absorption of either LA phonons or two longitudinal optical (LO) phonons.

In particular, using LO phonons we can selectively excite the exciton or biexciton 7 times more efficient than under above-band excitation. Under LO and

LA phonon-mediated excitation we perform indistinguishability measurements using a Hong-Ou-Mandel interferometer, which show modest indistinguishabilities due to the inhibited rate of spontaneous emission. The corresponding dephasing rates are, however, very low and we demonstrate a decrease in dephasing when shifting from LO to LA phonon-mediated excitation. This chapter is based on the article "*Efficient generation of indistinguishable photons using phonon-mediated excitation of a quantum dot in a photonic-crystal cavity*" by K. H. Madsen, S. Ates, J. Liu, A. Javadi, and P. Lodahl, which is being prepared for submission.

5.1 Single-photon collection efficiency

The photonic-crystal cavity sample has a lattice constant $a = 240$ nm and hole radius $r = 66$ nm. The experimental setup is the same as described in the previous chapter, where we probe the cavity by confocal microscopy and a dichroic mirror separates the excitation from the emission. We use a tunable Ti:Sapph laser for continuous wave (CW) or pulsed (3 ps pulse duration and 76 MHz repetition rate) excitation. For measurements of the efficiency, the collected emission is sent to a spectrometer through a free-space path in order to reduce the losses of the optical path. Although the excitation beam can be tightly focused on the sample to a spotsize of 2.4μm, the carriers generated in the GaAs can diffuse over typical lengths of $\sim$ 15μm, thus exciting other QDs. Spatial selection is therefore always needed to filter out these other contributions. This is done by sending the optical beam through a one-to-one telescope and inserting a pinhole in the image plane created between the two lenses. For autocorrelation and coherence measurements the emission is sent through a single-mode polarization-maintaining fiber. After the spectrometer, the emission is directed onto a CCD-camera or an avalanche photo detector (APD). In Fig. 5.1(a) the recorded cavity emission spectra under strong above-band (800 nm) CW excitation power is shown. The modes are labeled M1-M6, and because the QD ensemble only emits within the region $880 - 1000$ nm, the M6 mode is not visible, although its presence will be demonstrated in the following by scanning the excitation laser across its resonance. Most notably, the M3 mode is very intense despite being a low-Q mode.

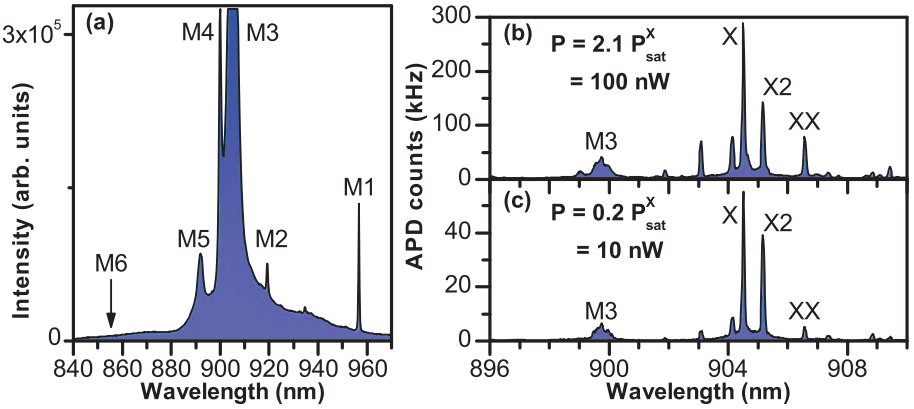

Figure 5.1: **a)** Cavity emission spectrum showing the modes labeled M1-M6 under strong above-band CW excitation. **b-c)** Emission spectra recorded on APD under pulsed M6-resonant excitation for excitation powers 2.1 and 0.2 times the saturation power of the exciton X-line, respectively. The neutral exciton (X), bi-exciton (XX), and charged exciton (X2) all originate from the same QD and are identified using cross-correlation measurements and power series.

5.1.1 Identification of emission lines

In Fig. 5.1(b-c) we show the spectra recorded on the APD around the M3 mode, where the pulsed excitation laser has been tuned into resonance with the M6 mode. The applied excitation powers are 2.1 and 0.2 times the saturation power of the X-line. For the high power we observe a very high count-rate on the APD of almost 300 kHz. The emission spectrum is also very clean, and even above saturation power the M3 mode has not increased in relative intensity. The neutral exciton (X) is identified by the linear power dependence shown in Fig. 5.3(a) and single-photon emission from this line is shown in Fig. 5.3(c), which we will discuss more shortly. The X-line is linearly polarized and under pulsed excitation we record the decay curve that is found to be bi-exponential with a fast rate of 0.62 ns^{-1} and a slow rate of 0.24 ns^{-1}. The bi-exponential behavior proves that it is a neutral exciton, since the slower exponential decay is due to the dark state, that does not exist for a charged exciton. We also note that the fast rate is inhibited compared to the bulk decay rate, where typical

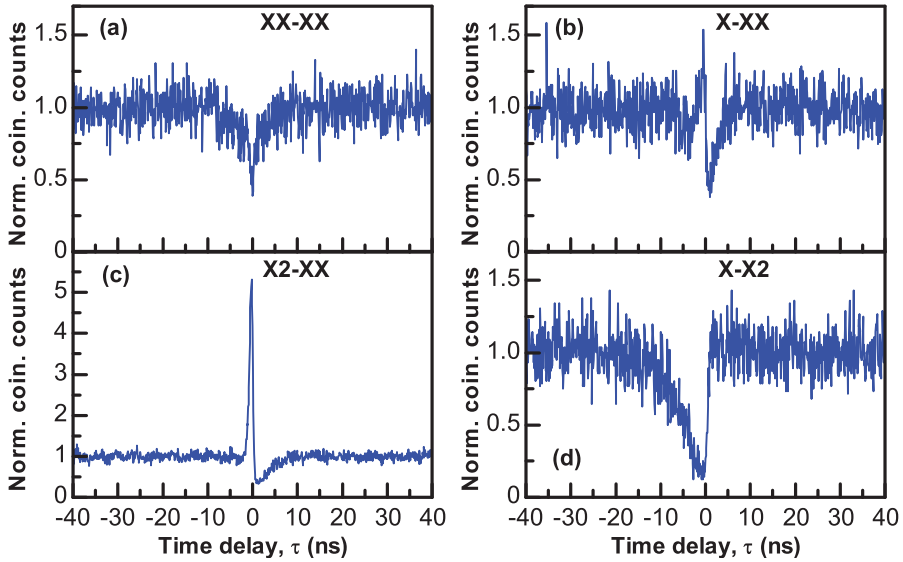

Figure 5.2: Normalized coincidence counts as a function of time delay under CW excitation. **a)** Autocorrelation measurement of the bi-excitonic XX-peak, where the anti-bunching reveals single-photon emission. **b)** Cross-correlation measurement where the time delay is measured from detection of an X photon and stopped when detecting an XX-photon. The bunching at negative times proves that the process is a cascaded emission and identifies the XX-peak as a bi-exciton. **c)** The same feature is observed for the X2-XX cross-correlation proving that the XX-peak also decays into the X2-peak. **d)** Cross-correlation proving that the X2 is a charged exciton.

fast decay rates of 1.1 ns^{-1} are found. The inhibition of the fast decay rate for the investigated QD is due to the suppression of spontaneous emission by the photonic-crystal structure. Because the background decay rate is strongly inhibited, the QD can couple to the cavity while still having a decay rate that is inhibited compared to the bulk decay rate. The bi-exciton (XX) is identified by its super-linear power dependence, which occurs because it can decay into both bright exciton states. In Fig. 5.2(a) we show an autocorrelation measurement of the XX-peak that exhibits anti-bunching, which is a proof of the single-photon emission from the bi-exciton. The raw data does not dip all the way to zero in part due to the convolution with the instrument response function,

i.e. the time-resolution of the APDs. The bi-excitonic nature of the XX-line is demonstrated in Fig. 5.2(b), where a cross-correlation between the X- and XX-line shows the expected behavior for a bi-exciton. The time-delay is measured from the detection of a photon in the X-peak and stopped when a photon is detected in the XX-peak. Thus when having detected a X-photon there is a reduced probability of detecting an XX-photon and a dip in the coincidence counts is observed, while the probability is enhanced for the opposite case. In Fig. 5.2(c) a cross-correlation between the X2- and XX-peak is shown and the same behavior is observed. This means that the bi-exciton (XX) has a cascaded decay into both the X and X2 exciton. From a power series we verify that the X2-line has a linear power dependence and in Fig. 5.2(d) we show the cross-correlation between the X- and X2-peaks. This measurement shows only anti-bunching which means that the X- and X2-lines originate from the same QD but the radiative decay of X2 does not populate X and vice versa. The asymmetry of the dip with a fast recovery for $\tau > 0$ is expected if the X2 arises from a charged exciton. The post-measurement state of charged-exciton emission is a single-charged QD, and the recovery time for $\tau > 0$ is thus determined by the timescale of injection of a single charge into the QD. The recovery time for $\tau < 0$ is determined by the timescale of injection of three charges [120], which is expected to be much slower and thus gives rise to the strong asymmetry observed in Fig. 5.2(d). We thus conclude that the X2-line originates from a charged exciton in the same QD.

5.1.2 Calculating the collection efficiency

We send the emission from the neutral exciton (X) to an APD and perform the power series shown in Fig. 5.3(a), where the very high count-rates on the APD bear evidence of the high collection efficiency. The corresponding very clean spectra at two different excitation powers were shown in Fig. 5.1(b-c). We fit the power series with the function $C_{\mathrm{out}} = C_{\mathrm{sat}}(1 - \mathrm{e}^{-P_{\mathrm{in}}/P_{\mathrm{sat}}})$, where P_{in} and P_{sat} are the input power and input saturation power, respectively, and C_{out} and C_{sat} are the corresponding output count-rates. Modeling of the power series is shown as solid lines in Fig. 5.3(a) together with the data, and we extract the parameters $P^X_{\mathrm{sat}} = 46.7 \pm 3.7$ nW and $C^X_{\mathrm{sat}} = (2.93 \pm 0.086) \cdot 10^5$ counts s^{-1} for the single X-line.

In Fig. 5.3(c) autocorrelation measurements of the X-line are shown for

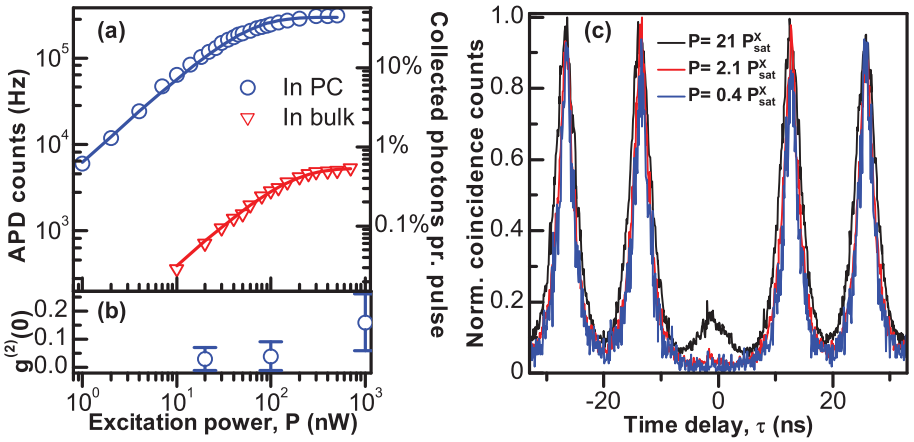

Figure 5.3: **a)** Power series of the X-line and of a QD in bulk recorded on the APD under pulsed (76 MHz) excitation showing a 56 times increase in count-rate for the X-line. Solid lines are the fits, and on the right axis the corresponding efficiency at the first lens is plotted. **b)** The values of the second-order correlation function $g^{(2)}(\tau = 0)$ extracted from **(c)**, where we present auto-correlation measurements of the neutral exciton (X) under three different excitation powers showing a pronounced anti-bunching even at excitation powers 21 times the saturation power.

three very different excitation powers. We calculate the value of normalized coincidence counts at zero time delay, $g^{(2)}(\tau = 0)$, by averaging all counts in a 2 ns window around zero delay, and we obtain the values 0.03 ± 0.04, 0.04 ± 0.05, and 0.16 ± 0.1 for excitation powers of 0.4, 2.1, and 21 times saturation power, respectively. These values are also shown in Fig. 5.3(b) and remarkably the anti-bunching remains very strong even at 21 times saturation power proving that the X-line contains single-photon emission.

A power series on a QD situated in bulk GaAs is also shown in Fig. 5.3(a). By fitting the data we obtain the parameters $P_{\text{sat}}^{\text{bulk}} = 126.7 \pm 6.3$ nW and $C_{\text{sat}}^{\text{bulk}} = (5.22 \pm 0.10) \cdot 10^3$ counts s^{-1}. Power series have been measured on several QDs in bulk and the one presented here is the one giving the highest count-rate. The X-line in the photonic-crystal cavity still gives 56 times more counts than the bulk QD. In order to determine the collection efficiency of the X-line we need a calibration value. For this purpose we calculate the

collection efficiency at the first lens of a bulk QD situated below an air-GaAs interface and for the experimentally used numerical aperture (N.A.) of 0.6. Using the finite-element method the far-field pattern of a dipole in a homogenous medium is calculated, but more details on the simulations will be provided later. In order to take the air-GaAs interface into account, Fresnel equations for the refraction of a wave at the air-GaAs interface are used to calculate the energy profile in air. The intensity that falls within a ring given by N.A. = 0.6 is integrated and divided by the total intensity, which gives a collection efficiency of $\eta_{\mathrm{bulk}} = 0.79\%$ for a bulk QD. Very similar values for the collection efficiency are obtained in [118], where the value is calculated using an eigenmode expansion technique.

The bulk count-rate above saturation can be expressed as

$$C_{\mathrm{sat}}^{\mathrm{bulk}} = \eta_{\mathrm{setup}}\, \eta_{\mathrm{bulk}}\, \mathrm{r}_{\mathrm{rep}} \quad , \tag{5.1}$$

where η_{setup} is the transmission of the setup from the output of the microscope objective to detection, η_{bulk} is the collection efficiency at the first lens, and $\mathrm{r}_{\mathrm{rep}}$ is the repetition rate of photon emission from the exciton in the QD. Importantly this expression is only valid for excitation powers above saturation, because in order to guarantee that only the two orthogonal dipoles in the QD and no dark states are excited, a bi-exciton has to be created for every excitation event. One might expect the rate of photon emission, $\mathrm{r}_{\mathrm{rep}}$, to be given by the laser repetition rate (76 MHz) but for several reason this is not correct. Firstly, at saturation both orthogonal dipoles of the QD are excited with equal probability, so division by a factor of two is necessary. Secondly the non-unity quantum efficiency of the exciton means that it sometimes recombines non-radiatively, which would reduce the rate even further. Finally, other charges in the GaAs can get trapped close to the QD and shift the frequency of the exciton far away. The exciton returns to its normal frequency when this trapped charge has disappeared again, and this gives rise to blinking of the QD, which has been observed previously in cavity quantum electrodynamics [93, 66], and will reduce $\mathrm{r}_{\mathrm{rep}}$ even further. Blinking will be studied in more detail shortly. For the derivation of the collection efficiency we make the important assumption that $\mathrm{r}_{\mathrm{rep}}$ is the same for the QD in the cavity and the QD in bulk. With this assumption we can divide Eq. (5.1) for the QD in the cavity with the one for

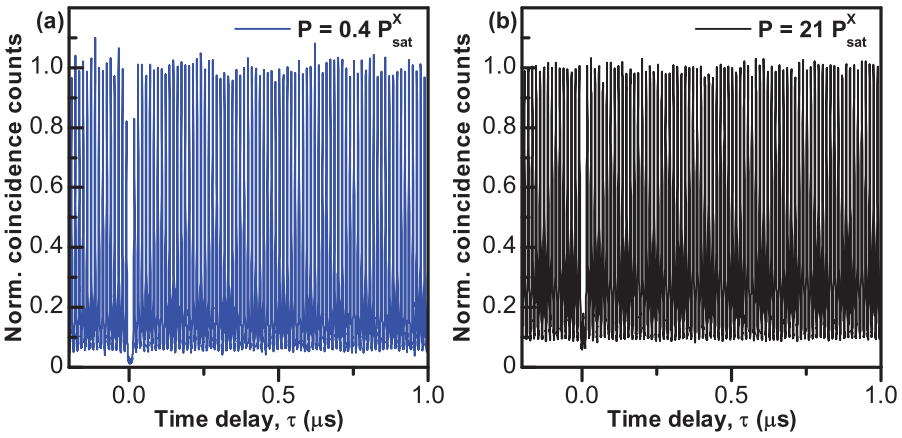

Figure 5.4: Normalized coincidence counts at large delay times. Both at low **(a)** and high **(b)** power we found no systematic variations of the peak heights, which is otherwise a tell-tale sign of blinking of the QD. The standard deviations of the peak heights are $\pm 2.5\%$ and $\pm 1.6\%$ for low and high power, respectively.

the bulk QD and we obtain the following collection efficiency

$$\eta_X = \eta_{\text{bulk}} \frac{C^X_{\text{sat}}}{C^{\text{bulk}}_{\text{sat}}} = (44.3 \pm 2.1)\% \quad . \tag{5.2}$$

This collection efficiency should be compared to the best found in the literature, where 72% [118] and 42% [121] for nanowires and 79% [33] for micropillars have been demonstrated. Just considering the APD detection frequency of single photons, we measure 293 kHz compared to $\sim$ 65 kHz [118], $\sim$ 236 kHz [121], and $\sim$ 700 kHz [33] for the three former cases found in the literature.

Blinking of the QD can usually be observed as variations of the peak amplitude at large time delays in autocorrelation measurements. In Fig. 5.4(a-b) we plot the low, 0.4 $\text{P}^{\text{X}}_{\text{sat}}$, and high, 21 $\text{P}^{\text{X}}_{\text{sat}}$, power autocorrelation measurements from Fig. 5.3(c) at large time delays. Both at low and high power we observe no systematic variations in the peak heights and the standard deviation of the peaks heights are $\pm 2.5\%$ and $\pm 1.6\%$ for the low and high power measurements, respectively. Larger delays were also investigated, but no systematic variations were found, and we conclude that blinking of the QD is negligible on the timescales investigated. Unfortunately we could not perform the same

autocorrelation measurements on the emission from the bulk QD due to low count-rates.

The efficiency at the first lens has been measured for many QDs all spectrally situated around the M3 mode, and the high efficiency is seen to be reproducible and relatively broadband. We found 8 QDs with efficiencies above 20% out of which 5 QDs had efficiencies above 25% and for some of the QDs the detuning exceeded 5 nm. The corresponding decay rates have also been recorded showing, as expected, a strong frequency dependence of the Purcell enhancement of the decay rate with Purcell factors up to ~ 6 close to resonance with the M3 mode. In addition, no strong correlation was found between the high collection efficiency and the Purcell enhancement, which confirms that the high efficiency is not due to the Purcell enhancement but rather to the modification of the far-field radiation pattern resulting from the cavity structure.

5.2 Numerical modeling of the efficiency

The high efficiency has also been investigated theoretically by performing numerical simulations of the emission from a QD with various detunings from the M3 mode. The simulations are done in the commercially available software COMSOL using the finite-element method in frequency domain. We calculate the electric field from the dipole on a surface 10 nm above the membrane and perform a near-field to far-field transformation over the surface [1] [122, 123]. The far-field patterns are calculated for the two orthogonal dipole moments of the QD oriented along the x- and y-axis, and the energy falling within a N.A.$= 0.6$, corresponding to our microscope objective, in the upward direction compared to the total emitted energy gives the collection efficiency. The experimental situation is illustrated in Fig. 5.5(a), from which it is clear that the symmetry of the membrane results in identical emission patterns in the up- and downward directions. Figure 5.5(b) shows examples of the far-field patterns for the x- and y-dipoles, where the norms of the x- and y-components of the simulated electric fields are plotted.

The calculated collection efficiencies are shown in Fig. 5.5(d-e) as a function of detuning from the M3 mode for the x- and y-dipoles, respectively, and for the 6 different spatial positions that are shown in the position map in Fig. 5.5(c).

[1] Simulations have been performed by Alisa Javadi, Niels Bohr Institute

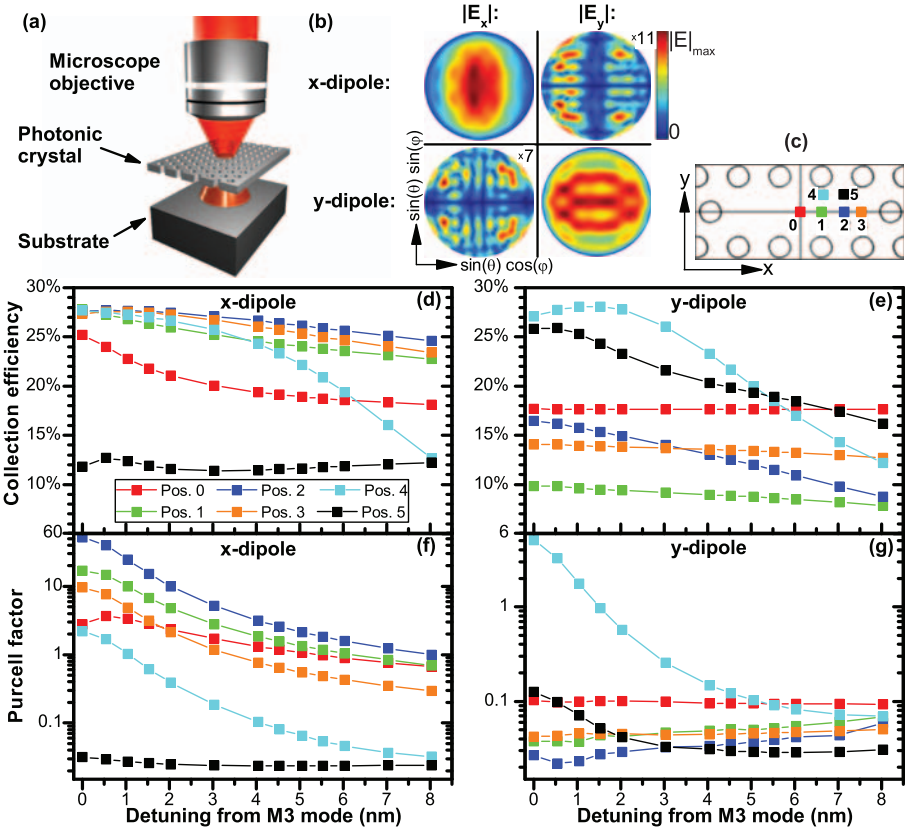

Figure 5.5: **a)** Illustration of the experimental situation. **b)** Calculated far-fields showing the norms of the electric field components for the x- and y-dipoles at position 3 and detuning 5 nm in spherical coordinates with the polar (θ) and azimuthal (φ) angles. There is almost no mixing of the polarizations in the far-field. **c)** Position map for the cavity. **d-e)** Calculated collection efficiencies at the first lens for a N.A.= 0.6 as a function of detuning at 6 different spatial positions for the x- and y-dipoles, respectively. **f-g)** The corresponding Purcell factors show a small coupling to the M3 mode for many positions at large detunings. There is no strong correlation between Purcell factors and collection efficiencies.

The x-dipole is generally the most efficient, while both dipoles exhibit a broad-band high efficiency, none of which, however, is as high as the experimentally

measured value. We also calculate the corresponding Purcell factors for the two dipoles in order to gain insight on the degree of coupling to the M3 mode, and the results are shown in Fig. 5.5(f-g). The x-dipoles are generally Purcell enhanced, while the y-dipoles have an inhibited spontaneous emission rate. For larger detunings, the Purcell factor decreases significantly while the efficiencies remain high, thus showing no strong correlation between Purcell factor and efficiency. This proves that it is not the coupling to the M3 mode but rather the modification of the far-field pattern due to the cavity structure that is responsible for the high efficiency.

As an example, position 3 exhibits the broadband high efficiency and low Purcell factors that we measure experimentally. The far-fields plots in Fig. 5.5(b) are for the two dipoles at position 3 and detuning 5 nm. For the x-dipole, $|\mathrm{E_y}|$ is scaled up by a factor of 11 for the structure to be visible on the same scale as $|\mathrm{E_x}|$. Similarly $|\mathrm{E_x}|$ is scaled up by a factor of 7 for the y-dipole, and we immediately observe that the x- and y-dipoles emit almost exclusively into the x- and y-polarizations, respectively. This means that there is no mixing of the polarizations in the far-field at position 3. This result is important because mixing of the polarizations can result in errors in the calculations of the efficiency, because it leads to underestimates of $\mathrm{r_{rep}}$. For the same detuning of 5 nm we do, however, observe polarization mixing for position 4, where both dipoles emit into the x-polarization in the far-field. We attribute this mixing to the fact that the y-dipole at position 4 is also coupled to the M3 mode, as evidenced by the detuning-dependence of the Purcell factor. The M3 mode is x-polarized in the far-field, and since the y-dipole couples to the M3 mode this obviously leads to polarization mixing. We note that the measurements reveal that the exciton is highly polarized, which indicates that there might be polarization mixing in the far-field.

The calculated efficiencies are, however, systematically lower than the experimentally measured value. The most likely explanation for this discrepancy is that we do not take the under-etch of the membrane into account. Underneath the membrane there is a air gap of 1530 nm before the GaAs substrate is reached, cf. Fig. 5.5(a). This distance is large enough for near-field effects to have died out [123], but the air-GaAs interface will give rise to reflections. For reference, for a plane wave at normal incidence $\sim 55\%$ of the power is reflected. Furthermore, the light reflected from the substrate can interfere con-

structively with the top-emitted field. This could very well be the reason for the discrepancy between the calculated and measured values for the efficiency.

5.3 Phonon-mediated excitation

We now turn to studying different excitation schemes of the QD in order to address the QD of interest in the cavity. While resonant excitation provides the ultimate selective excitation method [92, 66], it is technically very demanding as shown in the next chapter. We previously showed that p-shell and higher-order mode excitation also provide relatively selective excitation. In the following we will demonstrate both LO and LA phonon-mediated excitation of the QD, which proves to be a selective excitation mechanism.

5.3.1 LO phonon-mediated excitation

In Fig. 5.6(a) we present photoluminescence excitation (PLE) measurements, where we detect the total intensity in the M1 mode while scanning the laser across the M6 mode, thus mapping out the absorption spectrum. By scanning across the M6 mode under high excitation power we map the linewidth of the M6 mode and record a Q-factor of 306. Thereafter we again scan the excitation laser across the M6 mode but now under low excitation power, while we record the total intensity of the exciton X. We observe two strong absorption resonances at 854.56 and 856.40 nm and the corresponding emission spectra are shown in Fig. 5.6(b-c), respectively, both showing very clean emission spectra. In Fig. 5.6(a) we also plot the total intensity of the bi-exciton XX as a function of excitation wavelength, where we observe a single strong resonance at 856.40 nm.

When exciting through the 854.56 nm resonance, the emission spectrum is completely dominated by the excitonic X-line, cf. Fig. 5.6(b), while the bi-excitonic XX-line increases by a factor of ~ 3 when exciting through the 856.40 nm resonance and keeping the excitation power constant. Furthermore, the energy difference between the absorption peaks at 854.56 and 856.40 is 3.12 meV, which exactly matches the energy difference between the X- and XX-emission lines. The resonances are too high in energy to be higher electronic states of the QD and the wetting layer does not give rise to sharp resonances. Furthermore, the fact that the PLE measurement in Fig. 5.6(a) maps out the

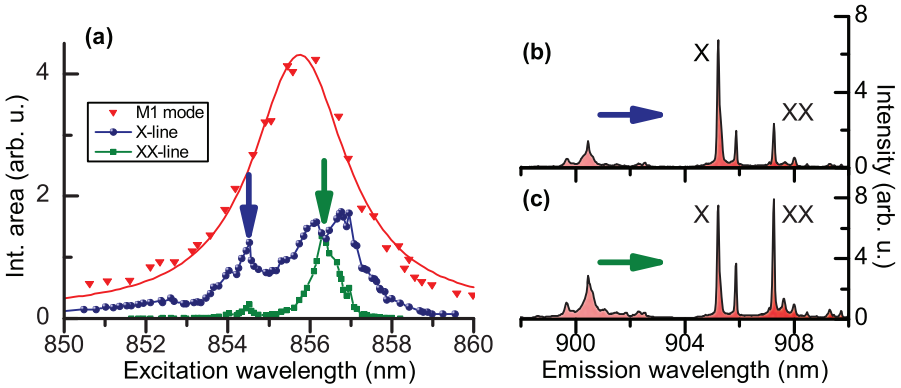

Figure 5.6: **a)** PLE measurement of the absorption showing the integrated area in the M1 mode (high power), in the exciton X-line (low power), and in the bi-exciton XX-line (low power) as a function of excitation wavelength around the M6 mode. The linewidth of the M6 mode is mapped when detecting the M1 mode and agrees well with the fit (solid red line). Detecting the X- and XX-lines reveal sharp resonances at 854.56 and 856.40 nm corresponding to LO phonon-mediated excitation of the exciton (X) and bi-exciton (XX), and the corresponding spectra are shown in **(b)** and **(c)**.

M6 linewidth while detecting the intensity in the M1 mode proves that the wetting layer is a continuum over the M6 linewidth. The energy difference between the excitation and emission is 81.2 meV, which roughly corresponds to two times the LO-phonon energy in GaAs as we will discuss shortly. We thus conclude that the resonances are due to the absorption of 2 LO phonons, where the lower and higher wavelength-resonances correspond to LO-phonon mediated excitation of the exciton and bi-exciton, respectively.

LO phonons are out of phase movements of the atoms in the lattice, which in the simple diatomic linear chain model can be understood as the two atoms within the unit cell moving in opposite direction, as opposed to acoustic phonons where the two atoms move in the same direction [21]. As opposed to LA-phonons that have a linear dispersion relation and thus form a continuum, the energy of an LO phonon is non-zero at zero phonon wavevector. The dispersion relation for LO phonons is almost constant at small wavevectors. As demonstrated in section 4.3, the QD only interacts with phonons up to a certain

wavevector because the finite size of the exciton wavefunctions gives rise to a cut-off [112]. For wavevectors below this cut-off, the LO phonon dispersion is constant, and we calculate the energy to be 36.8 meV [2]. This results in discrete lines of the LO phonon absorption spectrum, corresponding to multiples of the single LO phonon energy.

The calculated energy of a LO phonon in bulk GaAs is 36.8 meV, while we experimentally obtain the value 40.6 meV. Part of this discrepancy may be attributed to the calculated value containing the average of all LO mode frequencies [124]. Previous work has observed LO phonon energies increased by ~ 0.7 meV, where transmission spectra revealed that the shift in energy arose from the strong coupling between the p-shell of the QD and 2 LO-phonons [125]. However, in our QDs the p- to s-shell energy difference is typically ~ 28 meV. This means that the 2 LO-phonon resonance lies within the continuum of electronic states in the wetting layer, and the former mentioned effect has only been demonstrated when the 2 LO-phonons interact with a discrete p-shell level. One might speculate that the energy difference is emitted as LA phonons, but this would not give rise to a sharp but rather a broadband resonance. The reason for this discrepancy should most likely be found in the inhomogeneity and/or strain of the QD that could shift the frequency of the LO-phonons. Furthermore, because LO phonons can be considered microscopic distortions within the primitive cell of the semiconductor [126], phonon localization either in the QD or at the interface between the InAs and GaAs could maybe be responsible for this increase in energy. By keeping the excitation power constant, we observe that LO phonon mediated excitation is 7 times more efficient than above-band excitation. According to theoretical calculations[2] for a bulk QD, it should be 3 orders of magnitude more efficient to excite through the 1 LO-phonon line than the 2 LO-phonon line used here. However, experimentally we could not excite through the former because that absorption line does not lie within the linewidth of a cavity, which highlights the fact that the total absorption depends both on the optical properties of the photonic-crystal membrane as well as on the absorption spectrum of the material.

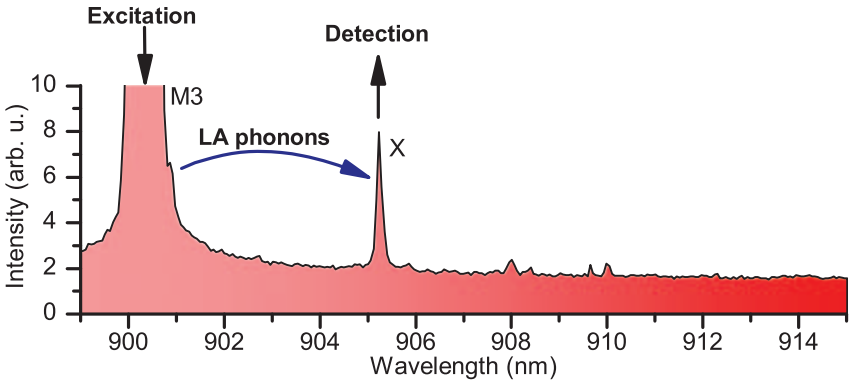

Figure 5.7: The excitation laser is resonant with the M3 mode, and LA-phonons mediate the excitation of the X-line. The peak at the M3 mode is due to laser reflections. The spectrum is surprisingly clean with only emission from the X-line, because excitation of the bi-exciton (XX) and charged exciton (X2) is highly unlikely.

5.3.2 LA phonon-mediated excitation

In Fig. 5.7 we demonstrate that we can also excite the QD by tuning the excitation laser into resonance with the M3 mode, which is only 4.8 nm blue detuned from the X-emission line. The large peak seen at the M3 wavelength is the laser reflection, which we could not suppress more. This excitation mechanism must be mediated by LA phonons since their linear dispersion results in a continuum of modes, and the excitation cannot be due to electronic states of the QD since they lie much higher in energy. Physically, the process starts with the absorption of a photon with the energy of the cavity that becomes an exciton in the QD with emission of the residual energy into the lattice as an LA phonon. This has been previously demonstrated [127], whereas in chapter 4 we demonstrated the opposite process, where the QD was initially excited and emitted an LA phonon in order to decay into the cavity [55]. Figure 5.7 shows a surprisingly clean spectrum, where only emission from the X-line is present. The bi-excitonic XX-line is most likely suppressed because it is detuned 3.12 meV further away from the excitation than the X-line, and because it requires absorbtion of an additional photon and the subsequent emission of one more

[2]Calculation performed by Per Kaer, DTU Fotonik

LA phonon, which is unlikely. The charged exciton (X2) is also absent from the spectrum in Fig. 5.7 because the process is highly unlikely. One additional charge is needed for a charged exciton and this cannot be created by phonon-mediated optical excitation.

5.4 Indistinguishability measurements

We now study the effect of the phonon-mediated excitation on the coherence of the single photons emitted from the QD, in order to gain more insight on the decoherence mechanisms that give rise to dephasing. The coherence is investigated by measuring the indistinguishability of two consecutively emitted photons in a Hong-Ou-Mandel (HOM) interferometer [88], where the two photons are interfered on a beam-splitter and their coincidence counts are measured as a function of delay time. If the two photons are completely distinguishable, then the two photons will neither bunch nor anti-bunch, whereas indistinguishable photons will bunch in one arm and thus not give rise to any coincidence counts. This is a purely quantum mechanical effect that does not appear in the classical description of the experiment [38]. In the following, the theoretical background will briefly be derived before discussing the experimental data.

5.4.1 Calculating the indistinguishability

For comparison to correlation measurements, we can to a good approximation describe the neutral exciton as a two-level system that decays exponentially. This can be done because the amplitude of the slow component is 29 times smaller than the amplitude of the fast component. The equations of motion are easily found from the master equation for the density matrix, as done in section 2.4. However, we do not need to include the coherent light-matter interaction since we are considering a QD that decays exponentially, and dissipation can therefore be included through Lindblad terms. In this way we introduce the decay rate γ and the pure dephasing rate γ_{dp} of the QD, and we obtain the following time-evolutions of the population and polarization, respectively:

$$\rho_{\mathrm{qd}}(t) = \mathrm{e}^{-\gamma t} \quad \text{and} \quad \rho_{\mathrm{po}}(t) = \mathrm{e}^{-(\gamma/2+\gamma_{\mathrm{dp}})t} \ . \tag{5.3}$$

The electric field annihilation operator, $\hat{a}$, can in the far-field be related to the QD lowering operator, $\hat{\sigma}_-$, with a time-retardation due to the propagation time

of the emitted photon and with a space dependent amplitude [49]. Neglecting both the amplitude and time-retardation allows us to express the unnormalized first-order coherence function as

$$G^{(1)}(t,\tau) = \langle \hat{\sigma}_+(t+\tau)\hat{\sigma}_-(t)\rangle = \mathrm{e}^{-(\gamma/2+\gamma_{\mathrm{dp}})\tau}\rho_{\mathrm{qd}}(t) = \mathrm{e}^{-(\gamma/2+\gamma_{\mathrm{dp}})\tau}\mathrm{e}^{-\gamma t}\ , \quad (5.4)$$

where the second equality sign has been obtained by use of the quantum regression theorem [38]. The photon annihilation operators $\hat{a}_3(t)$ and $\hat{a}_4(t)$ correspond to the two output ports of the beam-splitter, so experimentally we measure the coincidence counts between those two, which is given by the cross-correlation function $\langle \hat{a}_3^\dagger(t)\hat{a}_4^\dagger(t+\tau)\hat{a}_4(t+\tau)\hat{a}_3(t)\rangle$ [128]. Using the input-output relationship for the operators in the beam-splitter, the output operators $\hat{a}_3(t)$ and $\hat{a}_4(t)$ can be related to the operators $\hat{a}_1(t)$ and $\hat{a}_2(t)$ for the two input ports. Assuming that the emitters sending light into the beam-splitter are independent but have identical expectation values corresponds to the case of consecutive emissions from the same QD. The coincidence counts are thus given by the correlation function [128]

$$G^{(2)}_{\mathrm{HOM}}(t,\tau) = \frac{1}{2}\left[\rho_{\mathrm{qd}}(t)\rho_{\mathrm{qd}}(t+\tau) - |G^{(1)}(t,\tau)|^2\right] \quad (5.5)$$

$$= \frac{1}{2}\mathrm{e}^{-2\gamma t}\mathrm{e}^{-\gamma\tau}\left[1-\mathrm{e}^{-2\gamma_{\mathrm{dp}}\tau}\right]\ . \quad (5.6)$$

Experimentally we only measure the delay time τ between the two single photon detection events, and because the total detection time T is much longer than the single photon pulse-width we can write the experimentally measured correlation function as

$$G^{(2)}_{\mathrm{HOM,\,exp}}(\tau) = \lim_{T\to\infty}\int_0^T G^{(2)}_{\mathrm{HOM}}(t,\tau)dt = \frac{1}{4\gamma}\mathrm{e}^{-\gamma\tau}\left[1-\mathrm{e}^{-2\gamma_{\mathrm{dp}}\tau}\right]\ . \quad (5.7)$$

In the limiting case of indistinguishable photons ($\gamma_{\mathrm{dp}} \to 0$) the coincidence counts go to zero, meaning that the two incoming photons always bunch in one of the two output arms of the beam-splitter. In the opposite case of completely distinguishable photons ($\gamma_{\mathrm{dp}} \to \infty$) the coincidence counts decay with the lifetime of the emitter. In between these two extrema the coincidence counts curiously always vanish at zero time delays. This central dip occurs because the time intervals between photodetections are shorter than the mutual coherence time of the two photons, thus making them indistinguishable. The first factor in Eq. (5.7) thus arises from the incoherent dynamics, while the second factor

comes from the coherent dynamics. Often in experiments, this structure cannot be resolved due to the time resolution of the detectors and only the integrated coincidence counts are available. This area is given by

$$\mathrm{A}_0 = 2 \lim_{T\to\infty} \int_0^T G^{(2)}_{\mathrm{HOM,\,exp}}(\tau) d\tau = \frac{1}{\gamma^2} \frac{\gamma_{\mathrm{dp}}}{\gamma + 2\gamma_{\mathrm{dp}}} \quad , \tag{5.8}$$

where a factor of 2 takes the negative delay times into account. The case of completely distinguishable photons gives an area of

$$\mathrm{A}_1 = \lim_{\gamma_{\mathrm{dp}}\to\infty} \mathrm{A}_0 = \frac{1}{2\gamma^2} \quad , \tag{5.9}$$

so we can define the indistinguishability, V, as

$$\mathrm{V} = 1 - \frac{\mathrm{A}_0}{\mathrm{A}_1} = \frac{\gamma}{\gamma + 2\gamma_{\mathrm{dp}}} \quad , \tag{5.10}$$

which vanishes in the case of distinguishable photons and takes the value of unity in the case of indistinguishable photons. This expression agrees with that obtained in [129]. It is evident that dephasing degrades the indistinguishability of the emitted single photons, but it can be compensated for by Purcell-enhancing the decay rate, which has been demonstrated experimentally [72]. This can be understood by considering the emitter in the frequency domain, where in the absence of dephasing the spectrum of the emitter is only lifetime-broadened. Pure dephasing corresponds to adding an inhomogeneous broadening to the spectrum of the emitter, but this can be compensated for by increasing the lifetime-broadening, which corresponds to Purcell-enhancing the decay rate.

5.4.2 Experimental setup

The experimental setup is shown in Fig. 5.8, where the part before the PM fiber is the one we previously used for the investigation of photonic-crystal cavities. The sample is placed in the cryostat, accessed optically using confocal microscopy, where the excitation and emission are separated by a dichroic mirror, and the emission is coupled into the PM fiber after polarization selection. Before coupling the pulsed Ti:Sapph laser into the excitation fiber, we send half of the excitation beam through an optical delay path of 3.04 ns before coupling it back into the original optical mode. This results in two pulses separated by 3.04 ns arriving at the sample every 13 ns (corresponding to the laser

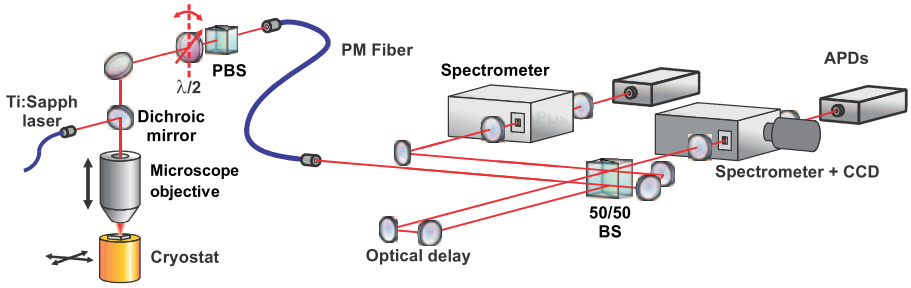

Figure 5.8: Experimental setup used for indistinguishability measurement. Every 13 ns two pulses from the Ti:Sapph laser separated by 3.04 ns excite the sample. The emission is sent through a HOM interferometer, where ideally the first photon goes to the reflected arm and is delayed by 3.04 ns compared to second photon that goes into the transmission arm. Both photons are reflected both to the same beam-splitter and interfered. The outputs are sent through spectrometers before the coincidence counts are measured using APDs.

repetition rate of 76 MHz). We can consider the case where every excitation event gives rise to a detected photon, because only these events give rise to coincidence counts. Thus every 13 ns two single photons separated by 3.04 ns arrive at the output of the PM fiber shown in Fig. 5.8 and are directed into the Hong-Ou-Mandel interferometer [88]. The optical beam is incident on a 50:50 beam-splitter, where the reflected arm has an optical delay of 3.04 ns compared to the other arm. The beams in both arms are reflected back to the same beam-splitter, where the two beams are interfered. Both output beams are sent through spectrometers before being incident on APDs for detection. Importantly, the resolution of the spectrometers is 0.05 nm, and it only allows us to filter away other emission lines, not to spectrally filter on the emission line, i.e. post-select. For these measurements the photon flux in the optical beam is very important, since reducing it by a factor of two reduces the coincidence counts by a factor of four. Therefore we use APDs from Perkin Elmer, model SPCM CD3371H, that offer a high quantum efficiency of $\sim 35\%$ at 900 nm with dark counts of 70 Hz and a dead-time of 25 ns. The downside of using these APDs is their low time-resolution of 330 ps. For coincidence measurements, dark counts are not a problem since they very rarely give rise to any coincidence counts. It is important that the delay in the excitation exactly

matches the delay in the HOM interferometer, and we ensure this to a high precision (< 20 ps) through time-resolved measurements.

5.4.3 Measurements under LO phonon-mediated excitation

We now excite the X-line using LO phonon-mediated excitation, where the excitation laser is tuned to the resonance at 854.56 nm. By blocking one of the delay arms in the HOM interferometer, we continuously perform autocorrelation measurements, and because we excite below saturation power the emission always exhibits complete anti-bunching, as we verified in Fig. 5.3(c). The outcome of a HOM measurement under LO phonon-mediated excitation is shown in Fig. 5.9(a), and it gives a cluster of five peaks for every 13 ns, where only the center peak corresponds to the desired two-photon interference. The peaks correspond to all the other possible path-combinations that the two photons can take in the HOM interferometer. Counting from the left, the first peak originates from the first photon taking the short path in the HOM interferometer, while the second photon takes the long path giving a delay time of $-2 \cdot 3.04$ ns. The second peak originates from both photons taking either the short and long path, in which case the delay time is -3.04 ns. The third (i.e. center) peak comes from the first photon taking the long path and the second photon the short path, which gives rise to the two-photon interference effect around zero delay time. These combinations should be mirrored around the center peak, because it is probabilistic which output port of the beam-splitter the photons go out through, and this gives rise to the fourth and fifth peaks. In the case of completely distinguishable photons, the relative intensities in the peaks 1-5 should be $1:2:2:2:1$, while the center peak should vanish completely for indistinguishable photons. As shown in Eq. (5.7), all of the peaks fall of exponentially with the decay rate of the X-line. Although we have chosen the delay to be large (3.04 ns), the inhibited decay rate ($\gamma = 0.62$ ns^{-1}) of the X-line means that all the peaks overlap with their neighboring peaks. A larger delay will increase the peak-to-peak distance, but in that case the peaks from the neighboring clusters will begin to overlap, so the delay chosen was found to be optimum.

In Fig. 5.9(c) we have zoomed in on the center peak in Fig. 5.9(a), where we see a clear suppression of the center peak. Furthermore, we see that the center peak, as expected from theory, actually has a double peak structure with a dip

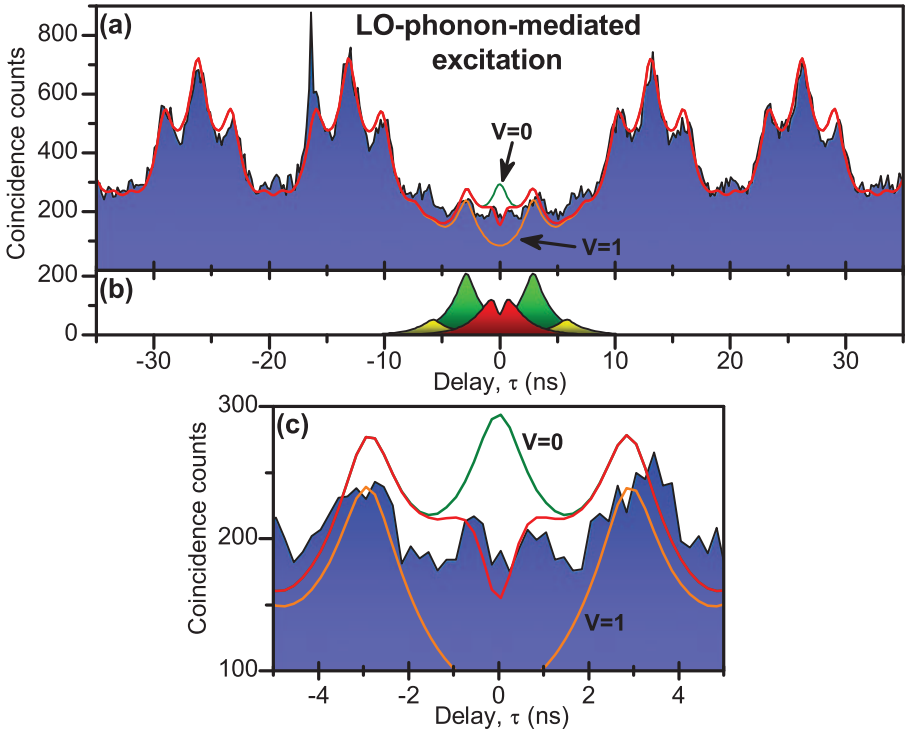

Figure 5.9: **a)** Indistinguishability measurements under LO phonon-mediated excitation at the temperature 5 K and under an excitation power of 0.88 $P_{\mathrm{sat}}^{\mathrm{X}}$. The data shows a cluster of five peak every 13 ns, where only the center peak at $\tau = 0$ corresponds to the two-photon interference. The fit shows a reasonable agreement with the data, and in **(b)** the fit is decomposed into the five peaks, where the fine structure of the central peak with a small central dip is clear. **c)** Shows a zoom-in around the center peak. For reference the lines corresponding to completely distinguishable ($V = 0$) and indistinguishable ($V = 1$) photons are also shown. We extract the indistinguishability $V_{\mathrm{LO}} = 0.20 \pm 0.07$, which corresponds to a low dephasing rate of $\hbar\gamma_{\mathrm{dp}}^{\mathrm{LO}} = 0.82 \pm 0.41$ μeV.

in the middle. This is experimental evidence for the effect that photons emitted very fast have not been subject to much dephasing and consequently they are indistinguishable. In previous work, this fine structure of the center peak has not been observed, because Purcell enhancement of the decay rate has been

used to increase the indistinguishability making this fine structure impossible to resolve temporally [72, 115].

In order to model the recorded data in Fig. 5.9(a), we initially leave out the data from the cluster around zero time delay. Because the beam-splitter is balanced, as verified by measurements, we can assume the amplitudes of peak 1 and 5 are identical and that the amplitude of peak 2 and 4 are also identical. The time delay between the peaks has been measured independently and each peak is given by an exponential function, where the decay rate has also been measured independently. By propagating a laser pulse through the system we record an IRF, and the exponential function is convoluted with the IRF before fitting. When modeling the data away from the central cluster the only free parameters we thus need are the amplitudes of peaks 1, 2, and 3.

Having determined these we now include the central cluster of peaks in the data. We assume that the ratios between the peaks 1 and 2 are unchanged, and we thus only need one overall amplitude for fitting the peaks 1,2,4, and 5. The amplitude of the central peak is the same as for peaks 2 and 4. The center peak is therefore modeled with the expression in Eq. (5.7) after convolution with the IRF and with γ_{dp} as a free parameter. Fig. 5.9(a-c) shows the theory curve and we obtain an indistinguishability of $V_{\mathrm{LO}} = 0.20 \pm 0.07$ under LO phonon-mediated excitation. The model shows a reasonably good agreement, and for reference we also show the curves corresponding to $V = 0$ and $V = 1$, where we note that even the $V = 1$-curve does not go completely to zero due to the overlaps. In Fig. 5.9(b) the theory is decomposed into the five peaks, and the central dip due to indistinguishability of the photons is evident. Using the relation we derived in Eq. (5.10) we extract the coherence rate $\hbar(\gamma/2 + \gamma_{\mathrm{dp}}^{\mathrm{LO}}) = 1.02 \pm 0.41$ μeV, which gives a pure dephasing rate of $\hbar\gamma_{\mathrm{dp}}^{\mathrm{LO}} = 0.82 \pm 0.41$ μeV. The data were recorded at the temperature 5 K and under an excitation power of 0.88 $P_{\mathrm{sat}}^{\mathrm{X}}$.

5.4.4 Measurements under LA phonon-mediated excitation

The excitation laser is now tuned into resonance with the M3 mode in order to excite the X-line using LA phonon-mediated excitation. An example of the very clean emission spectrum can be seen in Fig. 5.7 and autocorrelation measurements verify that the emission still exhibits complete anti-bunching. We now perform HOM measurements on the emission in the exact same way

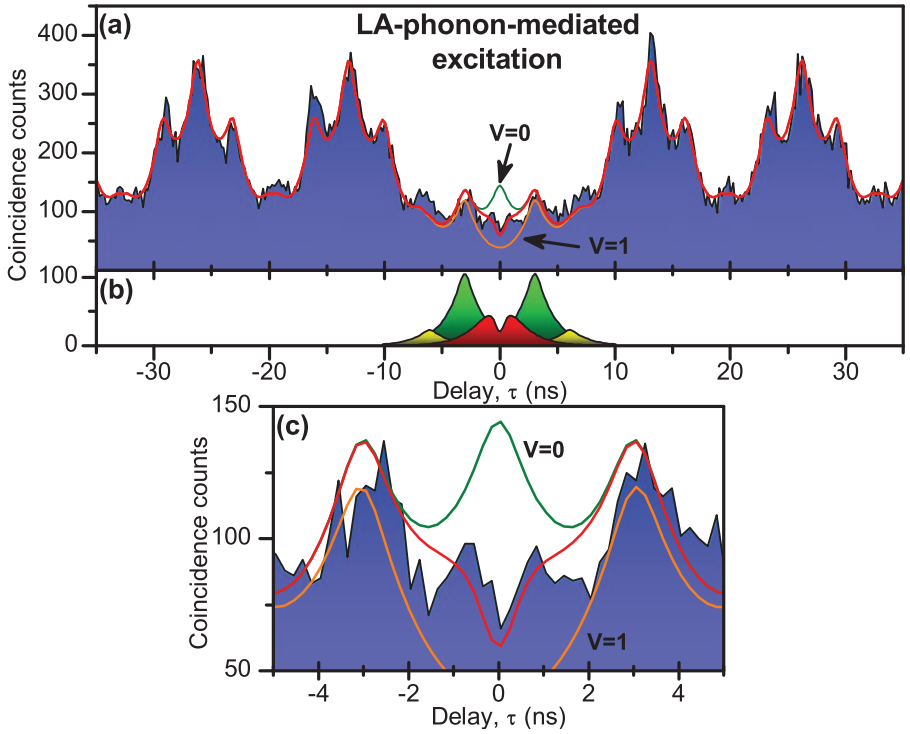

Figure 5.10: **a)** Indistinguishability measurements under LA phonon-mediated excitation at the temperature 4.8 K and under an excitation power of 0.10 $P_{\mathrm{sat}}^{\mathrm{X}}$. The fit shows a reasonable agreement with the data and in **(b)** the fit is decomposed into the five peaks, where the fine structure of the central peak with a small central dip is clear. **c)** Shows a zoom-in around the center peak. For reference the lines corresponding to completely distinguishable $V = 0$ and indistinguishable $V = 1$ photons are also shown. We extract the indistinguishability $V_{\mathrm{LA}} = 0.33 \pm 0.09$ which corresponds to a very low dephasing rate of $\hbar\gamma_{\mathrm{dp}}^{\mathrm{LA}} = 0.42 \pm 0.18$ μeV, which is a reduction by a factor of two compared to LO phonon-mediated excitation.

as under LO phonon-mediated excitation. The outcome of the measurement can be seen in Fig. 5.10(a), and in (c) we have zoomed in on the area around the center peak at $\tau = 0$. We notice, that the center peak seems less intense, and that the dip within the center peak is more pronounced than under LO phonon-

mediated excitation. The data is now modeled following the same procedure as before, and the theory curve is seen to be in reasonably good agreement with the data in Fig. 5.10(c). From the theory we extract an indistinguishability of $V_{\mathrm{LA}} = 0.33 \pm 0.09$, and in Fig. 5.10(b) the model is decomposed into the five peaks. A clear dip within the center peak is also seen in Fig. 5.10(b), and this center dip originates from photons being emitted before they have had time to dephase thus making them indistinguishable. Resolving this dip is only possible because the decay rate of the emission is inhibited and because the dephasing rate is low. This center dip holds information on the dephasing at early times, where, e.g., LA phonons have been shown to give rise to a time-dependent dephasing rate. This rate varies strongly within the first ~ 4 ps, after which it settles to a constant level [130].

From the indistinguishability we extract the coherence rate $\hbar(\gamma/2+\gamma_{\mathrm{dp}}^{\mathrm{LA}}) = 0.62 \pm 0.18$ μeV, which gives a very low pure dephasing rate of $\hbar\gamma_{\mathrm{dp}}^{\mathrm{LA}} = 0.42 \pm 0.18$ μeV at 4.8 K and under an excitation power of 0.10 $P_{\mathrm{sat}}^{\mathrm{X}}$. In comparison this dephasing rate is 5 times lower than the one we measured for a QD in a micropillar cavity even after having compensated for the temperature by assuming a linear dependency. Low dephasing rates have been demonstrated for a QD in a micropillar cavity, where the value 0.46 μeV was obtained at $3-7$ K under p-shell excitation [72]. However, previous work on QDs in photonic-crystal cavities used a strong Purcell enhancement to obtain a high indistinguishability of 0.72, while the pure dephasing rate was measured to 2.34 μeV at 4 K under p-shell excitation [115].

We also note that the dephasing rate decreases when changing from LO to LA phonon-mediated excitation, which we attribute to the much smaller residual energy being emitted as LA-phonons. For LO phonons the energy difference between excitation and emission is 81.2 meV, while it is only 7.2 meV for the LA phonons. One would therefore expect the LO-phonons to perturb the lattice and thus the exciton wavefunctions significantly more than LA phonons, and thus give rise to the higher dephasing rate. Furthermore, the almost completely flat dispersion of the LO phonons implies a very slow group velocity, and as a result LO phonons do not propagate over the timescale of the dynamics. Instead LO phonons scatter into e.g. LA phonons, where one LO phonon can decay into two LA phonons both with half the energy and opposite wavevectors. The lifetime of LO phonons has been measured to 7

ps in GaAs at 77 K [23], and LO phonons thus give rise to dephasing on a very short timescale before decaying into LA phonons that propagate away. Before decaying LO phonons perturb the lattice at the position of the exciton wavefunctions, which is expected to dephase the wavefunctions considerably. In comparison LA phonons propagate with the speed of sound $\sim 5110\frac{\text{nm}}{\text{ns}}$ and they therefore only distort the lattice, where the exciton is confined, for a short time.

Using the dephasing rate from LA phonon-mediated excitation, we estimate that if the X-line had a Purcell factor of 5, the indistinguishability would be very high, V= 0.86. However, studying slow QDs has the advantage that the coherence of the photons is limited not by the lifetime but by the dephasing rate. In this way we can study how the QD is dephased at early times and investigate whether or not pure dephasing is the correct model to apply for the times shortly after the excitation.

5.5 Absorption of LA-phonons

In the previous demonstrations of LA phonon-mediated excitation, the excitation laser had a higher energy than the QD emission, and the residual energy was emitted as LA phonons. Now we study the opposite case, where the excitation laser has lower energy than the QD emission and relies on the absorption of LA phonons in order to excite the QD. In Fig. 5.11(a) we show an emission spectrum, where the excitation laser is tuned into resonance with the M4 mode at 914.7 nm and we observe strong emission from the X-line. However, we note that the emission spectrum is not nearly as clean the one in Fig. 5.7, where excitation relied on the emission of LA phonons. In Fig. 5.11(b) we show a PLE measurement, where we have scanned the excitation laser across the M4 mode while detecting the total intensity in the X-line. The precise power applied to the sample is difficult to determine due to the wavelength-dependent reflection of the dichroic mirror, but we make sure to operate below saturation of the X-line. The data clearly map out the linewidth of the M4 mode, and we fit the data with a Lorentzian (solid red line), which gives a Q-factor of 3354 with a center wavelength of 914.76 nm. This is in good agreement with the Q-factor 2927 and center wavelength 914.61 nm we extract from strong above-band excitation, where the M4 mode is visible in the emission spectrum. Because

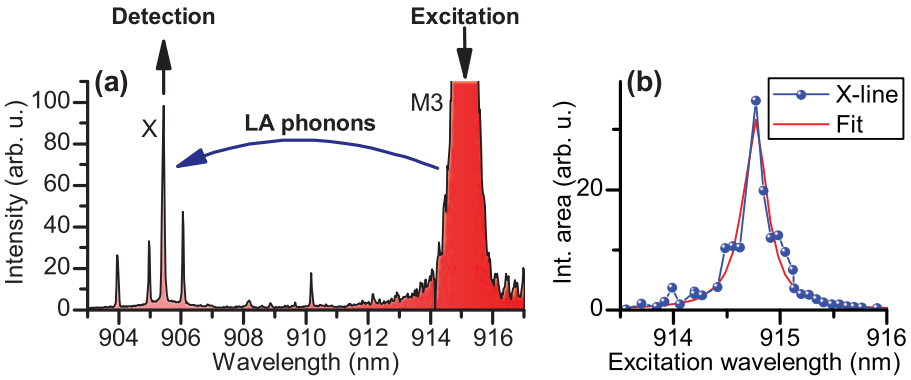

Figure 5.11: **a)** Emission spectrum where the laser is coupling to the M4 mode and absorption of LA phonons makes excitation of the X-line possible. **b)** PLE measurement where the total intensity in the X-line is plotted as a function of the excitation wavelength at low excitation powers and at 10 K. The linewidth of the M4 mode is mapped out, and it agrees very well with that obtained from emission spectra. This proves that the feeding mechanism is broadband and thus due to the absorption of LA phonons.

the absorption follows the linewidth of the M4 mode, the feeding mechanism is broadband and it must be due to LA phonons, since no other broadband mechanisms should be present.

The data in Fig. 5.11 are taken at the temperature 10 K, and the energy difference between the X-line and the center of the M4 mode used for excitation is 14.08 meV. Evaluating the thermal occupation number at this energy and temperature gives an occupation number of $8.5 \cdot 10^{-8}$, which would imply that the absorption of single LA phonons is highly improbable. Most likely, the laser induces some local heating effects that would increase the thermal occupation of phonons. Although the absorption coefficient is only $\alpha = 2.4 \cdot 10^{-5}$ nm^{-1} in GaAs [20], the Q-factor of the cavity enhances the absorption to $Q\alpha = 0.08$ nm^{-1}, and because the M4 has a relatively high Q factor the excitation light is strongly confined and could heat the lattice around the QD significantly. As an example if the local temperature is 35 K, then the thermal occupation is $n = 0.01$. Furthermore, multiphonon absorption processes, where several low-energy phonons are absorbed, could also contribute. However, these processes

are also subject to selection rules that need to be taken into account [131].

Finally we note that it was possible to excite the X-line even at 5 K, where we measured the linewidth of the X-line using a scanning Fabry-Perot. Though not conclusive, these measurements indicated that the spectral linewidth of the X-line was above 20 μeV, in stark contrast to the linewidths of 2.04 ± 0.82 and 1.24 ± 0.36 μeV expected from indistinguishability measurements under LO and LA phonon-mediated excitation. This would most likely be due to spectral diffusion, i.e., spectral wandering of the X-line due to changes in the electrostatic environment. Spectral diffusion is expected to take place on a slow timescale (up to seconds), which is also the timescale of the Fabry-Perot measurements, and it would thus broaden the measured linewidths, but not influence the outcome of a HOM measurement, where the dephasing rate is probed on a nanosecond timescale.

5.6 Conclusion

We have performed measurements on a QD detuned from a low-Q mode of a photonic-crystal cavity. The exciton, bi-exciton and charged exciton was identified using power series and cross-correlations measurements, and by comparing to a bulk QD we derived a collection efficiency at the first lens of $(44.3 \pm 2.1)\%$. Autocorrelation measurements proved the single-photon nature of the emission, and a pronounced anti-bunching was observed for excitation powers 21 times higher than the saturation power. The efficiency and Purcell factor has been measured for many QDs, and the high efficiency is seen to be reproducible with 5 QDs showing efficiencies above 25%, while no strong correlation between efficiency and Purcell factor was observed.

The high efficiency was also investigated by performing numerical simulations of the far-field pattern. The collection efficiency at the first lens was calculated for the experimentally used N.A.$= 0.6$, and in agreement with experiment we found the high efficiencies to be broadband and not strongly correlated with the Purcell factor. This proved that it is not the coupling to the M3 mode but rather the modification of the far-field pattern due to the cavity structure that is responsible for the high efficiency. However, the calculated efficiencies were found to be systematically lower than the experimentally measured values. We attribute this discrepancy to the under-etch of the membrane, since

half of the emission from the QD propagates down towards the substrate, and at the air-GaAs interface a significant part will be reflected upwards towards the collection lens.

We have demonstrated both LO and LA phonon-mediated excitation by exciting the QD through phonon absorption lines that lie within the linewidth of higher-order cavity modes. LO phonon-mediated excitation of both the exciton and bi-exciton by absorption of 2 LO-phonons was demonstrated and shown to be 7 times more efficient than above-band excitation. The energy difference between the exciton and bi-excitonic LO phonon absorption lines matched very well with the energy difference between the exciton and bi-exciton emission lines. However, the energy of the 2 LO phonon line was slightly larger than expected from theory, which we provide some possible explanations for. Selective excitation of the exciton was demonstrated by LA phonon mediated excitation. This resulted in an emission spectrum much cleaner than under LO phonon-mediated excitation and only the exciton emission line can be seen.

In order to investigate the effect of excitation on the dephasing we performed indistinguishability measurements of the exciton emission line under both LO and LA phonon-mediated excitation. Under the former we extract an indistinguishability of 0.20 ± 0.07. However, this value is only low because the radiative decay rate of the exciton is inhibited, and the extracted pure dephasing rate of $\hbar\gamma_{\mathrm{dp}}^{\mathrm{LO}} = 0.82 \pm 0.41$ μeV at 5 K is a low rate. Under LA phonon-mediated excitation we measure an indistinguishability of 0.33 ± 0.09, but we extract the very low pure dephasing rate of $\hbar\gamma_{\mathrm{dp}}^{\mathrm{LA}} = 0.42 \pm 0.18$ μeV at 4.8 K. The pure dephasing rate thus decreases when going from LO to LA phonon-mediated excitation. We attribute this to the much smaller residual energy being emitted into the lattice as phonons, which is 81.2 meV for LO phonons but only 7.2 meV for LA phonons. Furthermore, while LA phonons propagate away from the QD quickly, LO phonons stay localized around the exciton wavefunctions and perturb the lattice before decaying into LA phonons that propagate away. LO phonons thus give rise to an additional very fast dephasing of the exciton wavefunctions. Interestingly, we were able to resolve the fine structure of the center peak in the indistinguishability measurement. This dip occurs because the photons have been emitted before the environment has had time to dephase the QD. The inhibition of the radiative decay rate thus enables us to probe dephasing at early times, and investigate whether or not

pure dephasing is the correct model to apply in this regime. Finally, we demonstrated that we can also excite the QD with lower-energy photons and rely on the absorption of LA phonons to mediate the excitation.

Chapter 6

Resonant excitation of quantum dots in photonic crystals

In the previous chapters we studied the selective excitation of QDs through the p-shell, higher-order modes of the cavity, and phonon resonances, but the most selective and cleanest excitation is to tune the laser into resonance with the s-shell of the QD. This makes it possible to address the exciton of interest. Only recently has resonance fluorescence from a solid-state emitter been demonstrated [132, 133], where Mollow triplets resulting from the dressing of the exciton level in a QD with the laser was shown. Furthermore, coherent oscillations of the QD were proven by observing the oscillations in the second-order correlation. The biggest technical difficulty in resonance fluorescence is to separate the excitation laser from the emission, since they both have the same wavelength. In the aforementioned work the separation was done by coupling the excitation laser into a waveguide containing the QDs and observing the emission in the orthogonal direction. Spin-resolved resonance fluorescence was observed not long after [134], where Mollow triplets were observed for both excitons separated by the fine-structure splitting. Resonant excitation was also seen to minimize decoherence compared to non-resonant excitation, and the most remarkable reduction in decoherence was demonstrated in [135],

where a 30-fold reduction of the emission linewidth with respect to the radiative linewidth of the QD was observed. Normally the radiative decay rate sets a minimum linewidth of the QD through the Fourier transform, but the excitation laser results in a coherently and incoherently scattered part of the field, where the former part inherits the coherence properties of the incident laser while remaining anti-bunched [136]. The total field is dominated by the coherent part at low powers and for relatively small dephasing rates. In contrast to the incoherent part, the coherent part has a phase relation to the excitation laser, and this has been demonstrated by optical heterodyning measurements [137].

Exciting the QD with a pulsed resonant laser allows us to fulfill the requirement of on-demand single photons. Here the QD can be prepared in any superposition of the ground and excited state by adjusting the pulse area [132, 138], and the final population of the QD thus varies periodically with pulse area. Not surprisingly dissipation damps this process, and recent work demonstrated that phonon dephasing due to acoustic phonons is the principal responsible for the intensity damping [139] and gives rise to a renormalization of the coupling strength [114]. The emitted photons under such pulsed excitation were impressively shown to have a high degree of indistinguishability of $\sim 97\%$ and were used to successfully construct a quantum controlled-NOT gate [119]. Under non-resonant excitation the exciton relaxes down to the s-shell of the QD with some rate, which gives rise to a time-jitter on the time of excitation. This time-jitter degrades the indistinguishability, but it can be eliminated under pulsed resonant excitation, which is probably part of the reason for the high degree of indistinguishability measured in [119]. Furthermore, the strictly resonant excitation eliminates the excitation of other charges in the system and could potentially reduce fluctuations in the electrostatic environment.

The work described in this chapter is still in progress, and as a result only a single measurement will be presented. The theory for both continuous and pulsed resonant excitation will be derived and essential features will be described. Afterwards, the experimental setup will be described in detail, and a measurement showing the experimental proof of resonant excitation will be shown. Finally, the outlook of the project will be presented and discussed.

6.1 Resonance fluorescence

While we previously studied the spontaneous decay of a QD due to the vacuum fluctuations of the electromagnetic field, we here study the emission from the QD while it is irradiated by a continuous monochromatic electric field, and this is called resonance fluorescence. The derivations in this section follow those presented in [53]. When studying spontaneous emission and the Jaynes-Cummings model, we assumed that the QD was initially in the excited state. In the present theory the excitation of the QD is included in the model, and we assume that the QD is in the ground state initially. From the derivations in section 2.1.2 we find that the Hamiltonian in the rotating frame is given by

$$\hat{H} = \hbar\frac{\Omega}{2}(\hat{\sigma}_- + \hat{\sigma}_+) + \hbar\Delta\hat{\sigma}_+\hat{\sigma}_- \quad , \tag{6.1}$$

where $\Omega = -2\hbar^{-1}\mathbf{d_{eg}}\cdot\mathbf{E}$ is the Rabi frequency and $\Delta = \omega_{\mathrm{qd}} - \omega_{\mathrm{la}}$ is the detuning between the QD (ω_{qd}) and laser (ω_{la}) frequency. In this semiclassical description the emitter, i.e. QD, is quantized, while the driving field is a coherent state that is described classically. In accordance with section 2.4 we describe the system using the density operator for which the equation of motion can be written

$$\dot{\rho} = -\frac{i}{\hbar}[\hat{H},\hat{\rho}] + \mathcal{L}(\gamma,\hat{\sigma}_-) + \mathcal{L}(\gamma_{\mathrm{dp}}/2,\hat{\sigma}_{\mathrm{z}}) \quad , \tag{6.2}$$

where $\hat{\sigma}_{\mathrm{z}} = [\hat{\sigma}_+,\hat{\sigma}_-]$. The first term in the equation governs the coherent light-matter interaction, while the second term is a Lindblad term that describes the decay of the QD with the rate γ, and the last Lindblad term describes pure dephasing of the QD levels. The density matrix is a two by two matrix, but writing the elements as a vector of dimension four gives the following equations of motion

$$\begin{pmatrix} \dot{\rho}_{11} \\ \dot{\rho}_{12} \\ \dot{\rho}_{21} \\ \dot{\rho}_{22} \end{pmatrix} = \begin{pmatrix} -\gamma & i\Omega/2 & -i\Omega/2 & 0 \\ i\Omega/2 & -\frac{\gamma+2\gamma_{\mathrm{dp}}}{2} - i\Delta & 0 & -i\Omega/2 \\ -i\Omega/2 & 0 & -\frac{\gamma+2\gamma_{\mathrm{dp}}}{2} + i\Delta & i\Omega/2 \\ \gamma & -i\Omega/2 & i\Omega/2 & 0 \end{pmatrix} \begin{pmatrix} \rho_{11} \\ \rho_{12} \\ \rho_{21} \\ \rho_{22} \end{pmatrix} \tag{6.3}$$

which we in shorthand write $\dot{\rho}_{\mathrm{v}}(t) = \mathbf{M}\rho_{\mathrm{v}}(t)$. We note that using the relation $\langle\hat{\sigma}_+(t)\hat{\sigma}_-(t)\rangle = Tr(\rho(t)\hat{\sigma}_+\hat{\sigma}_-) = \rho_{11}(t)$ we make the following identifications;

$\langle\hat{\sigma}_-\hat{\sigma}_+\rangle = \rho_{22}(t)$, $\langle\hat{\sigma}_+\rangle = \rho_{12}(t)$, and $\langle\hat{\sigma}_-\rangle = \rho_{21}(t)$. From Eq. (6.3) we thus observe that in absence of any driving field the QD simply decays with the rate γ and the polarization decays with the rate $(\gamma/2 + \gamma_{\rm dp})$. However, when including the driving laser, the excited and ground state of the QD become coupled through the polarization.

6.1.1 Steady state solutions

Because the driving field is continuous, the QD will eventually settle in a steady state. In this case the left hand of Eq. (6.3) can be set to zero, and we find the following expression for the polarization

$$\rho_{12} = \frac{i\Omega}{\gamma/2 + \gamma_{\rm dp} + i\Delta}\left(\rho_{11} - \frac{1}{2}\right) \quad . \tag{6.4}$$

Inserting this into the equation for $\rho_{11}(t)$ gives us the population of the QD in the steady state limit

$$n_{\rm ss} = \rho_{11}(t)|_{ss} = \frac{\Omega^2}{4\gamma}\frac{\gamma + 2\gamma_{\rm dp}}{\Delta^2 + (\gamma + 2\gamma_{\rm dp})(\gamma + 2\gamma_{\rm dp} + 2\Omega^2/\gamma)/4} \quad . \tag{6.5}$$

We note that using the above definitions, the Rabi frequency squared is proportional to the intensity of the driving laser, i.e. $\Omega^2 \propto I$. In Fig. 6.1 the steady state population, $n_{\rm ss}$, is plotted as a function of intensity, Ω^2, for $\Delta = 0$, where the population increases linearly until it reaches saturation at $\Omega^2 = \gamma(\gamma/2 + \gamma_{\rm dp})$. At saturation the population approaches $1/2$, and detuning decreases this value.

6.1.2 Second order correlation

We now study the second order correlation function because it is experimentally accessible and because it can reveal whether or not the emission is of single-photon nature. In order to calculate this function we must first solve the equation of motion given in Eq. (6.3) that is of the form $\dot{\rho}_{\rm v}(t) = \mathbf{M}\rho_{\rm v}(t)$, in which case we can simply write the solution as

$$\rho_{\rm v}(t+\tau) = \mathbf{U}(\tau)\rho_{\rm v}(t) \ \text{, where} \ \ \mathbf{U}(\tau) = \mathrm{e}^{\mathbf{M}\tau} \quad . \tag{6.6}$$

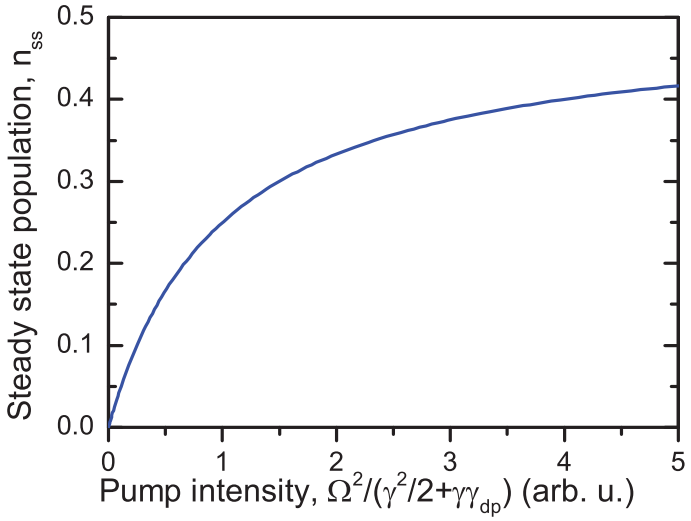

Figure 6.1: The steady state population of the QD as a function of Ω^2, which is proportional to the intensity of the driving field. The population increases linearly until reaching saturation when $\Omega^2 = \gamma(\gamma/2 + \gamma_{\rm dp})$ and the population approaches $1/2$.

According to the quantum regression theorem [38], if the one-time expectation value of the operator $\hat{A}$ is given by

$$\langle \hat{A}(t+\tau)\rangle = \sum_i \alpha_i(\tau)\langle \hat{A}_i(t)\rangle \quad , \tag{6.7}$$

then the two-time expectation value with the two other operators $\hat{B}$ and $\hat{C}$ can be expressed

$$\langle \hat{B}(t)\hat{A}(t+\tau)\hat{C}(t)\rangle = \sum_i \alpha_i(\tau)\langle \hat{B}(t)\hat{A}_i(t)\hat{C}(t)\rangle \quad . \tag{6.8}$$

Using this theorem we can calculate the unnormalized second order correlation function to be

$$\begin{aligned} G^{(2)}(\tau,t) &= \langle \hat{\sigma}_+(t)\hat{\sigma}_+(t+\tau)\hat{\sigma}_-(t+\tau)\hat{\sigma}_-(t)\rangle & (6.9)\\ &= \mathbf{U}_{11}(\tau)\langle \hat{\sigma}_+(t)\hat{\sigma}_+(t)\hat{\sigma}_-(t)\hat{\sigma}_-(t)\rangle + \mathbf{U}_{12}(\tau)\langle \hat{\sigma}_+(t)\hat{\sigma}_+(t)\hat{\sigma}_-(t)\rangle \\ &+ \mathbf{U}_{13}(\tau)\langle \hat{\sigma}_+(t)\hat{\sigma}_-(t)\hat{\sigma}_-(t)\rangle + \mathbf{U}_{14}(\tau)\langle \hat{\sigma}_+(t)\hat{\sigma}_-(t)\hat{\sigma}_+(t)\hat{\sigma}_-(t)\rangle \\ &= \mathbf{U}_{14}(\tau)\rho_{11}(t) & (6.10) \end{aligned}$$

because $\hat{\sigma}_+(t)\hat{\sigma}_+(t) = \hat{\sigma}_-(t)\hat{\sigma}_-(t) = 0$, which holds because the two-level system can maximally hold one excitation. Assuming that the time, t, is large enough for steady state conditions to be reached, we can replace $\rho_{11}(t)$ with the steady state population n_{ss}. This results in the following normalized second order coherence function

$$g^{(2)}(\tau) = \frac{\mathbf{U}_{14}(\tau)}{n_{\mathrm{ss}}} \quad , \tag{6.11}$$

which assuming resonance, $\Delta = 0$, can be calculated to give [53]

$$g^{(2)}(\tau) = 1 - \mathrm{e}^{-(\gamma_{\mathrm{dp}}/2+3\gamma/4)\tau}\left(\cos(\mu\tau) + \frac{2\gamma_{\mathrm{dp}} + 3\gamma}{4\mu}\sin(\mu\tau)\right) \quad , \tag{6.12}$$

where $\mu = \sqrt{\Omega^2 - (\gamma/4 - \gamma_{\mathrm{dp}}/2)^2}$. Under strong excitation, i.e. $\Omega \gg \{\gamma, \gamma_{\mathrm{dp}}\}$, the above expression simplifies to

$$g^{(2)}(\tau) = 1 - \mathrm{e}^{-(\gamma_{\mathrm{dp}}/2+3\gamma/4)\tau}\cos(\Omega\tau) \quad , \tag{6.13}$$

from which it is seen that although the function still dips to zero for zero time delay, it exhibits oscillations damped by dissipation and decoherence for larger time delays. Similarly the following expression is found in the weak excitation regime

$$g^{(2)}(\tau) = 1 - \mathrm{e}^{-\gamma\tau} \quad , \tag{6.14}$$

where we have assumed that $\gamma \ll 2\gamma_{\mathrm{dp}}$, which is usually fulfilled when considering the case of a QD in a photonic crystal due to the strong inhibition of the radiative rate. This result is analogous to that obtained for a QD that is initially in the excited state and spontaneously decay with the rate γ, which is the case under incoherent excitation of the QD. In Fig. 6.2 the second order correlation function is plotted as a function of time delay for three different excitation powers. The emission is always anti-bunched at zero time delay, but the width of the dip varies strongly with excitation power. At low powers it is limited by the radiative decay rate, and with increasing powers the dip narrows and eventually damped oscillations appear at small time delays. These oscillations are proof of the coherent oscillations of the population driven by the excitation laser.

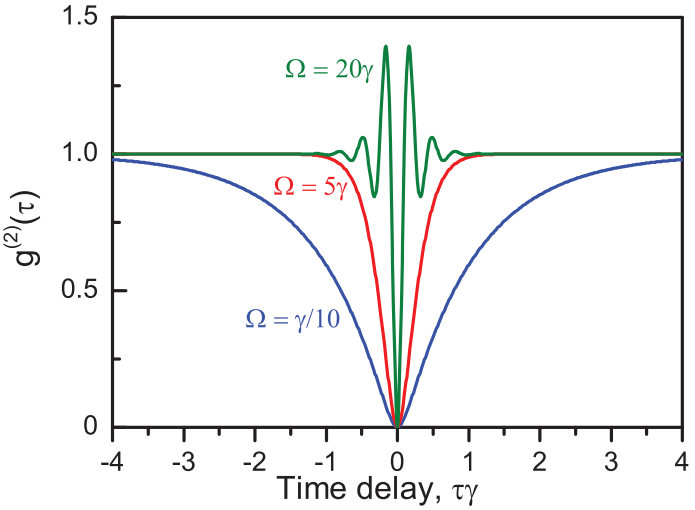

Figure 6.2: Second order correlation function as a function of time delay for three different excitation powers with $\gamma = \gamma_{\rm dp}/10$ and $\Delta = 0$. While the emission is always anti-bunched at zero time delay, the width of the dip is given by the radiative rate for low excitation powers and the dip narrows when increasing power until damped oscillations are observed at small time delays.

6.1.3 First order correlation

The coherence of a quantum system can most directly be probed by measuring the first order correlation function. Using the quantum regression theorem the unnormalized first order correlation function can be calculated to give

$$\begin{aligned} G^{(1)}(\tau,t) &= \langle \hat{\sigma}_+(t)\hat{\sigma}_-(t+\tau)\rangle \\ &= \mathbf{U}_{31}(\tau)\langle \hat{\sigma}_+(t)\hat{\sigma}_+(t)\hat{\sigma}_-(t)\rangle + \mathbf{U}_{32}(\tau)\langle \hat{\sigma}_+(t)\hat{\sigma}_+(t)\rangle \\ &+ \mathbf{U}_{33}(\tau)\langle \hat{\sigma}_+(t)\hat{\sigma}_-(t)\rangle + \mathbf{U}_{34}(\tau)\langle \hat{\sigma}_+(t)\hat{\sigma}_-(t)\hat{\sigma}_+(t)\rangle \\ &= \mathbf{U}_{33}(\tau)\rho_{11}(t) + \mathbf{U}_{34}(\tau)\rho_{12}(t) \quad . \end{aligned} \tag{6.15}$$

The normalized first order correlation function can be expressed as

$$g^{(1)}(\tau,t) = \frac{G^{(1)}(\tau,t)}{\left[\langle \hat{\sigma}_+(t)\hat{\sigma}_-(t)\rangle\langle \hat{\sigma}_+(t+\tau)\hat{\sigma}_-(t+\tau)\rangle\right]^{1/2}} = \frac{G^{(1)}(\tau,t)}{\sqrt{\rho_{11}(t)\rho_{11}(t+\tau)}} \quad . \tag{6.16}$$

Once again we assume that the time, t, is long enough for steady state conditions to apply, and we obtain the expression

$$g^{(1)}(\tau) = \mathbf{U}_{33}(\tau) + \frac{p_{\mathrm{ss}}}{n_{\mathrm{ss}}}\mathbf{U}_{34}(\tau) \quad , \tag{6.17}$$

where p_{ss} is the steady state polarization obtained by inserting Eq. (6.5) into Eq. (6.4). In the case of $\Delta = 0$ we find the following analytical expression [53]

$$g^{(1)}(\tau) = n_{\mathrm{ss}}\frac{\gamma^2}{\Omega^2} + \frac{1}{2}\mathrm{e}^{-(\gamma/2+\gamma_{\mathrm{dp}})\tau} \tag{6.18}$$

$$+ \frac{n_{\mathrm{ss}}}{\Omega^2}\mathrm{e}^{-(3\gamma/4+\gamma_{\mathrm{dp}}/2)\tau}\left(A\cos(\mu\tau) + \frac{B}{4\mu}\sin(\mu\tau)\right) \quad , \tag{6.19}$$

where the constants A and B have been defined as

$$A = \Omega^2 - (\gamma/2 - \gamma_{\mathrm{dp}})\gamma \quad ,$$
$$B = -(\Omega^2(2\gamma_{\mathrm{dp}} - 5\gamma) + 2\gamma\gamma_{\mathrm{dp}}^2 - 2\gamma^2\gamma_{\mathrm{dp}} + \gamma^3/2) \quad .$$

By setting dephasing to zero, i.e. $\gamma_{\mathrm{dp}} = 0$, and taking the low power limit, $\Omega \ll \gamma$ we see that the time dependence of $g^{(1)}(\tau)$ disappears and it approaches unity. This is also shown in Fig. 6.3(a), where $\gamma_{\mathrm{dp}} = 0$ and the coherence is seen to decay to a non-zero level for low powers. The scattered field has two components, namely the coherently and incoherently scattered field. In the former, a single photon in the driving field scatters off the two-level system without populating the system notably, and absorption and emission cannot be considered independent events. The incoherent part of the field originates from single photons of the driving field being absorbed and subsequently emitted. For spontaneous emission the coherence is always limited by the radiative lifetime, but the coherently scattered field is liberated from this constraint, and the coherence can as a result remain very high. Both the coherently and incoherently scattered part of the field are calculated from expectation values of the QD operators ($\hat{\sigma}_+$ and $\hat{\sigma}_-$) that both relate to the dipole moment of the QD. As a result the far-field pattern of both parts remains the dipole pattern, and from Eq. (6.14) we see that the field is also anti-bunched. As a result the coherence, i.e. $g^{(1)}(\tau)$, can remain very high, while the field still exhibits anti-bunching, which has been demonstrated experimentally [135, 137]. However, as shown in Fig. 6.3(b) dephasing destroys this effect by decreasing the steady state level of coherence. When the power is increased the incoherent

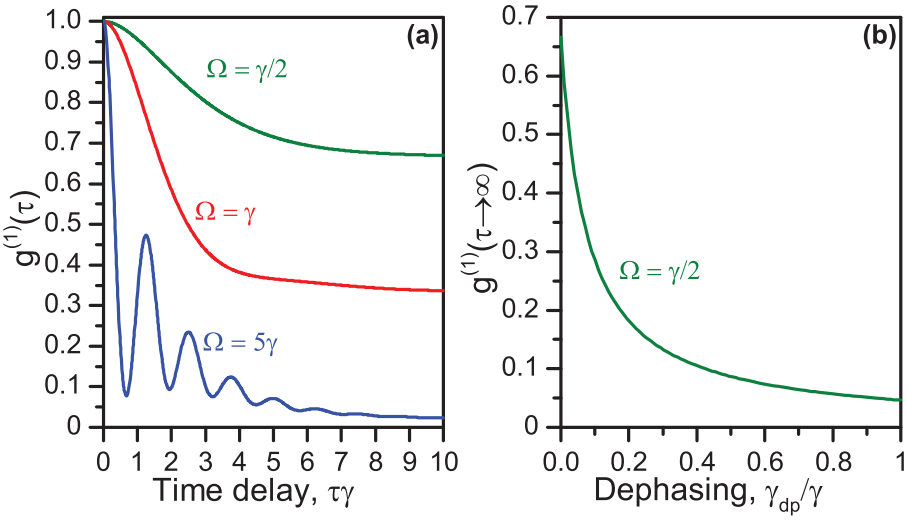

Figure 6.3: **a)** Normalized first order coherence as a function of time for three different pump powers and $\gamma_{\mathrm{dp}} = \Delta = 0$. For weak excitation the coherently scattered part dominates the field and the coherence reaches a steady state level that is much higher than the limit given by the radiative lifetime. When increasing power the coherence decreases until oscillations, due to the dressing of the two-level system with the laser, become visible. **b)** The steady state level of coherence as a function of dephasing showing that dephasing decreases the contribution of coherent scattering to the total field.

field becomes dominant and the coherence decreases. Eventually the driving laser becomes strong enough to dress the two-level system, and this gives rise to oscillations in the coherence as seen in Fig. 6.3(a).

6.1.4 Emission spectra

From the first order correlation function we can calculate one of the experimentally accessible properties, namely the emission spectrum. Because stationary conditions apply we can express the emission spectrum as the Fourier transform of the unnormalized first order correlation function [53]

$$S(\omega) = \frac{1}{\pi}\int_0^\infty G^{(1)}(\tau)\mathrm{e}^{i\omega\tau}d\tau \quad , \tag{6.20}$$

and using simple properties of the Fourier transform allows us to easily compute the emission spectrum as

$$\begin{aligned}\frac{S(\omega)}{n_{\mathrm{ss}}} &= n_{\mathrm{ss}}\frac{\gamma^2}{\Omega^2}\delta(\omega) + \frac{1}{2}\frac{\gamma_{\mathrm{dp}}+\gamma/2}{\omega^2+(\gamma_{\mathrm{dp}}+\gamma/2)^2} \\ &+ Re\frac{n_{\mathrm{ss}}}{\Omega^2}\left(\frac{A}{2}+\frac{B}{8i\mu}\right)\frac{1}{i(\omega-\mu)+(\gamma_{\mathrm{dp}}/2+3\gamma/4)} \\ &+ Re\frac{n_{\mathrm{ss}}}{\Omega^2}\left(\frac{A}{2}-\frac{B}{8i\mu}\right)\frac{1}{i(\omega+\mu)+(\gamma_{\mathrm{dp}}/2+3\gamma/4)} \end{aligned} \tag{6.21}$$

in the case of $\Delta = 0$. We note that ω is the observation frequency relative to the QD frequency, because we are in the rotating frame. The first term gives the coherently scattered part of the field, while the three latter terms make up the incoherently scattered contribution. The single photons coherently scattered off the two-level system inherit the coherence properties of the driving laser, and because we assumed a completely monochromatic driving field the spectrum for the coherently scattered field is a delta-function. This is of course not physical, but it serves to prove that the coherently scattered field inherits the coherence of the laser and the delta-function can to a good approximation be replaced by the actual spectral function of the laser as long as the laser is much more narrow than the QD linewidth. In the case of spontaneous decay, the upper limit for the coherence of a two-level system is given by the radiative rate, but operating in the coherently scattered regime a 30-fold increase in the coherence has been observed experimentally [135].

The incoherently scattered part of the field is given by the last three terms in Eq. (6.21), where the first of these terms gives a central peak and the two last terms give peaks at $\pm\mu$. In Fig. 6.4(a) the emission spectra are plotted as a function of the amplitude of the driving field Ω and in Fig. 6.4(b) the spectra at three different powers representing very different regimes are shown. As discussed, at low powers the coherently scattered field dominates and the emission spectra inherits the linewidth of the excitation laser. In order to be able to plot the spectrum we have assumed the laser to be given by a Lorentzian with a very narrow full-width at half-maximum (FWHM) of $10^{-3}\gamma$. When increasing Ω the incoherently scattered field begins to contribute significantly to the total field, which is seen in Fig. 6.4(b) for $\Omega = \gamma$ as a broad contribution to the central peak and the overall intensity has gone up. In this case the central

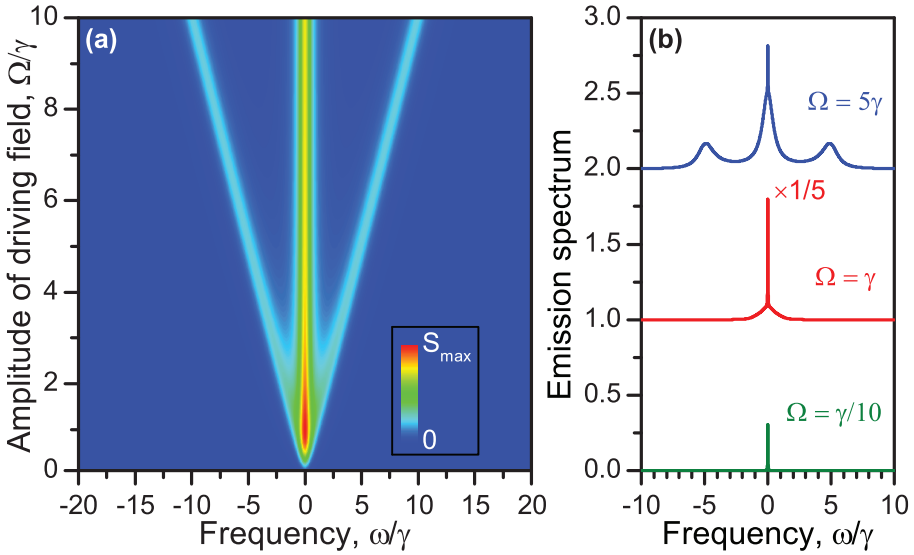

Figure 6.4: Emission spectra calculated with $\Delta = 0$ and $\gamma_{\rm dp} = 0$. **a)** While the coherent part dominates the spectrum at very low values of ω, the incoherent part has become significant already at $\Omega = \gamma$. As Ω increases, Mollow triplets become clear and they split linearly as a function of Ω. **b)** Spectra at three powers showing very different regimes. For $\Omega = \gamma/10$ the coherent part dominates and the spectrum has the linewidth of the laser. For $\Omega = \gamma$ the incoherent part has become significant and appear as a broadening of the central peak. When $\Omega = 5\gamma$ the incoherent part dominates completely and Mollow triplets appear due to the dressing of the QD levels with the driving laser. For clarity the spectra are offset vertically and the spectrum for $\Omega = \gamma$ is scaled down by a factor of 5.

peak consists of the sum of the first and second term in Eq. (6.21), where the former coherent part is given by the delta-function and the latter incoherent part is a Lorentzian with a width of $(\gamma + 2\gamma_{\rm dp})$. The relative amount of incoherent field increases as the population of the QD becomes non-negligible. As Ω is increased even further, the incoherent part dominates the central peak completely and side peaks appear. These three peaks are known as Mollow triplets [75] and can be seen in Fig. 6.4(b) for $\Omega = 5\gamma$. For these values of Ω, the driving field becomes strong enough to overcome both dissipation and

decoherence, and the laser dresses the bare states of the QD. Both the excited and ground state of the QD are split into two states with the splitting μ, which allows for four transitions, where two of them are at $\omega = \pm\mu$ and two of them are degenerate at $\omega = 0$. As a result the spectrum in Fig. 6.4(b) contains three peaks, and the splitting between them increases linearly with Ω.

Coherent and incoherent scattering

The transition from predominantly coherent to incoherent scattering can be quantified by considering their respective contributions to the total intensity of the emitted field, which can be be expressed as the integral over the entire spectrum

$$I = I_{\mathrm{coh}} + I_{\mathrm{inc}} = \alpha \int_{-\infty}^{\infty} S(\omega) d\omega = \alpha n_{\mathrm{ss}} \quad , \tag{6.22}$$

where α is a proportionality constant. We have used the fact that the total intensity can viewed simply as the steady state population of the QD. The coherent spectrum is given by the first term in Eq. (6.21) and the intensity is easily found to be

$$I_{\mathrm{coh}} = \alpha \int_{-\infty}^{\infty} n_{\mathrm{ss}}^2 \frac{\gamma^2}{\Omega^2} \delta(\omega) d\omega = \alpha n_{\mathrm{ss}}^2 \frac{\gamma^2}{\Omega^2} = \alpha \frac{\gamma^2 \Omega^2}{(\gamma^2 + 2\gamma\gamma_{\mathrm{dp}} + 2\Omega^2)^2} \quad , \tag{6.23}$$

and the intensity of the incoherent part is found as the difference

$$I_{\mathrm{inc}} = I - I_{\mathrm{coh}} = \alpha n_{\mathrm{ss}} \left(1 - n_{\mathrm{ss}} \frac{\gamma^2}{\Omega^2} \right) = \alpha \frac{\Omega^2 (2\gamma\gamma_{\mathrm{dp}} + 2\Omega^2)}{(\gamma^2 + 2\gamma\gamma_{\mathrm{dp}} + 2\Omega^2)^2} \quad . \tag{6.24}$$

We recall that the intensity of the driving field is proportional to Ω^2, and in Fig. 6.5 the intensities of both the coherent and incoherent parts are plotted as well as the total intensity as a function of pump intensity. For small values of Ω^2 the coherent part dominates and increases linearly with pump intensity until it reaches saturation, whereafter it decreases again. The incoherent part increases parabolically until eventually reaching saturation. The intensities of the coherent and incoherent parts are equal at $\Omega^2 = \gamma(\gamma/2 - \gamma_{\mathrm{dp}})$, where the steady state population has reached the value of $n_{\mathrm{ss}} = (1 - 2\gamma_{\mathrm{dp}}/\gamma)/4$. We immediately note that increasing dephasing will cause this cross-over to occur at lower pump intensities. The ratio between the two contributions yields

$$\frac{I_{\mathrm{coh}}}{I_{\mathrm{inc}}} = \frac{\gamma^2}{2(\gamma\gamma_{\mathrm{dp}} + \Omega^2)} \quad . \tag{6.25}$$

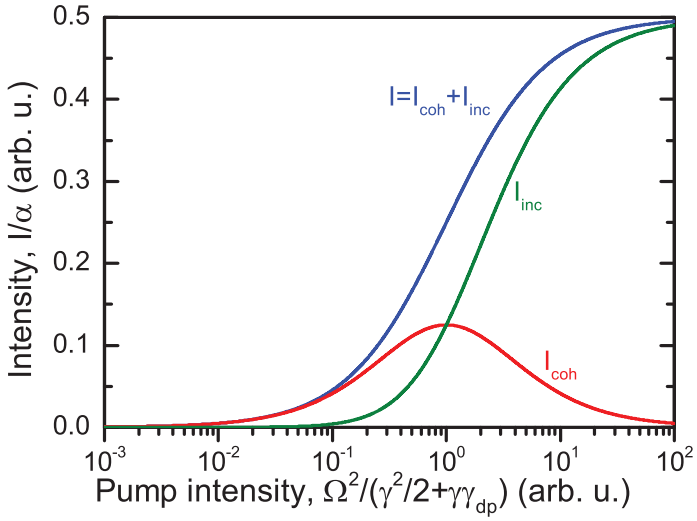

Figure 6.5: The intensity of the coherently and incoherently scattered parts of the field together with the total intensity for $\gamma_{dp} = \Delta = 0$. At low powers the coherent part dominates until it reaches saturation at $\Omega^2 = \gamma(\gamma/2 - \gamma_{\rm dp})$, after which it decreases again. Meanwhile the incoherent part increases and completely dominates the total intensity for large values of Ω^2.

As observed in Fig. 6.5, the relative contribution of the coherently scattered field decreases with increasing pump intensity. In the limit of low pump intensity we obtain

$$\frac{I_{\rm coh}}{I_{\rm inc}} = \frac{\gamma}{2\gamma_{\rm dp}} \quad , \tag{6.26}$$

from which we see that the deteriorating effect of dephasing cannot be compensated for by decreasing pump intensity. However, in recent experimental work dephasing was found not to be very significant, and the coherently scattered part of the field was clearly observed [135].

6.2 Pulsed resonant excitation

In the previous section we considered only CW excitation, where single photons were generated but at random times. However, in order to generate single

photons on-demand we need to prepare the QD deterministically in the excited state, which we in the following demonstrate is possible by exciting the QD with a pulse. The equations of motion for pulsed excitation are the same as Eq. (6.3) derived for resonance fluorescence just with a time dependence on the driving field, i.e.

$$\Omega(t) = \frac{\Theta}{\sqrt{\pi}\sigma} \mathrm{e}^{-(t-t_0)^2/\sigma^2} \quad , \tag{6.27}$$

where the excitation pulse shape has been assumed gaussian with the temporal width of the pulse 2σ. The time offset, t_0, denotes the center of the pulse and assuming that the amplitude of the driving field is negligible at $t = 0$, then $\Theta = \int_0^\infty \Omega(t)dt$ is the pulse area. In shorthand we write Eq. (6.3) as

$$\dot{\rho}_{\mathrm{v}}(t) = \mathbf{M}(t)\rho_{\mathrm{v}}(t) \quad , \tag{6.28}$$

and the solution can then be written

$$\rho_{\mathrm{v}}(t) = \mathbf{\Phi}(t)\rho_{\mathrm{v}}(t=0) \quad , \text{ where } \quad \mathbf{\Phi}(t) = \mathrm{e}^{\int_0^t \mathbf{M}(\tau)d\tau} \quad , \tag{6.29}$$

if and only if $[\mathbf{M}(t), \mathbf{\Phi}(t)] = 0$. This condition is found to only be fulfilled on resonance and when dissipation and decoherence is not included, i.e. $\gamma = \gamma_{\mathrm{dp}} = \Delta = 0$ and for simplicity we first consider this case. We find that

$$\mathbf{\Phi}(t) = \begin{pmatrix} \cos(\theta(t)/2)^2 & \frac{i}{2}\sin(\theta(t)) & -\frac{i}{2}\sin(\theta(t)) & \sin(\theta(t)/2)^2 \\ \frac{i}{2}\sin(\theta(t)) & \cos(\theta(t)/2)^2 & \sin(\theta(t)/2)^2 & -\frac{i}{2}\sin(\theta(t)) \\ -\frac{i}{2}\sin(\theta(t)) & \sin(\theta(t)/2)^2 & \cos(\theta(t)/2)^2 & \frac{i}{2}\sin(\theta(t)) \\ \sin(\theta(t)/2)^2 & -\frac{i}{2}\sin(\theta(t)) & \frac{i}{2}\sin(\theta(t)) & \cos(\theta(t)/2)^2 \end{pmatrix} \quad , \tag{6.30}$$

with the time varying quantity defined as

$$\theta(t) = \frac{\Theta}{2}\left(erf\left(\frac{t-t_0}{\sigma}\right) + erf\left(\frac{t_0}{\sigma}\right)\right) \quad , \tag{6.31}$$

where $erf(t)$ is the error function occurring when integrating a normal distribution from zero to time t. At initial times the QD is in its ground state, and we thus find the following expression for the population of the excited state

$$\rho_{11}(t) = \sin^2(\theta(t)/2) \quad . \tag{6.32}$$

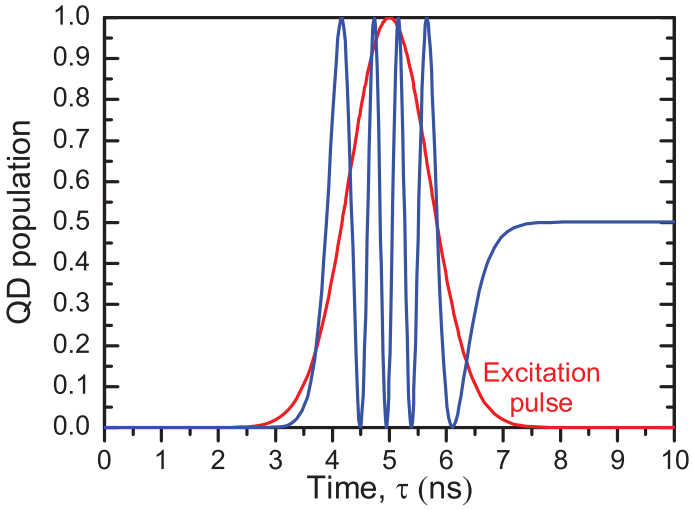

Figure 6.6: Population of the excited state of the QD as a function of time for $\gamma = \gamma_{\mathrm{dp}} = \Delta = 0$, $\Theta = 17 \cdot \frac{\pi}{2}$, $t_0 = 5$ ns, and $\sigma = 1$ ns. For reference the excitation pulse with an amplitude normalized to unity is also plotted.

Using this expression the population of the excited state in the QD is plotted in Fig. 6.6 as a function of time, and for reference the excitation pulse with an amplitude normalized to unity is also plotted. As expected the population remains zero until the pulse arrives, whereafter it increases and begins to oscillate. The oscillations become faster as the pulse amplitude increases and when the pulse amplitude decreases again then the oscillations slow down again. Finally the population levels off at a fixed population, from where it does not decay because we have set dissipation to zero. By taking the long-time limit in Eq. (6.31) we obtain that $\theta(t \gg \{t_0, \sigma\}) = \Theta$, where Θ is the pulse area. We thus see that the final population of the QD varies as $\sin^2(\Theta/2)$, which is plotted in Fig. 6.7. A pulse with $\Theta = \pi$, also known as a π-pulse, thus leaves the QD in an excited state and choosing the pulse area correctly makes it possible to prepare the QD in any superposition of excited and ground state. This behavior has also been observed experimentally [138, 132], where dissipation, however, changes the picture as we shall see now.

We now include both dissipation and decoherence and solve the equations numerically. The population is plotted as a function of time in the case of both

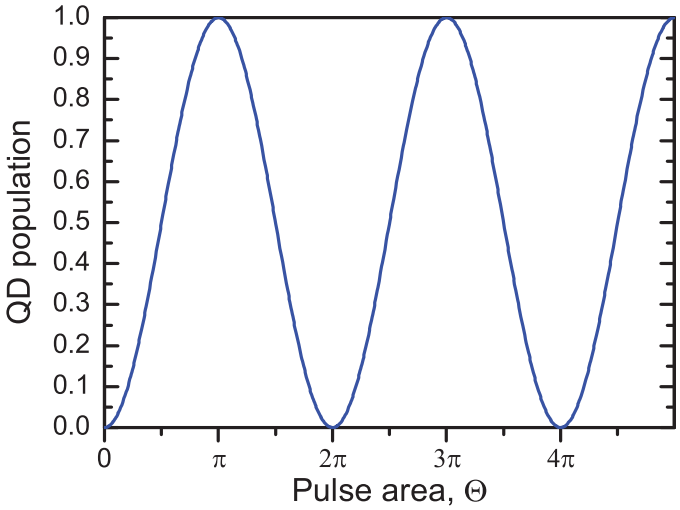

Figure 6.7: Steady state population of the excited state of the QD as a function of pulse area with $\gamma = \gamma_{\mathrm{dp}} = \Delta = 0$. The steady state of the QD can thus be tailored by applying the correct pulse area, e.g., applying a π-pulse ($\Theta = \pi$) leaves the QD in the excited state.

dissipation, cf. Fig. 6.8(a), and dephasing, cf. Fig. 6.8(b). Both processes cause damping of the oscillations during the excitation pulse, while only dissipation gives rise to a population decay after the excitation pulse has disappeared. Dissipation usually causes a decay of both the population and the polarization, while decoherence only causes the latter. However, when the system is driven with a pulse, the population decay becomes less important because the excitation pulse can re-excite the QD immediately. For this reason dissipation and decoherence have the same effect on the population, namely damping the oscillations, with the only difference being that dissipation causes the otherwise steady state population to decay, as verified by Fig. 6.8. While including dephasing, $\gamma_{\mathrm{dp}} = 1\ \mathrm{ns}^{-1}$, we now calculate the steady state population as a function of pulse area, and the result is shown in Fig. 6.9. As in the case of no dephasing, the population oscillates as a function of pulse area, but dephasing causes damping of the oscillations and an increase in their period. The damping results in the population eventually reaching the steady state value 0.5, which is the same as in the case of continuous wave excitation. Experimentally

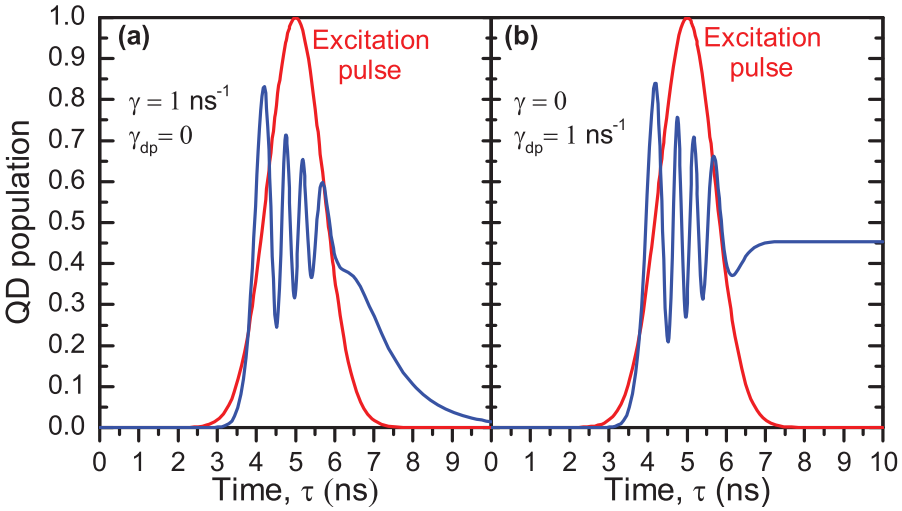

Figure 6.8: Population of the excited state of the QD as a function of time for $\Theta = 17 \cdot \frac{\pi}{2}$, $t_0 = 5$ ns, $\Delta = 0$, and $\sigma = 1$ ns. **a)** Dissipation damps the oscillations and causes a decay of population once the excitation pulse has disappeared. **b)** Decoherence also damps the oscillations but does not give rise to a population decay.

the damping shown in Fig. 6.9 has been observed [139], but the period of the oscillation were seen to increase with the spectral FWHM of the excitation pulse, which was attributed excitation-induced dephasing. Acoustic phonons could be identified as the principal source of this excitation-induced dephasing. Later work showed that the period of the oscillations also increased with temperature and comparison to a model that takes the interaction between electrons and longitudinal acoustic phonons into account showed a very good agreement [114]. The aforementioned model bares strong resemblances to the model we described in chapter 4. The increase in period with temperature was shown to be due to the phonon-induced renormalization of the Rabi frequency.

Recent measurements have used resonant excitation to prepare the QD in an excited state and measured the indistinguishability of the emitted photons to an impressive 97% [119], where the extracted dephasing rate was found to be very low, $\hbar\gamma_{\mathrm{dp}} = 0.12$ μeV indicating that resonant excitation might reduce

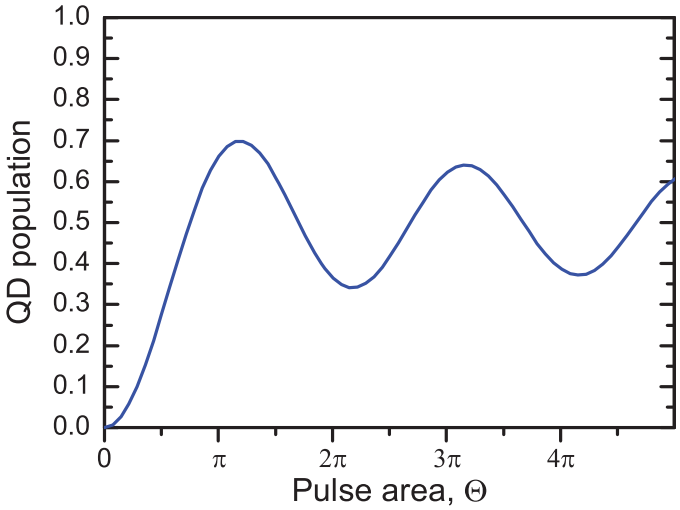

Figure 6.9: Steady state population of the excited state of the QD as a function of pulse area with $\gamma_{\mathrm{dp}} = 1$ ns^{-1} and $\gamma = \Delta = 0$. Dephasing damps the oscillations and increases the period slightly.

the very fast dephasing. Furthermore, the deterministic preparation of the QD in the excited state leads to the elimination of the jitter on the excitation time that occurs under non-resonant excitation. This time-jitter causes additional dephasing and resonant excitation thus eliminates this source of dephasing.

6.3 Experimental setup

A new experimental setup has been build for the purpose of resonant excitation of a single QD in a photonic-crystal membrane, and in the following all of the essential components are described. It will also be outlined how measurements are performed and an example of resonant excitation of a QD will be shown.

6.3.1 Cryostat

The cryostat used in this setup is a AttoDry500 cryostat, which is a Cryostation from Montana Instruments customized by AttoCube Systems so that small and high-precision piezo-stages can be fitted inside the cryostat. The cryostat is a closed-cycle cryogen-free cryostat, which means that a fixed amount of helium is circulated around in the cryostat and used for cooling. Complete details on the cooling mechanism in the cryostation are not revealed by Montana Instruments as they have a patent pending, but the main principle behind the cooling of the cryostat is a Gifford-McMahon cryocooler. The working principle, which is not much different from that of a standard refrigerator, is that helium gas is let into a displacer, where it is expanded causing the pressure and thus temperature to drop. The displacer moves back and forth with frequency ~ 1 Hz at stable conditions, and it is connected to a compressor through both a high-pressure supply line and low-pressure exhaust line both containing helium. The compressor consumes significant amounts of energy in order to supply the high-pressure helium into the cryocooler and retract it through a low-pressure exhaust line. The cold space in the cryocooler it connected to a cold arm that goes to the sample chamber, cf. Fig. 6.10, and delivers the cooling power. In Fig. 6.10 it is illustrated how the sample chamber is connected to the cryocooler via a cold arm, and that the cryocooler is connected to the compressor via two supply lines. In addition both the cryocooler and the compressor are connected to a control unit that contains much of the electronics for controlling the system. The control unit is also connected to a laptop computer that contains the graphic user interface. Finally, the sample chamber is connected through a vacuum tube to a vacuum pump in the control unit, which ensures a low pressure before cooling is initiated. The surrounding housing of the sample chamber is made of Invar and vacuum sealing between the removable lid and the fixed bottom part is ensured by O-rings. Before cooling, the sample chamber is pumped

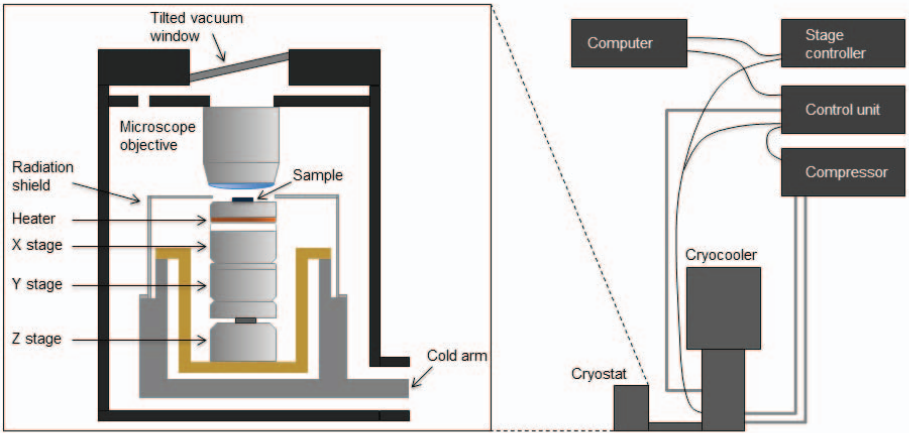

Figure 6.10: Sketch of the cryostat setup. The compressor is connected to the Gifford-McMahon cryocooler via a supply and return Helium line. The control unit contains a vacuum pump and through a connection to the cryocooler it ensures vacuum around the sample. Electronic connections make it possible to control the cooling of the cryostat and the stages from a computer. In the left part we show a zoom-in on the cryostat, where the cold arm comes from the cryocooler and the stages, sample, and radiation shield are all connected to it. The three stages are stacked on top of each other with a thermally anchored pad on top followed by a heater pad with a build-in thermometer. On top of this our sample is placed surrounded by a radiation shield that facilitates the cryo-pumping. The microscope objective is placed 1.2 mm above the sample and is at room-temperature. A tilted anti-reflection coated window ensures the vacuum. There is a small gap between this window and the top of the cryostat, and a small hole is made on the left of it to enable the pressure to equalize.

down to $\sim$ 0.13 mbar at $\sim$ 300 K, and after cooling when the temperature has reached stable conditions the pressure should drop to $\sim 1.7 \cdot 10^{-3}$ mbar following the ideal-gas law. However, at cryogenic temperatures an important effect is cryo-pumping, where gas molecules condensate on cold surfaces. In the sample chamber gas molecules condensate on e.g. the outside of the radiation shield and two adsorber towers filled with porous carbon, which allows for an even more effective cryo-pumping, bring the pressure down to $\sim 1.3 \cdot 10^{-6}$ mbar outside the radiation shield. The pressure is probably significantly lower

inside the radiation shield, where the sample is mounted. We later modified the setup to allow for the connection to a turbopump in which case we reach an initial pressure before cooling of $\sim 10^{-6}$ mbar.

In Fig. 6.10 the sample chamber is shown in more detail. The three piezo-stages are mounted on a holder that is thermally coupled to the cold arm from the cryocooler. The piezo-stages are ANP101/RES/LT from AttoCube that work on the slip-stick principle utilizing the difference in static and kinetic friction, and they have a minimum step size of ~ 10 nm at 10 K. A small variable resistor is mounted inside each of the stages, and the resistance is proportional to the position of the stages. By reading out the resistance, we can measure the position with an accuracy of ~ 200 nm. The absolute readout can thus not be used for fine-tuning of the position but works very well for larger movements. On top of the three stages a pad thermally anchored to the bottom through ultra-flexible cobber braids is mounted, and on top of that a heating pad with an integrated temperature sensor is placed for temperature control. Finally, the titanium sample holder is placed with the sample glued onto using silver glue. A radiation shield encasing the piezo-stages and sample but allowing for optical access from the top is mounted. Sample temperatures down to 6.5 K with a stability of 13 mK can be reached with the radiation shield on, as opposed to only 14 K without the radiation shield. As indicated in Fig. 6.10 the electrical connections from the stages are going to a stage controller box, ANC350/3/RES from AttoCube, which generates the voltages needed to move the stages and does the resistive read-out of the position. The stage controller is also connected to a computer from which it can be controlled.

The microscope objective, LCPLN100XIR from Olympus, has a working distance of 1.2 mm, a high numerical aperture of 0.85, and a high optical transmission of more than 80% in the range $800 - 1000$ nm. As seen in Fig. 6.10, the microscope objective is mounted on the part of the cryostat that stays at room temperature. The vacuum in the sample chamber thermally isolates the room-temperature microscope objective from the sample, which is at cryogenic temperatures. The resolution of the microscope objective was tested by inserting a test sample containing a grating with a periodicity of 5 μm. The grating was mounted at a 45° angle relative to the $x-$ and $y-$stages in order for the

measurements to include vibrations along both axes. Above the microscope objective we placed a single mode fiber and a lens in front of it to collimate the beam. Thereafter, we coupled a Helium-Neon laser at 633 nm into the fiber and measured the intensity of the light that has reflected from the sample and is coupled back into the fiber. By maximizing the intensity of the reflected light we focussed on the top of the grating structure. Using a fixed voltage per step we moved one of the piezo-stages and mapped out the grating structure as a function of steps, which allowed us to make the calibration of 146.4 nm/step using a voltage of 38 V. The grating structure we mapped out did not have very sharp edges due to the optical resolution. It took 4 steps, i.e. 585 nm, to go from 15% to 85% of the maximum intensity, which are the points corresponding to the 1σ level of a gaussian function. In this way we determined the optical resolution to 585 nm for a laser wavelength of 633 nm. Afterwards we moved the stages so that the intensity of the reflected light was half of the maximum, I_{max}. The slope at this point could be approximated by the linear expression $\alpha = I_{max}(0.85 - 0.15)/585$ nm. In a time-span of 20 s we measured peak-to-peak fluctuations of 16.7 nm, where we used the linear slope, α, to convert from intensity to spatial fluctuations. The root-mean-square of the vibrations were obtained by dividing the peak-to-peak fluctuations by $2\sqrt{2}$, and this gave 6 nm. The intensity of the emission from a single QD measured using a spectrometer and CCD maximally decreased by 50% over 24 hours without any re-alignment, which proved that long-term drifts of the sample were also not a problem.

6.3.2 Confocal microscopy setup

The optical setup around the cryostat is shown in Fig. 6.11. The excitation laser is coupled into the single-mode polarization-maintaining (PM) fiber and is exiting the fiber on the right-hand side of the figure. When exiting the fiber, the beam diverges but the lens (L1) makes the beam collimated with a diameter of 2 mm. The beam then propagates through a beam-sampler (BS1), where less than 10% is reflected. It then passes through a thin-film polarizer in order to make the beam linearly polarized before being incident on the beam-splitter (BS2) where 90% is transmitted and 10% is reflected down to the sample. The transmitted beam is incident on a photodiode, which is used for two purposes; firstly a thorough calibration using a power-meter makes it possible to use the

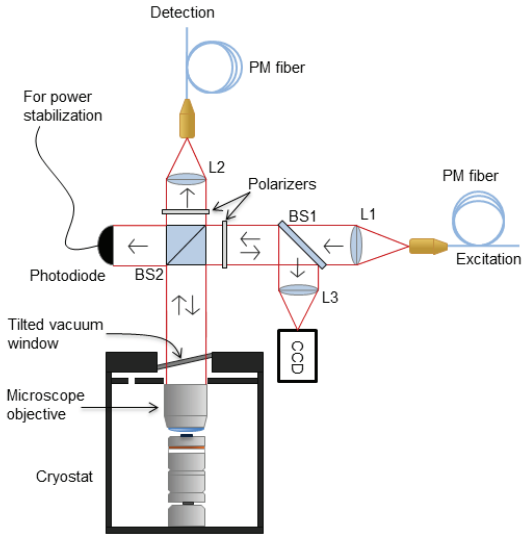

Figure 6.11: Sketch of the optical setup around the cryostat. The excitation laser is coupled out of the PM fiber and collimated to a beam diameter of 2 mm by lens (L1) before hitting a beam-sampler (BS1), which transmits more than 90% of the beam. The thin film polarizer ensures the beam is linearly polarized and the beam-splitter (BS2) reflects 10% of the laser down to the cryostat, where the vacuum window is anti-reflection coated and tilted. The 90% of the laser that is transmitted through BS2 is detected with a photodiode and the output goes to the power stabilization. The emission from the sample is collected by the microscope objective (NA=0.85) and 90% of the emission is transmitted through BS2, whereafter a linear polarization is selected and the emission coupled into a PM fiber and sent to detection. For imaging the sample, an LED centered at 850 nm is inserted before the lens L2, and the sample is imaged on the CCD-camera using the lens L3.

photodiode to measure the power, and secondly the voltage output can be connected to a PID loop for active stabilization of the power, as will be described in more detail shortly. 10% of the incident laser is reflected down towards the cryostat, where it propagates through a tilted anti-reflection coated window that ensures the vacuum before being incident on the microscope objective. The microscope objective focusses the beam onto the sample, excites the QDs,

and collects the emission from the sample. The collimated beam emerging from the microscope objective is incident on the beam-splitter (BS2), where 90% of the beam is transmitted, and the thin-film polarizer transmits only one linear polarization before the lens (L2) couples the beam into a PM-fiber, which goes to the detection part of the setup. However, 10% of the beam is reflected by the beam-splitter (BS2) and less than 10% of that beam is reflected once more by the beam-sampler (BS1) onto the lens (L3), which focusses the beam onto the CCD camera for imaging purposes. We need to image the sample in order to known where we are collecting emission from, and for this purpose we can insert an LED just in front of the detection fiber that then illuminates the sample. The center wavelength of the LED is 850 nm and the reflections from the sample are detected on the CCD, which thus enables orientation on the sample.

Through the PM fiber, the emission from the sample is sent to the detection part of the setup, where the output from the fiber is collimated with a diameter of 2.8 mm using a lens. The beam is directed onto a spectrometer followed by either an APD or a CCD-camera for time-resolved and spectroscopy measurements. However, since only a single QD is probed in resonance fluorescence a spectrometer is not needed to filter out the contributions from other QDs, and for resonance fluorescence measurements we therefore send the emission directly onto an APD. In this way we avoid the transmission losses of the spectrometer. We use the previously described APDs from Perkin Elmer that offer a high quantum efficiency at the expense of the time-resolution. The emission can also be sent to a free-space Hanbury Brown and Twiss setup, where the beam is incident on a $50:50$ beam-splitter and both the transmitted and reflected beams are sent to APDs, and the coincidence counts recorded.

Polarization extinction ratio

Because only a single QD is addressed in resonance fluorescence it is not necessary to spectrally filter emission from other QDs away. The technical challenge, however, consists in filtering the laser away from the emission since they both have the same wavelength and their optical modes have a large overlap. Filtering of the laser can be done by addressing one of the linear dipoles of the QD with a linearly polarized laser oriented at 45° with respect to the dipole. Half of the incident laser thus interacts with the dipole. In detection a polarizer

situated at $-45°$ with respect to the dipole and thus orthogonal to the excitation laser, which ensures that the excitation laser is filtered away. Only half of the emission is thus transmitted, but recent work has shown that residual laser can be suppressed by a factor of 10^7 [135]. In order to obtain such a high polarization extinction ratio we use thin-film polarizers in both the excitation and detection arm, as shown in Fig. 6.11. The extinction ratio is measured by reflecting linearly polarized laser light of the surface of the sample. The polarizer in the detection arm is now rotated and the difference between the maximum and minimum intensity of the light coupled into the PM fiber is measured to be $3.7 \cdot 10^6$. Such a high extinction ratio is only possible when the laser light is either s- or p-polarized with respect to the plate beam-splitter BS2 in Fig. 6.11. We find that it is crucial to have as few optical elements between the two polarizers as possible, and in this setup we only have a plate beam-splitter, a tilted anti-reflection coated vacuum window, and a microscope objective between the two polarizers. Because the dipoles of the QD preferably align themselves along crystal directions, we can rotate the sample in order to ensure that the excitation and detection polarizations are at $\sim 45°$ with respect to the dipoles of the QD. The high extinction ratio requires a very fine alignment, and temperature fluctuations and turbulence around the thin-film polarizers reduce the extinction ratio with more than two orders of magnitude over ~ 30 minutes. This problem was reduced by shielding the polarizers as much as possible.

6.3.3 Excitation of the quantum dot

For the theory derived in section 6.1 the excitation laser was assumed to be completely monochromatic, which of course cannot be realized experimentally. However, the theory can still be applied as long as the linewidth of the excitation laser is much narrower than the Fourier-limited linewidth of the QD. In this case $g^{(1)}(\tau)$ shown in Fig. 6.3 does not settle to a constant level but rather decays with the laser coherence time, and similarly the peak due to coherent scattering in the spectra in Fig. 6.4 is no longer a delta-function but is rather given by the linewidth of the laser [135]. Due to the inhibition of spontaneous emission in a photonic crystal the decay rate is normally below 0.1 ns^{-1} which corresponds to a Fourier-limited linewidth below 16 MHz or in energy 65 neV.

For excitation we therefore use a fiber-coupled diode laser, DL pro 940

from Toptica Photonics, which according to specifications has a linewidth of 100 kHz measured over 5 μs, but we have measured a long-term drift of more than $\sim$ 100 MHz over several hours. The laser can be tuned over the range 911 to 985 nm in a coarse manner, where the laser exhibits mode-jumps as it is scanned in wavelength. In Fig. 6.12 the optical setup for the excitation lasers is shown, and the output of the Toptica laser is sent through a half-wave plate (HWP) and a polarizing beam-splitter (PBS), where the reflected part is coupled into a fiber that goes to a wavemeter, HP Agilent 86120B, which records the wavelength of the laser. It is possible to scan the laser without any mode-hops by applying a voltage to the grating of the diode. By applying such a voltage in steps and recording the wavelength at each step using the wavemeter, we measure a typical mode-hop free tuning range of 24 GHz. Any noise on the voltage supplied to the grating will be turned into frequency noise of the laser, but we can eliminate a large part of this by inserting an electronic low-pass filter consisting of an RC-circuit with a cutoff frequency of 17 Hz. While scanning the laser, the output power changes strongly. Furthermore, the HWP and PBS in Fig. 6.12 translate polarization fluctuations into power fluctuations, and over time we observe a drift of the laser power. In order to compensate for this, we actively stabilize the power of the laser using a proportional-integral-derivative (PID) controller, where the difference between the measured and set power, $e(t)$, is calculated. The controller then tries to minimize $e(t)$ by adjusting an output variable that affects the power. The output variable depends on $e(t)$ through three terms; one that is just proportional to $e(t)$, one that is proportional to the integral of $e(t)$, and one that is proportional to the derivative of $e(t)$.

In our case the optical power is measured by the photodiode after the 90/10 beam-splitter in Fig. 6.11, which gives an output voltage that is sent to the PID loop. From the computer we set the desired optical power, which through a calibration is converted to the corresponding voltage and sent to the PID loop. The difference between the measured and set voltage is $e(t)$, which the PID loop minimizes by adjusting the optical power using an acousto-optic modulator (AOM), AOM 3080-125 with the driver 1080AF-AIFO-2.0 both from Crystal Technology. The AOM operates by using a piezoelectric transducer to create acoustic waves in glass (TeO_2) at 80 MHz. This causes the optical beam to be diffracted into the first order diffraction mode, and the amplitude of the

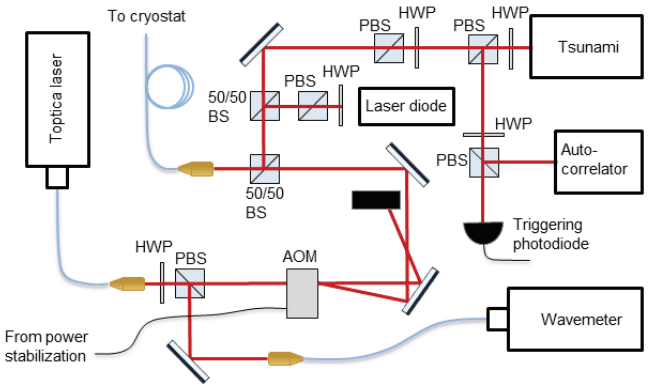

Figure 6.12: Sketch of the optical setup for the excitation lasers. The fiber-coupled tunable Toptica laser is used for resonant excitation, while the tunable pulsed Tsunami laser is primarily used for lifetime measurements, and the laser diode at 780 nm is used for fast characterizations. The Toptica laser passes through an AOM, where the first order diffracted beam is coupled into the fiber going to the cryostat. By connecting the AOM to a PID loop we can actively stabilize the power of the laser and part of the beam is sent to a wavemeter that measures the wavelength. Sets of half-wave plates (HWP) and polarizing beam-splitters (PBS) are used to control the power of the Tsunami and laser diode. Part of the Tsunami beam is sent to an autocorrelator for checking that it is pulsing, and part of it is sent to the triggering diode used for lifetime measurements.

diffracted beam depends on the amplitude of the acoustic wave.

In Fig. 6.12 the optical setup is shown, where the Toptica laser propagates through the AOM, and the first order diffracted beam is coupled into the fiber going to the cryostat, while the zeroth order diffracted beam is blocked. The output of the PID loop is connected to the driver of the AOM, which controls the amplitude of the acoustic wave, and in this way the PID stabilizes the power that is transmitted through the 90/10 beam-splitter in Fig. 6.11. By measuring the intensity fluctuations of the beam reflected from the 90/10 beam-splitter we constantly achieve standard deviations below 1% of the total intensity. We chose to place the photodiode for power stabilization as close to the sample as possible to minimize any intensity fluctuations of the excitation laser at the

position of the sample. An additional advantage of the power stabilization is that it also allows for automatic power control and, e.g., power series are thus automated.

In order to perform time-resolved measurements we have included the option of exciting the sample with a pulsed tunable Ti:Sapph laser, Tsunami from Spectra-Physics, which has a 3 ps pulse duration and a repetition rate of 80 MHz. As shown in Fig. 6.12, the output of the Tsunami laser is directed through two sets of HWP and PBS, where the beam reflected from the first PBS is sent toward an autocorrelator, Mini from A.P.E. , and a fast triggering diode. The second set of HWP and PBS is used for controlling the power that is sent to the sample. An additional set of HWP and PBS distributes the power between the autocorrelator used for monitoring that the Tsunami is pulsing and the fast triggering diode used for lifetime measurements. Finally, a small CW laser diode at 780 nm is also coupled into the fiber and is primarily used for alignment purposes in order to avoid having to turn on the Tsunami laser.

6.4 Measurements

The sample with photonic-crystal membranes that we use for resonance fluorescence is the same sample that we used for cavity quantum electrodynamics in the previous chapter. The sample contains photonic-crystal membranes both with and without L3 cavities, and we only use the latter structures, where the spontaneous decay rate is inhibited. For investigations of a single QD we need to locate an exciton emission line that is well separated from other QDs. Because the sample has a relatively high density of QDs, $\sim 80\ \mu\text{m}^{-2}$, we search for QDs at long wavelengths, ~ 950 nm, compared to the center of the distribution. When searching for suitable QDs we observe the emission on the spectrometer under above-band excitation. After locating the QD we tune the Toptica laser close to the resonance and optimize the extinction ratio under slightly detuned conditions. We then scan the laser across the resonance in small wavelength steps, while recording the emission from the sample on an APD and the wavelength of the laser for each step to ensure the tuning is mode-hop free. During scanning, power stabilization is used and the power is recorded to ensure that it works correctly. However, when using this approach we encounter the severe problem that the polarization extinction ratio varies strongly with wavelength.

The recorded signal is thus dominated by the reflection of the laser instead of emission from the QD, and the extinction ratio easily decreases by a factor of 25 over 20 GHz.

Such measurement have been performed successfully by other groups, but there are crucial differences. In [133], the geometry allowed for orthogonal excitation and detection which made the polarization extinction ratio unnecessary. In [135], cross-polarized confocal microscopy was also used, but instead of scanning the excitation laser, the QD transition was scanned using the DC Stark effect. The obvious advantage of scanning the QD transition energy instead of the excitation laser is that the extinction ratio can be optimized at a fixed wavelength, and the QD can subsequently be scanned across the resonance. Unfortunately we have neither electrically tunable samples nor the possibility of applying high magnetic fields, which would otherwise make it possible to tune the transition energy of the QD.

In order to circumvent this problem we plan to use a scanning Fabry-Perot to determine the QD transition energy and subsequently set the laser to the same wavelength thus ensuring the two are on resonance. However, the QD transition energy shifts slightly depending on the excitation method, e.g., we observe a QD shift of ~ 0.1 nm when changing from above-band to wetting-layer excitation, which we attribute to the excitation of more carriers under above-band excitation and their subsequent Coulomb shifts of the QD. Unfortunately we did not have access to a Fabry-Perot at the time of the measurements and instead we used a more crude method, where we set the excitation laser to resonance with the QD by overlapping the two on the spectrometer. This is done under wetting-layer excitation of the QD since the transition energy is not expected to be very different compared to resonant excitation. Once this is done we optimize the polarization extinction ratio. However, this requires that we minimize only the reflected laser light, and we thus need to shift the QD frequency away in order to make sure that there is no emission from the QD. This is done by applying a strong above-band laser, which shifts the QD ~ 0.1 nm away while we optimize the extinction ratio. Afterwards, we only send the Toptica laser to the sample and record the second order correlation function, $g^{(2)}(\tau)$, and in Fig. 6.13 an example of such a measurement is shown together with a reference measurements. The reference measurement is done

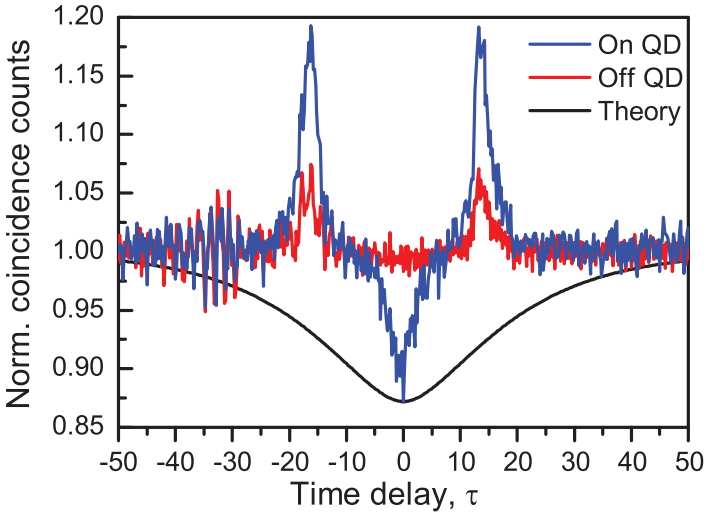

Figure 6.13: Normalized coincidence counts as a function of time delay. The reference measurement "off QD" is taken under large detunings, and two peaks due to flashing of the QDs are visible in both measurements. A dip at zero time delay is visible in the measurement on the QD, but the dip does not extend all the way to zero due to laser scattering. Theory is calculated using Eq. (6.12) with $\gamma = 0.14$ ns^{-1} as determined by lifetime measurements and with Δ, γ_{dp}, and Ω set to zero. An inhomogeneous part is added for the comparison, and the dip in the experimental data is much narrower than the theoretical one indicating that we are not in the very low power regime and that dephasing is not negligible.

under large detuned conditions, and the two peaks are due to flashing of the APDs, which is the emission of a photon from the APD chip shortly after the absorption of an incoming photon. The flashing of one of the APDs in the HBT setup can result in a backwards propagating photon in nearly the same optical mode as the emission and can thus give rise to a detection event on the other APD. The flashing peaks are at around ± 15 ns, which translates into a path length from one APD to the other of ~ 4.5 m. The flashing peaks are present in both measurements in Fig. 6.13, and they can be strongly reduced by inserting band-pass filters, but these also reduce the count-rates.

In Fig. 6.13 we observe a dip in $g^{(2)}(\tau)$-function as expected from the theory,

cf. Fig. 6.2, but the dip does not extend all the way to zero due to laser scattering but rather reaches the value $g^{(2)}(0) = 0.87$. By expressing the total intensity of the detected light as $I = I_{\mathrm{qd}} + I_{\mathrm{la}}$, where the latter part is due to laser scattering, we can perform the same type of calculations as we did in section 3.1.4. Assuming that incoherent scattering is dominating the emission, i.e. that the laser is uncorrelated with the QD emission, we derive that the laser constitutes $(1 - \sqrt{1 - g^{(2)}(0)})$ of the total intensity, which we evaluate to 64%.

Independently we measure the decay rate of the QD to $\gamma = 0.14$ ns^{-1} by exciting the QD with a 20 MHz repetition rate pulsed above-band laser diode, PDL 800-B from Picoharp. The low repetition rate is needed because the QD has a strongly inhibited decay rate. Although we have determined γ, we do not have any independent measures of the other parameters entering the theoretical expression in Eq. (6.12), but by assuming the other parameters Δ, γ_{dp}, and Ω to be zero we obtain the theoretical curve shown in Fig. 6.13, where we have added a laser contribution of 64% for the comparison to experiment. The theory has a much wider dip than the experimental data.

Increasing Ω while maintaining $\gamma_{\mathrm{dp}} = 0$ to the point where the width of dip is in agreement with experiment results in large oscillations of the function, which are not visible in the data. This indicates that γ_{dp} is not negligible for this QD, but with the data at hand we cannot determine the value quantitatively. In order to examine this in more detail we first need to decrease the amount of laser scattering, which a lower value of the dip would be evidence of. As already mentioned, we plan to use a scanning Fabry-Perot to ensure resonance of the excitation and QD and thus a better signal-to-background ratio. Secondly, we plan to scan the laser across the QD resonance, while performing differential reflection measurements [140]. In that type of measurements the Toptica laser is frequency-scanned in steps while a strong above-band laser is modulated by a chopper wheel and is exciting the QD. The emission and any residual laser scattering from the sample is detected on a photodiode and sent to a lock-in amplifier that also has an input from the chopper wheel. The strong above-band laser shifts the QD far away from the laser. In the time the above-band laser is on, the signal measured on the photodiode is thus only reflected laser light. During the time the above-band laser is blocked, the interference between the reflected laser light and the coherently scattered light is measured. In a

differential reflection measurement the difference between these two signals is measured. Because differential reflection relies on the difference between the two signals, it does not depend on the polarization extinction ratio. In this way we might be able to circumvent the problem of the strongly wavelength-dependent polarization extinction ratio.

6.5 Conclusion and outlook

In conclusion we have derived the theory for resonance fluorescence, where a monochromatic laser is incident on a two-level system. The quantities relevant for experiments have been calculated, and we have shown that a coherently and an incoherently scattered part of the field results from the resonant excitation. The coherent part dominates at low excitation powers and it inherits its coherence properties from the laser while remaining anti-bunched. The incoherent part dominates at high powers and eventually the two-level system becomes dressed by the laser, which gives rise to Mollow triplets in the spectrum. The distinction can be made that the coherent part consists of single photons that scatter off the two-level system without populating it notably, while the incoherent part relies on absorption and emission of single photons. Similarly the theory for pulsed resonant excitation was derived, and we showed how the QD can be prepared in any superposition of the excited and ground by applying the correct pulse area.

The experimental setup for resonance fluorescence was described in detail with a special emphasis on the cryostat and the polarization extinction ratio since they have posed the largest experimental challenges. A successful measurement of resonance fluorescence was shown, where a correlation measurement showed the expected anti-bunching although laser scattering was found to make up 64% of the detected signal. We found it to be a severe limitation that the polarization extinction ratio depends strongly on the wavelength, but several suggestions were made to work around this obstacle. Namely a scanning Fabry-Perot can be used to ensure resonance between the excitation laser and the QD transition, and differential reflection can be employed to measure the coherently scattered part of the field.

Finally, as this is work in progress and much time was devoted to setting up the cryostat and building the optical setup there was no time to explore pulsed

resonant excitation. For CW excitation it poses an experimental challenge to ensure that the excitation laser is on resonance with a QD in a photonic-crystal membrane or to precisely determine the detuning, because the inhibited decay rate makes the Fourier-limited linewidth of the QD narrow with values below 16 MHz. However, under pulsed excitation the short pulse duration of ~ 3 ps for our pulsed Ti:Sapph laser makes the laser spectrally much wider (~ 150 GHz) than the QD and the effect of a small detuning becomes much less critical.

While the incoherent properties of QDs in photonic-crystal membranes, e.g. the decay rates, have been widely studied, details on their coherent properties are largely unknown. Rather surprisingly it was demonstrated in chapter 4 that the longitudinal acoustic phonons interacting with the QD in an L3 photonic-crystal cavity could be described as bulk phonons in GaAs. In chapter 5 it was demonstrated that the dephasing also depends on the excitation mechanism, and in this respect resonant excitation provides us with an exceptional tool to investigate the dephasing mechanisms without any excitation-induced dephasing. If we think of dephasing as a "shaking" of the QD transition energy, then resonant excitation might help us understand whether this "shaking" only occurs when an exciton is present, which is the case for the pure dephasing model, or whether the "shaking" occurs even if there is no exciton present, thus giving rise to an "intrinsic" dephasing as opposed to an excitation-induced dephasing.

Furthermore, we can use spectral measurements to study the local optical environment (LDOS), which is strongly modified in the photonic crystal. Strong variations in the LDOS can give rise to non-Markovian dynamics that can be resolved temporally by measuring the first order coherence. Finally, resonant excitation opens for the possibility to perform heterodyne measurements that can be used to study, e.g. collapses and revivals of quantum oscillations of a QD in a photonic-crystal cavity.

Chapter 7

Conclusion

In this thesis the coherent dynamics of QDs embedded in photonic-crystal cavities have been investigated. The properties of a QD is determined by the nanophotonic environment, which primarily alters the incoherent dynamics for the light-matter couplings strengths considered in this work, and by the interaction with the solid-state environment, which primarily gives rise to dephasing. The investigation has been carried out by studying systems, where the nanophotonic environment was engineered to give rise to a strong enhancement of the light-matter interaction, and also by studying different excitation methods, which allowed us to probe the solid-state environment of the QD.

In a micropillar cavity we found the enhancement of the light-matter interaction to be so strong that not only was the decay of the QD Purcell enhanced but it also exhibited non-Markovian decay dynamics. This occurred because the cavity was not just an efficient decay channel for the QD but actually exerted back-action onto the QD, thus making the decay process memory dependent. To our knowledge this provides the first experimental demonstration of non-Markovian dynamics in solid-state cavity quantum electrodynamics, and by independently measuring all the parameters we were able to show an excellent agreement with the Jaynes-Cummings model.

Studies of a QD with a small coupling to a low-Q mode of a photonic-crystal cavity enabled the investigation of the solid-state environment. The emission from the QD was collected with an efficiency at the first lens of $(44.3 \pm 2.1)\%$, and the emission retained its single-photon nature when excited far above sat-

uration. We were able to excite the system very efficiently by tuning the laser to a 2 longitudinal optical (LO) phonon resonance, where an exciton is created in the s-shell, and the residual energy is emitted as 2 LO phonons. Similarly we demonstrated excitation mediated by longitudinal acoustic (LA) phonons, where the residual energy is emitted as single LA phonons. Importantly both the 2 LO phonon resonance and the LA phonon continuum were lying within a cavity mode, which was crucial in making this type of excitation possible. Performing indistinguishability measurements under both LO and LA phonon-mediated excitation made it possible to extract the corresponding pure dephasing rates that were found to be surprisingly low. A significant decrease in dephasing rates were observed when shifting from LO to LA phonon-mediated excitation, which highlights the importance of excitation for the generation of coherent single photons. The decrease in dephasing is attributed to the significantly smaller amount of energy emitted into the lattice under LA phonon-mediated excitation.

We also studied a single QD in a high-Q photonic-crystal cavity, where a fascinating interplay between the nanophotonic and solid-state environment was found. On resonance the QD decays with a strongly Purcell enhanced decay rate due to the strong modification of the light-matter interaction. However, the Purcell enhancement is much more broadband than expected from the Jaynes-Cummings model, and we model the data successfully with a microscopic theory that takes the non-Markovian interaction with LA phonons into account. The broadband enhancement occurs because LA phonons can assist the QD in decaying into the cavity mode by either absorbing or emitting LA phonons with the energy corresponding to the QD-cavity detuning. Using the model we were able to extract the effective phonon density of states, which holds all the information on how phonons can assist in optical recombinations. A cut-off was observed when the wavelength of the phonons became comparable to the size of the exciton wavefunctions. Remarkably, the effective phonon density of states could be modeled by a theory assuming bulk phonons in GaAs despite the strong inhomogeneity of the structure, and this rules out localization of LA phonons in the cavity at the energies considered here.

The studies performed in this thesis provide a detailed insight on the solid-state environment that the QD is embedded in, and how this affects the optical properties of the QD. The low dephasing rates combined with the high

collection efficiency are promising for applications relying on single-photons on-demand, and by taking advantage of the strong Purcell enhancement in a cavity, a high degree of indistinguishability can be reached. Similar or even lower dephasing rates are expected under resonant excitation, which has also been pursued in this thesis, but no conclusive results were obtained. This thesis constitutes a step towards understanding and potentially controlling the coherence properties of quantum electrodynamics systems based on quantum dots, which is required for all-solid-state quantum-information processing. Finally, the observed interplay between the solid-state and nanophotonic environment provides a fascinating combination of different areas of physics, which may be utilized in, e.g., the emerging field of quantum optomechanics.

Bibliography

[1] J. Raimond, M. Brune and S. Haroche. *Manipulating quantum entanglement with atoms and photons in a cavity.* Reviews of Modern Physics **73**, 565 (2001).

[2] A. Einstein, B. Podolsky and N. Rosen. *Can Quantum-Mechanical Description of Physical Reality Be Considered Complete?* Physical Review **47**, 777 (1935).

[3] J. Bell. *On the Problem of Hidden Variables in Quantum Mechanics.* Reviews of Modern Physics **38**, 447 (1966).

[4] A. Aspect, P. Grangier and G. Roger. *Experimental Tests of Realistic Local Theories via Bell's Theorem.* Physical Review Letters **47**, 460 (1981).

[5] C. H. Bennett and G. Brassard. *Quantum Cryptography: Public key distribution and coin tossing.* In *Proceedings of the IEEE International Conference on Computers, Systems and Signal Processing*, pp. 175–179 (IEEE, New York, Bangalore, India, 1984).

[6] E. Knill, R. Laflamme and G. J. Milburn. *A scheme for efficient quantum computation with linear optics.* Nature **409**, 46 (2001).

[7] A. Faraon, I. Fushman, D. Englund, N. Stoltz, P. Petroff *et al. Coherent generation of non-classical light on a chip via photon-induced tunnelling and blockade.* Nature Physics **4**, 859 (2008).

[8] D. E. Chang, A. S. Sørensen, E. A. Demler and M. D. Lukin. *A single-photon transistor using nanoscale surface plasmons.* Nature Physics **3**, 807 (2007).

[9] T. J. Kippenberg and K. J. Vahala. *Cavity optomechanics: back-action at the mesoscale.* Science (New York, N.Y.) **321**, 1172 (2008).

[10] N. Gisin, G. Ribordy, W. Tittel and H. Zbinden. *Quantum cryptography.* Reviews of Modern Physics **74**, 145 (2002).

[11] H. Kimble, M. Dagenais and L. Mandel. *Photon Antibunching in Resonance Fluorescence.* Physical Review Letters **39**, 691 (1977).

[12] F. Diedrich and H. Walther. *Nonclassical radiation of a single stored ion.* Physical Review Letters **58**, 203 (1987).

[13] T. Basché, W. Moerner, M. Orrit and H. Talon. *Photon antibunching in the fluorescence of a single dye molecule trapped in a solid.* Physical Review Letters **69**, 1516 (1992).

[14] C. Kurtsiefer, S. Mayer, P. Zarda and H. Weinfurter. *Stable Solid-State Source of Single Photons.* Physical Review Letters **85**, 290 (2000).

[15] R. Brouri, A. Beveratos, J.-P. Poizat and P. Grangier. *Photon antibunching in the fluorescence of individual color centers in diamond.* Optics Letters **25**, 1294 (2000).

[16] P. Michler, A. Imamoglu, M. Mason, P. Carson, G. Strouse *et al. Quantum correlation among photons from a single quantum dot at room temperature.* Nature **406**, 968 (2000).

[17] P. Michler, A. Kiraz, C. Becher, W. V. Schoenfeld, P. M. Petroff *et al. A quantum dot single-photon turnstile device.* Science (New York, N.Y.) **290**, 2282 (2000).

[18] D. Loss and D. DiVincenzo. *Quantum computation with quantum dots.* Physical Review A **57**, 120 (1998).

[19] P. Kok, K. Nemoto, T. C. Ralph, J. P. Dowling and G. J. Milburn. *Linear optical quantum computing with photonic qubits.* Reviews of Modern Physics **79**, 135 (2007).

[20] S. L. Chuang. *Physics of optoelectronic devices* (John Wiley & Sons, Inc., New York, 1995).

[21] L. Ibach and H. Lüth. *Solid-State Physics* (Springer-Verlag Berlin Heidelberg, 2003), third edition.

[22] M. I. Dyakonov. *Spin physics in semiconductors* (Springer Berlin Heidelberg, 2008).

[23] M. Fox. *Quantum Optics* (Oxford University Press, 2006).

[24] M. Bayer, G. Ortner, O. Stern, A. Kuther, A. Gorbunov *et al. Fine structure of neutral and charged excitons in self-assembled In(Ga)As/(Al)GaAs quantum dots.* Physical Review B **65**, 195315 (2002).

[25] L. A. Coldren and S. W. Corzine. *Diode Lasers and Photonic Integrated Circuits* (John Wiley & Sons, Inc., 1995).

[26] L. E. Ballentine. *Quantum Mechanics* (World Scientific, Singapore, 2003).

[27] Q. Wang, S. Stobbe, H. Thyrrestrup, H. Hofmann, M. Kamp *et al. Highly anisotropic decay rates of single quantum dots in photonic crystal membranes.* Optics letters **35**, 2768 (2010).

[28] Q. Wang, S. Stobbe and P. Lodahl. *Mapping the Local Density of Optical States of a Photonic Crystal with Single Quantum Dots.* Physical Review Letters **107**, 167404 (2011).

[29] J. Johansen, B. Julsgaard, S. Stobbe, J. M. Hvam and P. Lodahl. *Probing long-lived dark excitons in self-assembled quantum dots.* Physical Review B **81**, 081304 (2010).

[30] L. Besombes, K. Kheng, L. Marsal and H. Mariette. *Acoustic phonon broadening mechanism in single quantum dot emission.* Physical Review B **63**, 155307 (2001).

[31] I. Favero, A. Berthelot, G. Cassabois, C. Voisin, C. Delalande *et al. Temperature dependence of the zero-phonon linewidth in quantum dots: An effect of the fluctuating environment.* Physical Review B **75**, 073308 (2007).

[32] B. Urbaszek, E. J. McGhee, M. Krüger, R. J. Warburton, K. Karrai *et al. Temperature-dependent linewidth of charged excitons in semiconductor quantum dots: Strongly broadened ground state transitions due to acoustic phonon scattering.* Physical Review B **69**, 035304 (2004).

[33] O. Gazzano, S. Michaelis de Vasconcellos, C. Arnold, A. Nowak, E. Galopin *et al. Bright solid-state sources of indistinguishable single photons.* Nature communications **4**, 1425 (2013).

[34] J. Liu. *Semiconductor Nanomembranes for Quantum Photonics: Quantum Light Sources and Optomechanics.* Ph.D. thesis, Technical University of Denmark (2012).

[35] M. Winger. *Mesoscopic Cavity QED with a Single Quantum Dot.* Ph.D. thesis, ETH Zurich (2009).

[36] M. Winger, T. Volz, G. Tarel, S. Portolan, A. Badolato *et al. Explanation of Photon Correlations in the Far-Off-Resonance Optical Emission from a Quantum-Dot–Cavity System.* Physical Review Letters **103**, 207403 (2009).

[37] M. L. Andersen, S. Stobbe, A. S. Sørensen and P. Lodahl. *Strongly modified plasmon–matter interaction with mesoscopic quantum emitters.* Nature Physics **7**, 215 (2010).

[38] R. Loudon. *The Quantum Theory of Light* (Oxford Science Publications, Oxford, 2000), third edition.

[39] E. Yablonovitch. *Inhibited Spontaneous Emission in Solid-State Physics and Electronics.* Physical Review Letters **58**, 2059 (1987).

[40] S. John. *Strong localization of photons in certain disordered dielectric superlattices.* Physical Review Letters **58**, 2486 (1987).

[41] J. D. Joannopoulos, S. G. Johnson, R. D. Meade and J. N. Winn. *Photonic Crystals: Molding the Flow of Light* (Princeton University Press, 2008), second edition.

[42] S. Stobbe. *Enhancement of Light-matter Interaction in Semiconductor Nanostructures.* Ph.D. thesis, Technical University of Denmark (2009).

[43] S.-i. Takayama, H. Kitagawa, Y. Tanaka, T. Asano and S. Noda. *Experimental demonstration of complete photonic band gap in two-dimensional photonic crystal slabs.* Applied Physics Letters **87**, 061107 (2005).

[44] Y. Akahane, T. Asano, B.-S. Song and S. Noda. *High-Q photonic nanocavity in a two-dimensional photonic crystal.* Nature **425**, 944 (2003).

[45] H.-Y. Ryu, M. Notomi and Y.-H. Lee. *High-quality-factor and small-mode-volume hexapole modes in photonic-crystal-slab nanocavities.* Applied Physics Letters **83**, 4294 (2003).

[46] Z. Zhang and M. Qiu. *Small-volume waveguide-section high Q microcavities in 2D photonic crystal slabs.* Optics Express **12**, 3988 (2004).

[47] Y. Akahane, T. Asano, B.-S. Song and S. Noda. *Fine-tuned high-Q photonic-crystal nanocavity.* Optics Express **13**, 1202 (2005).

[48] E. Jaynes and F. Cummings. *Comparison of quantum and semiclassical radiation theories with application to the beam maser.* Proceedings of the IEEE **51**, 89 (1963).

[49] M. O. Scully and M. S. Zubairy. *Quantum Optics* (Cambridge University Press, 1997), first edition.

[50] F. Marquardt and A. Püttmann. *Introduction to dissipation and decoherence in quantum systems.* arXiv:0809.4403 (2008).

[51] G. Lindblad. *On the generators of quantum dynamical semigroups.* Communications in Mathematical Physics (1965-1997) **48**, 119 (1976).

[52] H. Carmichael, R. Brecha, M. Raizen, H. Kimble and P. Rice. *Subnatural linewidth averaging for coupled atomic and cavity-mode oscillators.* Physical Review A **40**, 5516 (1989).

[53] A. Muller. *Resonance Flourescence and Cavity Quantum Electrodynamics with Quantum Dots.* Ph.D. thesis, The University of Texas at Austin (2007).

[54] E. M. Purcell. *Spontaneous emission probabilities at radio frequencies.* Physical Review **69** (1946).

[55] K. H. Madsen, P. Kaer, A. Kreiner-Møller, S. Stobbe, A. Nysteen *et al.* *Measuring the effective phonon density of states of a quantum dot in cavity quantum electrodynamics.* Physical Review B **88**, 045316 (2013).

[56] K. H. Madsen, S. Ates, T. Lund-Hansen, A. Löffler, S. Reitzenstein *et al.* *Observation of Non-Markovian Dynamics of a Single Quantum Dot in a Micropillar Cavity.* Physical Review Letters **106**, 233601 (2011).

[57] I. I. Rabi. *Space quantization in a gyrating magnetic field.* Physical Review **51**, 652 (1937).

[58] A. Laucht, N. Hauke, J. Villas-Bôas, F. Hofbauer, G. Böhm *et al.* *Dephasing of Exciton Polaritons in Photoexcited InGaAs Quantum Dots in GaAs Nanocavities.* Physical Review Letters **103**, 087405 (2009).

[59] N. Wiener. *Generalized harmonic analysis.* Acta Mathematica **55**, 117 (1930).

[60] G. Cui and M. Raymer. *Emission spectra and quantum efficiency of single-photon sources in the cavity-QED strong-coupling regime.* Physical Review A **73** (2006).

[61] J. Perea, D. Porras and C. Tejedor. *Dynamics of the excitations of a quantum dot in a microcavity.* Physical Review B **70**, 115304 (2004).

[62] S. Stobbe, J. Johansen, P. Kristensen, J. Hvam and P. Lodahl. *Frequency dependence of the radiative decay rate of excitons in self-assembled quantum dots: Experiment and theory.* Physical Review B **80**, 155307 (2009).

[63] P. T. Kristensen, C. Van Vlack and S. Hughes. *Generalized effective mode volume for leaky optical cavities* (2011).

[64] T. Lehmann. *Collective effects of Quantum Dots in Photonic Crystal Cavities.* Master thesis, Technical University of Denmark (2013).

[65] D. Fattal, E. Diamanti, K. Inoue and Y. Yamamoto. *Quantum Teleportation with a Quantum Dot Single Photon Source.* Physical Review Letters **92**, 037904 (2004).

[66] A. Reinhard, T. Volz, M. Winger, A. Badolato, K. J. Hennessy *et al.* *Strongly correlated photons on a chip.* Nature Photonics **6**, 93 (2011).

[67] H. Kim, R. Bose, T. C. Shen, G. S. Solomon and E. Waks. *A quantum logic gate between a solid-state quantum bit and a photon.* Nature Photonics **7**, 373 (2013).

[68] J. L. O'Brien, A. Furusawa and J. Vučković. *Photonic quantum technologies.* Nature Photonics **3**, 687 (2009).

[69] K. H. Madsen and P. Lodahl. *Quantitative analysis of quantum dot dynamics and emission spectra in cavity quantum electrodynamics.* New Journal of Physics **15** (2013).

[70] J. Gérard, B. Sermage, B. Gayral, B. Legrand, E. Costard *et al. Enhanced Spontaneous Emission by Quantum Boxes in a Monolithic Optical Microcavity.* Physical Review Letters **81**, 1110 (1998).

[71] E. Moreau, I. Robert, J. M. Gérard, I. Abram, L. Manin *et al. Single-mode solid-state single photon source based on isolated quantum dots in pillar microcavities.* Applied Physics Letters **79**, 2865 (2001).

[72] C. Santori, D. Fattal, J. Vučković, G. S. Solomon and Y. Yamamoto. *Indistinguishable photons from a single-photon device.* Nature **419**, 594 (2002).

[73] J. P. Reithmaier, G. Sek, A. Löffler, C. Hofmann, S. Kuhn *et al. Strong coupling in a single quantum dot-semiconductor microcavity system.* Nature **432**, 197 (2004).

[74] T. Yoshie, A. Scherer, J. Hendrickson, G. Khitrova, H. M. Gibbs *et al. Vacuum Rabi splitting with a single quantum dot in a photonic crystal nanocavity.* Nature **432**, 200 (2004).

[75] B. Mollow. *Power Spectrum of Light Scattered by Two-Level Systems.* Physical Review **188**, 1969 (1969).

[76] S. Ates, S. Ulrich, S. Reitzenstein, A. Löffler, A. Forchel *et al. Post-Selected Indistinguishable Photons from the Resonance Fluorescence of a Single Quantum Dot in a Microcavity.* Physical Review Letters **103**, 167402 (2009).

[77] A. Löffler, J. P. Reithmaier, G. Sek, C. Hofmann, S. Reitzenstein *et al. Semiconductor quantum dot microcavity pillars with high-quality factors and enlarged dot dimensions.* Applied Physics Letters **86**, 111105 (2005).

[78] A. B. Young, R. Oulton, C. Y. Hu, A. C. T. Thijssen, C. Schneider *et al. Quantum-dot-induced phase shift in a pillar microcavity.* Physical Review A **84**, 011803 (2011).

[79] M. Lermer, N. Gregersen, F. Dunzer, S. Reitzenstein, S. Höfling *et al. Bloch-Wave Engineering of Quantum Dot Micropillars for Cavity Quantum Electrodynamics Experiments.* Physical Review Letters **108**, 057402 (2012).

[80] T. Lund-Hansen. *Time-Resolved Spectroscopy of Quantum Dot Single-Photon Sources.* Ph.D. thesis, Technical University of Denmark (2009).

[81] A. N. Vamivakas, S. B. Ippolito, A. K. Swan, M. S. Ünlü, M. Dogan *et al. Phase-sensitive detection of dipole radiation in a fiber-based high numerical aperture optical system.* Optics Letters **32**, 970 (2007).

[82] M. Brune, F. Schmidt-Kaler, A. Maali, J. Dreyer, E. Hagley *et al. Quantum Rabi Oscillation: A Direct Test of Field Quantization in a Cavity.* Physical Review Letters **76**, 1800 (1996).

[83] B. Gayral and J. Gérard. *Photoluminescence experiment on quantum dots embedded in a large Purcell-factor microcavity.* Physical Review B **78**, 235306 (2008).

[84] J. Taylor. *Error Analysis: The study of uncertainties in physical measurements* (University Science Books, Sausalito, California, 1997), second edition.

[85] J. Johansen. *Decay Dynamics of Quantum Dots in Nanophotonic Structures.* Ph.D. thesis, Technical University of Denmark (2008).

[86] U. Hohenester, A. Laucht, M. Kaniber, N. Hauke, A. Neumann *et al. Phonon-assisted transitions from quantum dot excitons to cavity photons.* Physical Review B **80**, 201311(R) (2009).

[87] A. Auffèves, D. Gerace, J.-M. Gérard, M. F. Santos, L. C. Andreani *et al. Controlling the dynamics of a coupled atom-cavity system by pure dephasing.* Physical Review B **81**, 245419 (2010).

[88] C. K. Hong, Z. Y. Ou and L. Mandel. *Measurement of subpicosecond time intervals between two photons by interference.* Physical Review Letters **59**, 2044 (1987).

[89] P. Borri, W. Langbein, S. Schneider, U. Woggon, R. Sellin *et al. Ultralong Dephasing Time in InGaAs Quantum Dots.* Physical Review Letters **87**, 157401 (2001).

[90] E. Peter, P. Senellart, D. Martrou, A. Lemaître, J. Hours *et al. Exciton-Photon Strong-Coupling Regime for a Single Quantum Dot Embedded in a Microcavity.* Physical Review Letters **95**, 067401 (2005).

[91] Y. Ota, M. Shirane, M. Nomura, N. Kumagai, S. Ishida *et al. Vacuum Rabi splitting with a single quantum dot embedded in a H1 photonic crystal nanocavity.* Applied Physics Letters **94**, 033102 (2009).

[92] D. Englund, A. Majumdar, A. Faraon, M. Toishi, N. Stoltz *et al. Resonant Excitation of a Quantum Dot Strongly Coupled to a Photonic Crystal Nanocavity.* Physical Review Letters **104**, 073904 (2010).

[93] K. Hennessy, A. Badolato, M. Winger, D. Gerace, M. Atatüre *et al. Quantum nature of a strongly coupled single quantum dot-cavity system.* Nature **445**, 896 (2007).

[94] S. Mosor, J. Hendrickson, B. C. Richards, J. Sweet, G. Khitrova *et al. Scanning a photonic crystal slab nanocavity by condensation of xenon.* Applied Physics Letters **87**, 141105 (2005).

[95] A. Kreiner-Møller. *Quantum Dots in Photonic Crystal Nanocavities.* Master thesis, Technical University of Denmark (2011).

[96] S. Lea. *Mathematics for Physicists* (Thomson Brooks/Cole, 2004), first edition.

[97] K. H. Madsen. *Dynamics of Quantum Dots in Micropillar Cavities.* Master thesis, Technical University of Denmark (2010).

[98] S. Ates, S. M. Ulrich, A. Ulhaq, S. Reitzenstein, A. Löffler *et al. Non-resonant dot–cavity coupling and its potential for resonant single-quantum-dot spectroscopy.* Nature Photonics **3**, 724 (2009).

[99] M. Kaniber, A. Laucht, A. Neumann, J. Villas-Bôas, M. Bichler *et al. Investigation of the nonresonant dot-cavity coupling in two-dimensional photonic crystal nanocavities.* Physical Review B **77**, 161303 (2008).

[100] I. Diniz, S. Portolan, R. Ferreira, J. M. Gérard, P. Bertet *et al. Strongly coupling a cavity to inhomogeneous ensembles of emitters: Potential for long-lived solid-state quantum memories.* Physical Review A **84**, 063810 (2011).

[101] S. Stobbe, T. W. Schlereth, S. Höfling, A. Forchel, J. M. Hvam *et al. Large quantum dots with small oscillator strength.* Physical Review B **82**, 233302 (2010).

[102] M. Eichenfield, J. Chan, R. M. Camacho, K. J. Vahala and O. Painter. *Optomechanical crystals.* Nature **462**, 78 (2009).

[103] L. Ding, C. Baker, P. Senellart, A. Lemaitre, S. Ducci *et al. High Frequency GaAs Nano-Optomechanical Disk Resonator.* Physical Review Letters **105**, 263903 (2010).

[104] E. Gavartin, R. Braive, I. Sagnes, O. Arcizet, A. Beveratos *et al. Optomechanical Coupling in a Two-Dimensional Photonic Crystal Defect Cavity.* Physical Review Letters **106**, 203902 (2011).

[105] D. A. Fuhrmann, S. M. Thon, H. Kim, D. Bouwmeester, P. M. Petroff *et al. Dynamic modulation of photonic crystal nanocavities using gigahertz acoustic phonons.* Nature Photonics **5**, 605 (2011).

[106] I. Wilson-Rae, P. Zoller and A. Imamoğlu. *Laser Cooling of a Nanomechanical Resonator Mode to its Quantum Ground State.* Physical Review Letters **92**, 075507 (2004).

[107] K. Usami, A. Naesby, T. Bagci, B. Melholt Nielsen, J. Liu *et al. Optical cavity cooling of mechanical modes of a semiconductor nanomembrane.* Nature Physics **8**, 168 (2012).

[108] P. Kaer, T. R. Nielsen, P. Lodahl, A.-P. Jauho and J. Mørk. *Microscopic theory of phonon-induced effects on semiconductor quantum dot decay dynamics in cavity QED.* Physical Review B **86**, 085302 (2012).

[109] F. Rol, S. Founta, H. Mariette, B. Daudin, L. Dang *et al. Probing exciton localization in nonpolar GaN/AlN quantum dots by single-dot optical spectroscopy.* Physical Review B **75**, 125306 (2007).

[110] G. Ortner, D. Yakovlev, M. Bayer, S. Rudin, T. Reinecke *et al. Temperature dependence of the zero-phonon linewidth in InAs/GaAs quantum dots.* Physical Review B **70**, 201301(R) (2004).

[111] M. Calic, P. Gallo, M. Felici, K. A. Atlasov, B. Dwir *et al. Phonon-Mediated Coupling of InGaAs/GaAs Quantum-Dot Excitons to Photonic Crystal Cavities.* Physical Review Letters **106**, 227402 (2011).

[112] B. Krummheuer, V. Axt and T. Kuhn. *Theory of pure dephasing and the resulting absorption line shape in semiconductor quantum dots.* Physical Review B **65**, 195313 (2002).

[113] P. Kaer, T. R. Nielsen, P. Lodahl, A.-P. Jauho and J. Mørk. *Non-Markovian Model of Photon-Assisted Dephasing by Electron-Phonon Interactions in a Coupled Quantum-Dot–Cavity System.* Physical Review Letters **104**, 157401 (2010).

[114] A. J. Ramsay, T. M. Godden, S. J. Boyle, E. M. Gauger, A. Nazir *et al. Phonon-Induced Rabi-Frequency Renormalization of Optically Driven Single InGaAs/GaAs Quantum Dots.* Physical Review Letters **105**, 177402 (2010).

[115] S. Laurent, S. Varoutsis, L. Le Gratiet, A. Lemaître, I. Sagnes *et al. Indistinguishable single photons from a single-quantum dot in a two-dimensional photonic crystal cavity.* Applied Physics Letters **87**, 163107 (2005).

[116] L. Sapienza, H. Thyrrestrup, S. Stobbe, P. D. Garcia, S. Smolka *et al. Cavity quantum electrodynamics with Anderson-localized modes.* Science (New York, N.Y.) **327**, 1352 (2010).

[117] K. G. Lee, X. W. Chen, H. Eghlidi, P. Kukura, R. Lettow *et al. A planar dielectric antenna for directional single-photon emission and near-unity collection efficiency.* Nature Photonics **5**, 166 (2011).

[118] J. Claudon, J. Bleuse, N. S. Malik, M. Bazin, P. Jaffrennou *et al. A highly efficient single-photon source based on a quantum dot in a photonic nanowire.* Nature Photonics **4**, 174 (2010).

[119] Y.-M. He, Y. He, Y.-J. Wei, D. Wu, M. Atatüre *et al. On-demand semiconductor single-photon source with near-unity indistinguishability.* Nature nanotechnology **8**, 213 (2013).

[120] A. Kiraz, S. Fälth, C. Becher, B. Gayral, W. Schoenfeld *et al. Photon correlation spectroscopy of a single quantum dot.* Physical Review B **65**, 161303 (2002).

[121] M. E. Reimer, G. Bulgarini, N. Akopian, M. Hocevar, M. B. Bavinck *et al. Bright single-photon sources in bottom-up tailored nanowires.* Nature communications **3**, 737 (2012).

[122] J. Vucković, M. Loncar, H. Mabuchi and A. Scherer. *Optimization of the Q factor in photonic crystal microcavities.* IEEE Journal of Quantum Electronics **38**, 850 (2002).

[123] S.-H. Kim, S.-K. Kim and Y.-H. Lee. *Vertical beaming of wavelength-scale photonic crystal resonators.* Physical Review B **73**, 235117 (2006).

[124] M. Brewster, O. Schimek, S. Reich and S. Gradečak. *Exciton-phonon coupling in individual GaAs nanowires studied using resonant Raman spectroscopy.* Physical Review B **80**, 201314 (2009).

[125] S. Hameau, Y. Guldner, O. Verzelen, R. Ferreira, G. Bastard *et al. Strong Electron-Phonon Coupling Regime in Quantum Dots: Evidence for Everlasting Resonant Polarons.* Physical Review Letters **83**, 4152 (1999).

[126] P. Y. Yu and M. Cardona. *Fundamentals of Semiconductors* (Springer-Verlag Berlin Heidelberg, 2010), fourth edition.

[127] S. Weiler, A. Ulhaq, S. M. Ulrich, D. Richter, M. Jetter *et al. Phonon-assisted incoherent excitation of a quantum dot and its emission properties.* Physical Review B **86**, 241304 (2012).

[128] A. Kiraz, M. Atatüre and A. Imamoğlu. *Quantum-dot single-photon sources: Prospects for applications in linear optics quantum-information processing.* Physical Review A **69**, 032305 (2004).

[129] J. Bylander and I. Abram. *Interference and correlation of two independent photons.* The European Physical Journal D **22**, 295 (2003).

[130] P. Kaer, P. Lodahl, A.-P. Jauho and J. Mørk. *Microscopic theory of indistinguishable single-photon emission from a quantum dot coupled to a cavity: The role of non-Markovian phonon-induced decoherence.* Physical Review B **87**, 081308 (2013).

[131] J. Blakemore. *Semiconducting and other major properties of gallium arsenide.* Journal of Applied Physics **53**, 123 (1982).

[132] A. Muller, E. B. Flagg, P. Bianucci, X. Y. Wang, D. G. Deppe *et al. Resonance Fluorescence from a Coherently Driven Semiconductor Quantum Dot in a Cavity.* Physical Review Letters **99** (2007).

[133] E. B. Flagg, A. Muller, J. W. Robertson, S. Founta, D. G. Deppe *et al. Resonantly driven coherent oscillations in a solid-state quantum emitter.* Nature Physics **5**, 203 (2009).

[134] A. N. Vamivakas, Y. Zhao, C.-Y. Lu and M. Atatüre. *Spin-resolved quantum-dot resonance fluorescence.* Nature Physics **5**, 198 (2009).

[135] C. Matthiesen, A. N. Vamivakas and M. Atatüre. *Subnatural Linewidth Single Photons from a Quantum Dot.* Physical Review Letters **108**, 093602 (2012).

[136] H. S. Nguyen, G. Sallen, C. Voisin, P. Roussignol, C. Diederichs *et al. Ultra-coherent single photon source.* Applied Physics Letters **99**, 261904 (2011).

[137] C. Matthiesen, M. Geller, C. H. H. Schulte, C. Le Gall, J. Hansom *et al. Phase-locked indistinguishable photons with synthesized waveforms from a solid-state source.* Nature Communications **4**, 1600 (2013).

[138] R. Melet, V. Voliotis, A. Enderlin, D. Roditchev, X. Wang *et al. Resonant excitonic emission of a single quantum dot in the Rabi regime.* Physical Review B **78**, 073301 (2008).

[139] A. J. Ramsay, A. V. Gopal, E. M. Gauger, A. Nazir, B. W. Lovett *et al.* *Damping of Exciton Rabi Rotations by Acoustic Phonons in Optically Excited InGaAs/GaAs Quantum Dots.* Physical Review Letters **104**, 017402 (2010).

[140] E. D. Kim, A. Majumdar, H. Kim, P. Petroff and J. Vuckovic. *Differential reflection spectroscopy of a single quantum dot strongly coupled to a photonic crystal cavity.* Applied Physics Letters **97**, 053111 (2010).